CHARACTERIZATIONS OF SPATIO-TEMPORAL COMPLEX SYSTEMS

A Thesis
Presented to
The Academic Faculty

by

Kapilanjan Krishan

In Partial Fulfillment
of the Requirements for the Degree
Doctor of Philosophy

School of Physics
Georgia Institute of Technology
August 2005

CHARACTERIZATIONS OF SPATIO-TEMPORAL COMPLEX SYSTEMS

Approved by:

Dr. Michael F. Schatz, Advisor
School of Physics
Georgia Institute of Technology

Dr. Konstantin Mischaikow
School of Mathematics
Georgia Institute of Technology

Dr. Roman O. Grigoriev
School of Physics
Georgia Institute of Technology

Dr. Predrag Cvitanović
School of Physics
Georgia Institute of Technology

Dr. Turgay Uzer
School of Physics
Georgia Institute of Technology

Date Approved: 12th April 2005

ACKNOWLEDGEMENTS

A number of people have guided and participated in the efforts that has resulted in this thesis.

As an advisor, Mike has been an inexhaustible source of optimism, no matter how far the experiments might seem from the desired results. Much of the experimental development on laser actuation would not have progressed as long without his direction. Mike has been very patient in developing effective communication amongst his students. I have always found him supportive of presenting our work at various meetings, and have much to learn from his "word-smithing" of manuscripts. I have cherished the enormous(and enviable!) independence in the day to day work in lab, with responses to my financial requests for just about anything being immediate and consistent – "Have at it!".

The theoretical framework for our experiments on studying defects relevant to Spiral Defect Chaos would not have been possible without Roman. His office next door has been my refuge, for many hours, when I needed guidance with numerics. Andreas wrote the initial version of the code to perform data analysis. I have also benefited from many discussions I have had with Manu, at SUNY Stony Brook, about my projects and in particular with the error analysis for the nonlinear optimization.

It has been delightful to collaborate with Konstantin and Marcio at the School of Mathematics. The different perspective on pattern formation they offered us was refreshing, and timely! Under Konstantin's guidance, the homological characterization of patterns in our experiments has proven its use as a robust and useful tool to study dynamical systems. Marcio played a pivotal role in quickly instructing me in the mathematical formalism, maneuvering through essential parts of the code and its use, and also performed the homology computations on many experimental runs.

Much of what I have learnt on Periodic Orbit Theory has been from excellent courses taught by Predrag. Courses at the School of Physics by Uzi Landman have been very

TABLE OF CONTENTS

LIST OF FIGURES

SUMMARY

Two tools to characterize spatiotemporal complex systems are developed in this thesis, and used in experiments on Rayleigh-Benard convection(RBC) to probe the dynamical evolution of spiral defect chaos(SDC). Prior investigations suggest that the turbulence in SDC is defect mediated, with defect formation resulting in variations in the global topology of the pattern of fluid flow. We investigate the dynamics at local scales corresponding to the neighborhood of defect nucleation as well as at scales of the system size where global topological rearrangements are most noticeable.

At the local scale, we develop experimental as well as numerical tools to extract the linear manifold for local instabilities associated with defect nucleations. Our experimental setup enables us to impose desired initial states for the flow in RBC and prepare a selected ensemble of initial conditions in the neighborhood of defect nucleation. The initial conditions are chosen utilizing the symmetries of the flow, so as to maximally span the linear manifold about the defect nucleation event. The short time evolution of the ensemble is used to construct a basis for this manifold using proper orthogonal decomposition. The modes and growth rates are extracted by nonlinear optimization after projecting the evolution onto this basis to reduce the embedding space. The information so obtained should be useful in the implementation of schemes to control spatiotemporally complex dynamics.

At the global scale, defect nucleations mark regions where the topology of the pattern changes. We track the global topological evolution of the pattern through its homology - one of the easiest to measure topological invariants. The homology characterizes the geometry of the flow by a set of non-negative integers known as the Betti numbers. In addition to providing information about the global evolution through such reduced measures, a time series of the Betti numbers gives us many novel insights into the flow not otherwise revealed: (1) The Betti numbers time series provide a measure of the complexity of the flow, which may be used to estimate the parameters controlling the dynamics, (2) Quantities derived

from the Betti number time series at different parameter values can indicate transitions into the turbulent regime (3) The asymmetry between hot flows and cold flows that we measure suggests non-Boussinesq effects, (4) The entropy of the state at different parameter values can indicate bifurcations occurring even in the turbulent regime, (5) The global pattern evolves towards being primarily stochastic and (6) A new measure of boundary influence is introduced, relating connectivity to the boundary rather than the distance from it.

CHAPTER I

INTRODUCTION

1.1   Motivation

The approach to thermodynamic equilibrium is associated with the decay of gradients through dissipative processes that redistribute the energy in a system. This flux of energy across gradients ensures that equilibrium patterns are mostly uniform - devoid of any structure except for stochastic fluctuations. When there is an external flux of energy, gradients may be sustained as the dissipative losses are supplemented by the driving through the external source. Nonequilibrium systems typically exhibit patterns as a result of such interaction between driving and dissipative mechanisms [40, 58, 16]. Such patterns range in their dynamical behavior from being regular and stationary to highly complex and time dependent. Understanding such complex states is amongst the most important challenges faced by current science.

One of the primary difficulties in dealing with nonequilibrium spatial patterns is developing efficient characterizations that capture the essential dynamics that exhibits the complex behavior of the system. Such characterizations are motivated by the dynamical features one requires to capture for the particular system under study. In this thesis we detail quantitative techniques that are generically applicable to the study of spatially extended complex systems and are especially suited to experimental characterizations, and also in situations when the system has no good mathematical model and is not amenable to numerical and analytical investigations. Typically theoretical methods require the pursuit of trajectories in large dimensional phase spaces while experiments are limited to capturing only a fraction of the complete dynamics.

The transition to complex behavior is usually preceded by time-independent (or stationary states/fixed points) and time-periodic (also referred to as periodic orbits) states of the system. The progression from stationary states to time periodic to complex states can

often be tracked by a variation of some experimental parameter driving the system through a sequence of instabilities [40, 16, 39]. The first instability that results in the emergence of a pattern in a system originally in a uniform steady state is referred to as the primary instability of the system. The parameter is typically associated with the external flux of energy of the system relative to the dissipative mechanisms. Such an instability is characterized by intrinsic length and/or time scales that determine the structure of the pattern. The onset of this pattern is typically regular, being determined by only one spatial and/or temporal scale [16]. Further variation in the system parameter can result in secondary instabilities and the occurrence of irregular spatio-temporal states with the earlier regular states now turning unstable. The transition to complex dynamics can be viewed as a result of the interactions between previously stable states. Such mechanisms was first proposed by Landau as superpositions of infinite numbers of unstable states for the onset of turbulence [39]. The fundamental advance in the field was by Ruelle and Takens, discovering that nonlinear interactions between a few unstable modes generically results in turbulence [53].

Instabilities lead to the breaking of underlying symmetries of the system [16]. The system chooses one of the multiple solutions allowed by the dynamical equations in the regime in which the instability occurs. Such selection may be determined either by small stochastic fluctuations or through biases induced through the boundary conditions. The instability thus characterizes the transition from an unstable base state to a different stable state as the parameters of the system are varied. A base state is said to be linearly unstable if unstable against infinitesimal perturbations. The evolution of an infinitesimal volume in the phase space of the system undergoing a linear instability is characterized by the linear manifold within which the instability develops and the rate of change of volume in this manifold is measured by a set of numbers referred to as Lyapunov exponents. The characterization of a system by a linear evolution is most accurate about base states that represent stationary states or time-periodic trajectories [58, 18].

In spite of the severe restriction posed on the validity of the linear manifold, it is still invaluable to the characterization of a large class of complex systems. The trajectory of these systems is confined to the neighborhood of the unstable time-periodic and stationary

solutions and as the instabilities accumulate, the hyperbolic manifold of these solutions drive the system towards chaotic behavior. The chaotic attractor is defined as the closure of the set of unstable periodic orbits and fixed points. It can be shown that the long time averages of observables in hyperbolic chaotic systems(systems with isolated unstable periodic orbits and fixed points) can be determined from averages over the unstable periodic orbits comprising the attractor[18]. This is because the trajectory of the system in such an attractor evolves exponentially close to periodic orbits along their stable manifolds and the chaos is generated as the hyperbolic manifold scatters the trajectory amongst periodic orbits. In an interesting note, the longer periodic orbits can be approximated to be comprised of shorter orbits making the evaluation over the shorter orbits sufficient to generate long time averages of observables to remarkable accuracy.

The periodic orbits and fixed points form invariant structures within the chaotic attractor. The development of techniques to determine the stable and unstable manifolds of these structures that forms the skeleton of the chaotic strange attractor is of prime importance to its characterization.

The trajectory in the chaotic strange attractor often displays approximately recurrent behavior due to the underlying periodic structure of the attractor. This signatures of the unstable periodic orbits have been utilized in numerical work to extract periodic orbits of a system [1]. In spatially extended systems it would not be unexpected to find smaller period orbits to be extended over a smaller spatial domain than longer period orbits. It is less probable for structures to maintain their coherence over large spatial extents in turbulent systems. It is yet unknown if longer and spatially extended orbits may be approximated by a composition of spatially local shorter period orbits and fixed points. Recurrences in the local dynamics are easier to identify. Translation and rotation of these local dynamics might capture a significant section of the spatially extended dynamics in a chaotic system.

The unstable manifolds of the periodic orbits drive the chaos in a chaotic attractor and hold the key to controlling chaos. When these manifolds are spatially localized, it makes the local dynamics especially relevant, for one could attempt at devising schemes of control that require only local control to steer the global dynamics. In addition to the smaller

energetic inputs expected for local control making such schemes easier to implement, one only needs to characterize the local dynamics, reducing the computational effort required.
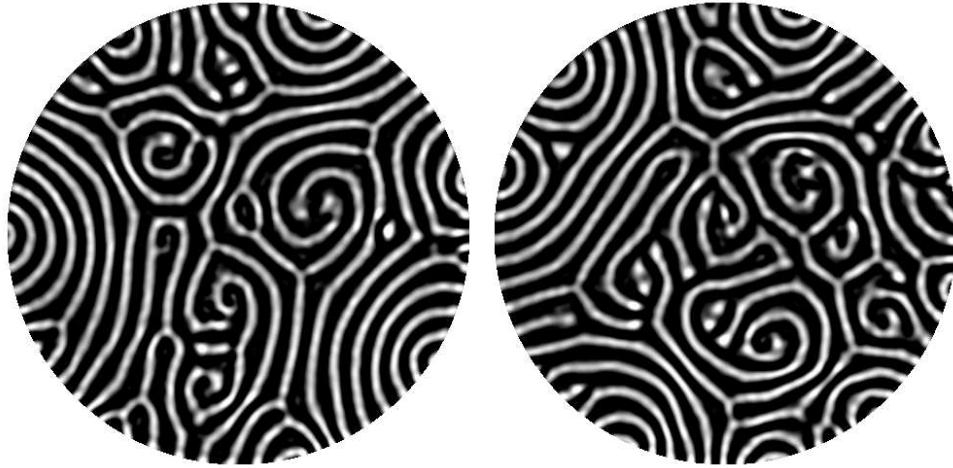
Figure 1: The states above are shadowgraph images of weakly turbulent convective flow in Rayleigh-Bénard convection known as spiral defect chaos. The two images represent configurations at different times taken by the system while all external parameters controlling the flow are held constant. While qualitatively similar, details of the structure are quite different. The complex evolution is manifest in the dynamic variation in the geometry of the state shown here. Building robust and effective characterizations to capture such dynamics is one of the challenges in describing complex systems.

While the technical description of chaotic attractors requires an understanding of the unstable manifolds, most experimental discoveries of chaotic systems are categorized as being chaotic with no evaluation of quantities such as the Lyapunov exponents. A complex system can often be broken down into individual distinct components whose interaction manifest as complex geometric structures. For instance, in fluid flows one could distinguish components as represented with regions of positive or negative fluid velocities. The complex geometry while being qualitatively similar through the evolution of the system, differs in the details of the particular configurations spanned by the evolution as in Figure 1. Such gross variations in the geometry may be quantified by topological measures. While topological measures are by definition insensitive to the scales of structures, they nevertheless offer insight into properties such as connectedness, properties not easily accessed through other means. The distinctive feature of the topological characterization of patterns is that it

4

captures a portion of the global dynamical evolution of the pattern. It is such qualitatively complex and striking features that motivate the description of complex dynamical structures as being chaotic or turbulent.

The coarse and qualitative categorization of chaos is formally encompassed by a description of a system through its symbolic dynamics [18]. In this formalism, one associates an alphabet (or symbol) with the occurrence of a particular event in the dynamical system. The events may be arbitrary and the alphabet used is not unique - however, a good choice of such events yields a sequence of symbols that could be used in building a qualitative representation of the chaos. Of particular interest in building such symbol sequences are events that show recurrences. Symbolic dynamics enables one to build a low dimensional representation of the dynamical system capturing the essence of the complex behavior. Building a good symbolic dynamics is an arduous task for spatially extended systems but is fruitful in extracting further dynamically relevant quantities such as periodic orbits.

It would be interesting to make connections between the symbolic dynamics extracted from recurrences in global measures with those extracted from recurrent local dynamics. Hidden in global topological measures could lie a symbolic dynamics that tracks the evolution of the system as a whole while a local symbolic sequence would describe local variations that affect the global topology of a pattern. The duality between local and global properties of complex structures lies at the heart of understanding of such systems.

1.2 Outline

In the preceding section we have described the perspective from which we have been guided in our research. Characterizations of spatially extended complex dynamics revolve about an effective reduction of information from a high dimensional data set. We develop our characterizations for a weakly turbulent state of Rayleigh-Bénard convection known as Spiral Defect Chaos(SDC). This state shows complex evolving patterns comprising primarily of roll like structures punctuated by defects. The spirit of the characterization tools however are not restricted to this state and may be adapted to other systems with a few modifications.

In the next chapter we motivate the study of fluids in understanding complex systems

and describe some of the basic equations governing fluid flows. This also serves to define many of the quantities referred to through the remainder of the thesis. We end Chapter 2 by compiling the relevant results published for the state of SDC. This also lays the background over which our investigations are based. Chapter 3 describes in detail the experimental setup we use in our investigations. The chaos in SDC is suggested to be driven by recurrent defect nucleations. These nucleation events can be thought of as being instabilities associated with fixed points or periodic orbits of the system. The extraction and characterization of the linear manifold in experiments for such events is discussed in Chapter 4. The formation of defects results in the change in the linkage between the roll structures that form the essential features of the pattern. We track the changes in the topology resulting from the occurrence of defects in the structure by computing the homology of the pattern. The insights offered by such a topological characterization are described in Chapters 5 and 6. In the final chapter we summarize our outlook and discuss their implications for the state of SDC.

CHAPTER II

SPIRAL DEFECT CHAOS

2.1 The case for fluids

Classical fluids are amongst the most investigated pattern forming systems in experimental and theoretical studies. The basic driving and dissipation mechanisms are well identified and understood. There are various methods of driving such systems which have been modeled to remarkable agreement with experiments [10, 3]. While the dissipation mechanisms(often diffusive) are usually limited in the amount of energy flux they may sustain across gradients, it is possible to drive the relative external energy flux through the system in an unbounded manner. At sufficiently high driving, this leads to incommensurate "stresses" that manifest itself as complex dynamics, no matter what the mechanism of driving. The rich spectrum of dynamical behavior spanned by such systems make them instructive in the study of complex systems and turbulence. In this section, we develop the Navier-Stokes equations that have laid the foundations for studying classical fluids[10, 39]. We follow this by coupling these equations to driving induced through vertical temperature gradients. Such driving causes unstable stratification of density in a vertical gravitational field resulting in a convective instability. This mechanism was developed by Lord Rayleigh to explain experiments by Bénard and is known as Rayleigh-Bénard convection [51]. In the final section of this chapter, we describe an intriguing chaotic state of Rayleigh-Bénard convection called spiral defect chaos which will be the focus of investigation for the remainder of the thesis.

The distinguishing factor of a system modeled as a fluid is that a fluid is considered a continuous medium. Such an approximation stands good even when the underlying medium may be discrete, but the model describes physics at a coarse enough length scale at which the underlying discrete nature is not apparent. For kinematic considerations each point in a fluid is characterized by a mass density (ρ) and the velocity ($\mathbf{v}$) of the fluid. The *mass flux density* at the point is defined as $\rho\mathbf{v}$ and measures the mass of fluid flowing in the

direction of the local velocity. This flux over any closed surface should relate to change in mass enclosed within the surface per unit time (t). This relation is known as the *continuity equation* and is written below in its differential form.

$$\frac{\partial \rho}{\partial t} = -\nabla \cdot (\rho \mathbf{v})$$

The force on a volume of a fluid is transmitted across the surface enclosing the volume and equals the surface integral of the pressure (p) over the entire volume. This force serves to accelerate the mass of fluid held within the volume. We include a term, $F_{external}$, to accommodate forces not associated with the pressure at the surface such as gravity or electromagnetic fields.

$$\int \rho \frac{d\mathbf{v}}{dt} dV = -\int pd\mathbf{S} + F_{external} = -\int \nabla p dV + F_{external}$$

In this equation, we have made use of Green's formula to transform the surface integral into a volume integral. Since this relation holds true for any arbitrary volume, the equality also holds for just the integrands, yielding the equations of motion.

$$\rho \frac{d\mathbf{v}}{dt} = -\nabla p + F_{external}$$

In many physical situations, it is more relevant to calculate the fluid velocities at fixed spatial locations. We transform from a coordinate system moving with a fluid element to one stationary in a laboratory frame through the relation,

$$\mathbf{v} = \mathbf{v}(\mathbf{x}, t) \implies d\mathbf{v} = \frac{\partial \mathbf{v}}{\partial t} dt + (\mathbf{x} \cdot \nabla) \mathbf{v}$$

which leads to the *Euler's equations* below, describing an ideal fluid with no dissipation mechanisms. This is essentially a statement of the response to forces through the continuum of the fluid media.

$$\frac{\partial \mathbf{v}}{\partial t} + (\mathbf{v} \cdot \nabla) \mathbf{v} = \frac{1}{\rho} \Big[-\nabla p + F_{external} \Big] \tag{1}$$

This equation has to be solved in conjunction with boundary conditions on the velocity field. Typically, this condition requires that the velocity of the fluid equal the velocity of the boundary constraining the fluid.

The absence of any thermal transport mechanisms in a fluid described by the Euler equations means that the motion of any volume in the fluid undergoes adiabatic transport by the velocity field. In a laboratory frame, this may be stated as

$$\frac{\partial s}{\partial t} + (\mathbf{v} \cdot \nabla)s = 0 \tag{2}$$

The complete description of the state of a fluid as presented above is described by its density, velocity and pressure. The equation of continuity, the Euler equations and the equation for adiabatic transport completely solve for the state of a fluid system with no dissipation.

The mechanism of dissipation of energy in a fluid may be seen as one which acts to reduce the momentum of flow. In order to incorporate such mechanisms into the Euler equations, we first develop an expression for the *momentum flux density*. The momentum flux is related to the rate of change of the momentum of a unit volume of fluid.

$$\frac{\partial}{\partial t}\rho\mathbf{v} = \rho\frac{\partial \mathbf{v}}{\partial t} + \frac{\partial \rho}{\partial t}\mathbf{v}$$

We substitute from the equation of continuity (for $\frac{\partial \rho}{\partial t}$) and Euler's equation (in $\frac{\partial \mathbf{v}}{\partial t}$) to have

$$
\begin{aligned}
\frac{\partial}{\partial t}(\rho v_i) &= -\frac{\partial p}{\partial x_i} - \frac{\partial}{\partial x_k}(\rho v_i v_k) \\
&= \frac{\partial}{\partial x_k}(\rho p \delta_{ik} + \rho v_i v_k) \\
&= \frac{\partial \Pi_{ik}}{\partial x_k} \tag{3}
\end{aligned}
$$

where the quantity $\Pi_{ik} \equiv \rho p \delta_{ik} + \rho v_i v_k$ represents the ith component of the momentum flowing in unit time through a unit area perpendicular to the x_k axis and is known as the *momentum flux density tensor*. As presented above the momentum flux represents

the transfer of momentum associated with mechanical transport of fluid elements and the pressure distribution. The above form of the Euler equations are a convenient place to include influences due to dissipation mechanisms. This is done by adding a term$(-\sigma'_{ik})$ to the momentum flux density tensor that acts against the momentum transfer for the ideal fluid. Such a mechanism models *viscous* damping within the fluid and leads to irreversible transfers of energy. The contribution from such a term vanishes when the fluid velocity is a constant everywhere. $-\sigma'_{ik}$, the *viscous stress tensor*, acts to reduce gradients in velocity. For small gradients one may assume the momentum transfer being dominated by the first derivatives of the fluid velocity. In addition, the rotation of the coordinate system at a constant angular velocity Ω must also not contribute. The most general tensor satisfying the above constraints is of the form

$$\sigma'_{ik} = \eta\Big[\frac{\partial v_i}{\partial x_k} + \frac{\partial v_k}{\partial x_i} - \frac{2}{3}\delta_{ik}\frac{\partial v_l}{\partial x_l}\Big] + \zeta\delta_{ik}\frac{\partial v_l}{\partial x_l}$$

For an isotropic fluid, η and ζ are scalars, known as coefficients of viscosity. The dissipation of energy through viscous effects must be positive definite (energy is not injected into the system through dissipative mechanisms), therefore these coefficients are both positive.

We incorporate this term into Euler's equation by adding $\frac{\partial \sigma'_{ik}}{\partial x_k}$ to the right side of equation 3. This yields the most general form of the equations of motion of a viscous fluid.

$$\rho\Big(\frac{\partial v_i}{\partial t} + v_k\frac{\partial v_i}{\partial x_k}\Big) = -\frac{\partial p}{\partial x_i} + \frac{\partial \sigma'_{ik}}{\partial x_k}$$

For many practical applications involving fluid equations the coefficients of viscosity may be considered a constant. This reduces the above equation to the *Navier-Stokes equation*.

$$\rho\Big[\frac{\partial \mathbf{v}}{\partial t} + (\mathbf{v}\cdot\nabla)\mathbf{v}\Big] = -\nabla p + \eta\nabla^2\mathbf{v} + (\zeta + \frac{1}{3}\eta)\nabla(\nabla\cdot\mathbf{v})$$

A further approximation that the fluid is incompressible ($\nabla.\mathbf{v} = 0$)is usually made to simplify the Navier-Stokes equation. This assumption suffices in modeling many fluid systems. This reduces the equation of motion to

$$\frac{\partial \mathbf{v}}{\partial t} + (\mathbf{v} \cdot \nabla)\mathbf{v} = -\frac{1}{\rho}\nabla p + \nu \nabla^2 \mathbf{v}$$

where $\nu = \eta/\rho$. In the above equation, the first term on the left represents the local acceleration of the fluid, while the second term models the convective acceleration. The gradient of the pressure contributes the hydrostatic forces on a fluid element while the last term is the viscous force per unit mass acting upon the fluid. The origin of the last term lies in dissipative forces associated with shear between fluid layers.

From the dynamical systems perspective, the above equation has three primary features that are associated with the generation of complex solutions. Foremost amongst them is the quadratic nonlinearity in the velocity seen in the convective term. The dissipation mechanism through the viscous term causes an irreversible transfer of energy. The pressure field at a point depends on the state of the fluid throughout the bulk. This induces non-local interactions.

In the absence of any energy flux into the system, the dissipative forces redistribute the velocity profile to yield a stationary solution with zero velocity. Typically, one couples the Navier-Stokes equations with terms associated with external energy flux that drives the fluid flow in conjunction with the dissipation. One of the first such mechanisms studied was driving induced through temperature gradients.

2.2   Rayleigh-Benard Convection

The primary ingredients for fluid flow in Rayleigh-Benard convection are a gravitational field along with buoyancy caused by density variations. These density variations result from externally imposed temperature gradients. The dissipation mechanisms of thermal conductivity and viscous drag are usually sufficient to model Rayleigh-Benard systems to remarkable agreement with experiments [10, 16].

The Navier-Stokes equations describing the fluid velocities are coupled with the thermal and viscous dissipation mechanisms. An additional approximation that is made to simplify the governing equations is that fluid properties such as the thermal conductivity, viscosity etc. do not vary to first order with the temperature gradients. Only the density is allowed to

11

vary along the vertical thermal gradient making buoyancy the primary driving mechanism.

$$\rho = \rho_0[1 - \alpha(T - T_{ref})]$$

where T_{ref} is some reference temperature, usually the mean temperature of the fluid and α is the thermal expansivity of the gas. The equations describing the fluid flow in Rayleigh Benard convection are

$$
\begin{aligned}
(\partial_t + \mathbf{v} \cdot \nabla)\mathbf{v} &= -\nabla\left(\frac{p}{\rho}\right) + \nu\nabla^2\mathbf{v} + g\alpha(T - T_{ref})\hat{z} \\
(\partial_t + \mathbf{v} \cdot \nabla)T &= \kappa\nabla^2 T \\
\nabla \cdot \mathbf{v} &= 0
\end{aligned}
$$
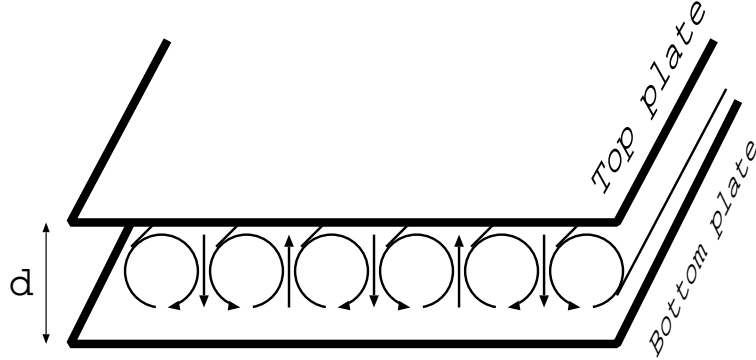
Figure 2: The essential description of Rayleigh-Benard convection - a fluid bounded between two infinite horizontal plates maintained at different temperatures, keeping a uniform separation d between them. The roll like structures between the plates indicates the fluid velocity after the onset of convection.

The study of a Rayleigh-Bénard system is usually confined to a simple geometry of vertically confining the fluid between two flat, rigid and parallel surfaces that have a spatially uniform temperature maintained at all times as in Figure 2. Thermal gradients are imposed across the fluid by variation of the temperature difference between these surfaces. While the essential features of this system may be studied considering an infinite spatial extent in the horizontal direction, experiments are limited to having a finite aspect ratio(the ratio of the horizontal to vertical dimensions of the confining geometry). The boundary influences are significant in systems with low aspect ratios.

Above a critical temperature difference(ΔT_c) across the fluid layer, the buoyant forces are sufficiently high to overcome the dissipation mechanisms. The uniform state of zero fluid velocity is destabilized even by thermal fluctuations resulting in the flow of fluid between the plates. The onset of this primary instability has been well understood from linear stability analysis developed by Rayleigh[51] and is well characterized by the dimensionless parameter known as the Rayleigh number(R). The primary instability occurs at a critical Rayleigh number($R_c \approx 1708$, evaluated at a temperature difference across the plates of ΔT_c)[10].

$$R = \frac{\alpha g d^3 \Delta T}{\nu \kappa}, \epsilon = \frac{R - R_c}{R_c}$$

Another parameter often used is the reduced Rayleigh number ϵ; the onset of convection occurs when $\epsilon > 0$. The Prandtl number, the ratio of the kinematic viscocity, ν, to the thermal diffusivity, κ, plays an important role in the structure of patterns formed. In our experiments we work with gases that are characterized by a Prandtl number close to 1. The vertical thermal diffusion time, $\tau_\nu = d^2/\kappa$, sets the time scale for the flow.

In the equations above, we have assumed the physical parameters describing the gas, namely the density ρ, thermal expansivity α, kinematic viscosity ν, thermal conductivity K and heat capacity C are constant throughout. This assumption is known as the Boussenesq approximation. Under this approximation, the flow in Rayleigh-Bénard systems is symmetric about reflections about the midplane [28].

The onset of convection is marked by a change in the state of the fluid from being at rest everywhere to regions of up-flow (hotter, lighter fluid) and down-flow (cooler, denser fluid). These regions form regular patterns with the flow taking on roll like structures.

The dynamics of the flow along the temperature gradient does not show as much variation as along the horizontal plane for low ϵ. The flow is highly confined in the vertical direction and in many cases it is interesting to look at the evolution of the flow projected along the horizontal plane. The length scale of these patterns is governed primarily by the depth of the fluid layer.

Close to onset, the convection rolls often form parallel stripes(Figure 3). The dimensionless wavenumber of such a pattern at onset is computed to be $3.11 (= 2\pi d/\lambda_c)$, λ_c being
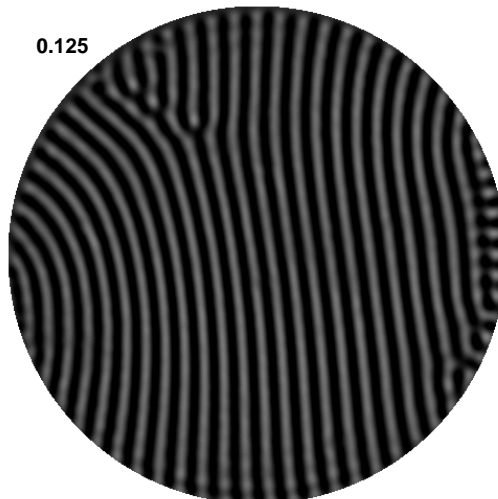
Figure 3: A parallel set of straight rolls seen close to the onset of convection ($\epsilon = 0.125$ in our experiments on RBC.

the wavelength of the pattern at onset[10]. In our experiments, the critical wavenumber or the critical temperature difference are used to compute the depth of the fluid layer. For stationary parallel rolls, the horizontal velocity of the fluid averaged over the depth of the fluid at a given horizontal spatial location is zero. This averaged quantity is a measure of the "mean flow" within the pattern along the horizontal plane [12, 44, 45].

The convection patterns may undergo further instabilities resulting in a change in the topology of the roll patterns. The various mechanisms for linear instability for infinite parallel convective rolls have been characterized by Busse [6, 7, 16] and are mapped out over variations of the Rayleigh number, wavenumber and Prandtl number. The stable region for ideal straight rolls within this parameter space is referred to as the Busse balloon. While this stability balloon has been developed for the ideal case of infinite stationary parallel rolls, it is nevertheless useful as an intuitive (and quantitatively approximate) guide for finite aspect ratio systems or systems where curvature of the rolls may be significant and with time dependence [22].

2.3 *Spiral Defect Chaos*

Spiral Defect Chaos is a recently discovered state of RBC exhibiting complex spatiotemporal behavior arising in a region of the Busse balloon previously associated with stable stationary

parallel rolls [42, 43, 49, 15]. The state has been exclusively seen in convection with gasses, where the Prandtl number is close to one, suggesting that part of the complexity may be attributed to the competing mechanisms of viscous and thermal dissipation. Experimental work by Morris et. al.[42, 43]. has demonstrated that SDC occurs between moderate($\Gamma \approx$ 30) to large aspect ratios($\Gamma \approx 100$). The mechanism of the onset of SDC, especially being in a regime bistable with ideal straight rolls(ISR) is an open question and has been explored experimentally as well as numerically[49, 12, 9]. The Busse balloon has been devised for an idealized state of parallel convective rolls, however, the occurrance of SDC projected (using the mean wave number of the complex state) is still unexpected. The state of convection can undergo seemingly spontaneous transitions between regions dominated by SDC and ISR while all experimental parameters of the system are maintained to be the same. Many investigations have highlighted the sustenance of SDC as being described by the interplay of wavenumber distortion[22], mean flow induced curvature of the rolls[13], defect-turbulence[20, 21, 23] and frustration due to multiple wave numbers for the state[17].

The development of defects in the convective state is associated with the merging and formation of rolls. Such events are characterized by a variation in the local wave number akin to the instabilities of ideal straight rolls bounding in the Busse balloon [22]. The curvature of the rolls in the neighborhood of defect formations changes and this results in mean flows. In an interesting numerical study of SDC, the quenching of mean flows also resulted in stationary patterns of a higher wave number, with the rolls evolving to straight segments intersecting at very angular vertices [13].

A significant insight into the instabilities resulting in the complex behavior focused on analyzing the linear stability of the state of SDC. It was noted that the linearized equations for the state were often most sensitive to perturbations in a local region for a short period of time[23]. The anecdotal evidence has been that these regions correspond to regions of defect nucleation. This study has emphasized the role of defect nucleation driving the chaos and showed that the chaos in the system was extensive.

Figure 4 illustrates a typical shadowgraph image of convective flow in the regime of SDC.

Figure 4: The shadowgraph image above illustrates the complex configuration of convection rolls in spiral defect chaos (SDC) - a name motivated from the spontaneous occurrence of spiral structures. The above state corresponds to $\epsilon \approx 1$, with a fluid layer depth of about 600 microns. The diameter of the convection cell imaged above is 3.8 cm.

CHAPTER III

EXPERIMENTAL TECHNIQUES

3.1 Motivation for design

Rayleigh-Bénard experiments have had a rich and instructive history in the study of pattern forming systems[16]. There is extensive experience in theoretical, numerical and experimental approaches to studying pattern formation in this system. In particular, experimental systems have an advantage of being able to follow the system state for long times with frequent sampling. In these experiments it is also not difficult to change some of the critical system parameters that are of prime importance in theoretical and numerical considerations, in particular the Rayleigh number and aspect ratio.

Many patterns exhibited in RBC have been observed through experimental investigations [15], with theoretical considerations providing qualitative insight into some of these patterns. Recent advances in numerical techniques have made it feasible to have exact quantitative comparisons with experiments, especially for small aspect ratios (about 10-40) or short intervals of time (a few hundred vertical thermal diffusion time scales). With further advances in computational abilities, it should be possible to extend this to a variety of experimental geometries even at large aspect ratios. The experiments measure only limited aspects of the flow - there is little information on the exact three dimensional velocity field of the fluid. Nevertheless, the qualitative structure of the flow may be inferred even from reduced information provided by measurements such as shadowgraphy(akin to a projection of the velocity along the vertical direction). These seemingly gross measurements of the flow are however ample in describing much of the dynamics at length and time scales pertinent to the complex behavior exhibited. The essential roll structure of the flow seen at onset is retained at higher ϵ. The structure of the rolls is the most striking aspect of the pattern, and the change in their configurations represent sufficient information to track the trajectory of the system.

The characterization of spatiotemporal complex systems often require details beyond the measurement of a single trajectory. The evolution of densities of neighboring trajectories play an important role in understanding chaotic evolution[18]. This requires the ability to evolve an ensemble of neighboring initial conditions in experiments. In our experiments, we use thermo-optic actuation to reproducibly impose initial patterns of the convective rolls and study their subsequent evolution.

In the remainder of this chapter, details of our experimental setup are discussed.

3.2 Convection cell

We use CO_2 gas as the working fluid in our convection experiments. The convection of the gas occurs between two horizontal plates (the top plate and bottom plate), the separation between which may be varied, and temperature of each controlled independently. The convection is detected through a shadowgraph technique that is sensitive to refractive index variations in the cell. These variations within the fluid are induced through inhomogeneous density distributions during convection. The thermal expansion coefficient of CO_2 increases significantly with pressure at room temperatures. The gas is therefore pressurized for good shadowgraph signal within a canister known as a convection cell.

The apparatus of the convection cell used in our experiment is adapted from a previous experimental setup used to study modulated pattern formation in RBC [52], which was based on designs by J. de Bruyn et. al [19]. The primary alterations have been to incorporate the ability to impose initial conditions on the flow by thermo-optic means. Details of this modification to the cell and the accompanying optical systems are discussed in a later section.

The essential design for our experiments on convection is to have control over the heat flux across the fluid layer, the depth of the layer and the pressure of the fluid. Other parameters for convection are controlled by the choice of fluid. A schematic of the experiment is detailed in Figure 5.

The $CO_2 (K \approx 0.2 \text{W/m K})$ in our experiments is confined between two good thermal conductors to maintain spatial homogeneity of the temperature at the bottom and top
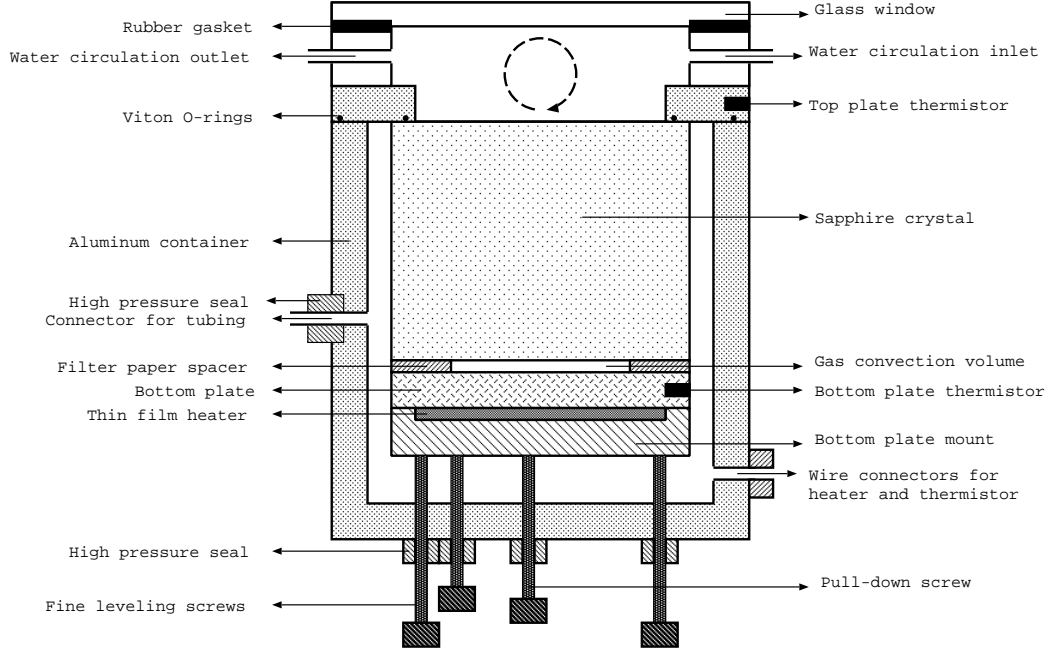
Figure 5: Schematic of the convection cell.

boundaries of the fluid. The top plate is a 2.54 cm thick sapphire crystal($K \approx 34$W/m K) that also acts as a pressure window for the cell. The sapphire crystal is transparent to light in the visible spectrum, which helps with the visualization of the flow as well as thermo-optic imposition of patterns as discussed later. Water at a constant temperature circulating over the top surface of the sapphire window regulates the top temperature of the convection cell. A thermistor embedded within the upper cover of the cell reading this temperature. The bottom plate is a gold coated Aluminum($K \approx 240$W/m K) mirror 5 cm in diameter and 0.6 cm thick. The lower surface of the mirror is mounted on a steel support that rests on a set of leveling screws. A thin film heater is sandwiched between the mirror and the steel support to control the temperature of the mirror by controlled heating. A thermistor embedded within a hole drilled into the side of the mirror monitors the bottom plate temperature. In the experiments involving thermo-optic actuation, the metal mirror is replaced with a composite layered structure discussed in section 3.4.

The temperatures of the top plate and bottom plate as monitored by the thermistors is used to control the power supplied to the thin film heater. The resistance of the thermistors is read by a Hewlett-Packard(Model 3420) digital multimeter, and the heater powered with a

single phase power supply. The multimeter and power supply are interfaced with a PC using a National Instruments LabPC card. A PID algorithm implemented in LabView maintains the temperature difference between these plates to within 10mK at the temperature ranges we work with(15°C - 40°C)[60]. Changing the temperature difference across the fluid layer is the easiest way to alter the Rayleigh number in the experiment.

The separation between the top and bottom plate is supported by a stack of filter paper. This stack also acts as the lateral boundary confining the convective flow. Finer control of the separation is enabled by three leveling screws (Newport 1/4-80 Fine Adjustment Screws) that the circumference of the bottom plate mount rests on. A further screw is hooked to the center of the bottom plate assembly to hold it firm. The uniformity of separation between the plates is checked by laser interferometry with a low power He-Ne laser. The separation between the plates, typically about 600 microns, controls the approximate wavelength of the roll pattern. The wavelength of the pattern at onset as well as the critical temperature difference between the plates at onset may be used to compute the separation between the plates.

The casing of the convection cell is an Aluminum cylinder 6.75 cm long with 6.93 cm inner and 8.95 cm as outer diameters. This holds CO_2 gas at a pressure of 3.2 MPa maintained by a pressure regulator attached to a pressurized tank filled with 99.99% CO_2. The connection between the regulator and convection cell is through NPT pressure fittings and clear 0.3 cm tubing. A pressure release controlled by a Swaglock Nupro plug valve allows for the convection cell to be purged. In addition, a pressure sensor monitors drifts in the pressure within the cell. While connected to the pressurized tank, the pressure within the cell is seen to be constant to within the measurement errors of the gauge.

3.3 Flow visualization

The convection rolls form the important structural features of the pattern. The orientation of these rolls is measured by a shadowgraph technique [55]. This technique is sensitive to spatial refractive index variations. In our system, a variation in the refractive index is seen across regions of hotter upflows and cooler down flows of the convection rolls(Figure 6). The

refractive index varies with the density of CO_2 with denser (down flowing) regions having a higher refractive index than lighter (up flowing) regions. The strong variation of refractive index in pressurized CO_2 makes it possible to perform shadowgraphy even with thin layers of the fluid due to the ample refraction of light within the fluid layer.
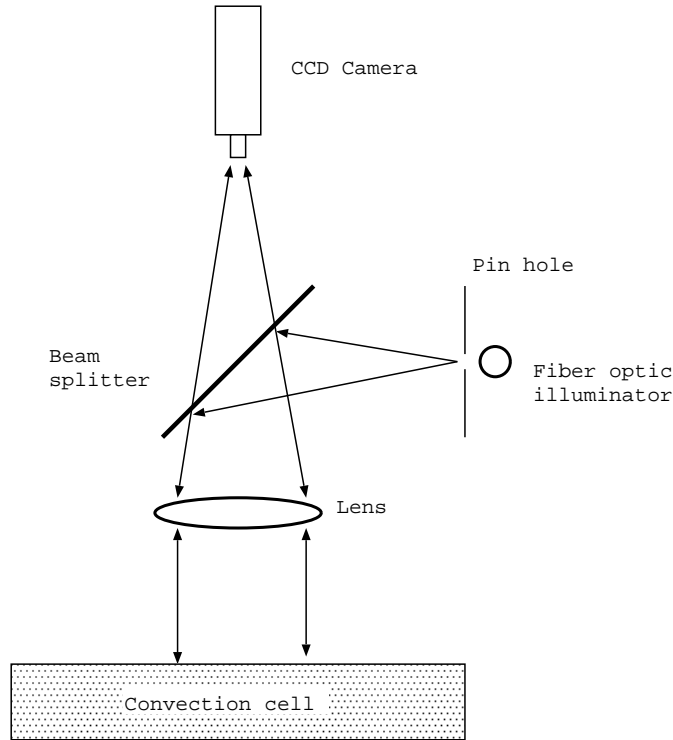
Figure 6: The shadowgraphy setup as implemented in the experiment.

The experimental setup for shadowgraphy used in our experiments is shown in Figure 6. A high intensity fiber optic illuminator in conjunction with a pin hole or iris is used at the focus of a convex lens(focal length of 50cm) as a source for collimated light. This light is passed through the top sapphire window of the convection cell and reflected back by the bottom plate, passing through the convective layer of fluid. The reflected light is imaged by a CCD camera(initially a SONY 8-bit camera, later changed to a DVC-1312 monochrome camera with 12-bit resolution fitted with an adjustable zoom lens) with the CCD array a small distance away from the plane of focus. The camera captures an intensity image representative of the refractive index variation across the flow. The camera is connected with a frame grabber board to stream data directly the hard disk (imaging at about 15Hz)

or RAM (at about 40Hz) of the computer. Software by EPIX is used extensively in image acquisition.

The shadowgraph technique is sensitive to changes in the illumination. The fiber optic illuminator is connected to a DC power supply to eliminate periodic variations in light intensity from AC power sources. The intensity of light from the fiber optic illuminator may be controlled by varying the power supplied to the bulb, or changing the diameter of the pinhole/iris. We find halogen bulbs with mirror reflectors of the EV series to be a good source in the illuminator. The ambient light in the room is reduced to a minimum during experimental runs as well.

Extracting the details of the refractive index profile from shadowgraph images is non-trivial and requires many details of the optical setup and gas properties. For our studies it suffices to have consistent quantitative measures of the patterns exhibited, without details of the flow such as exact velocity measurements [55, 19].

3.4 Thermo-optic actuation

3.4.1 Optics

The patterns in RBC are buoyancy driven. Our approach to actuating the flow is to heat the fluid locally to induce hot upflows. Controlled local heating, in terms of spatial location and power, carried out across the entire convective region lets us manipulate the state of fluid flow in a manner not possible earlier. In our experiments, we use local heating in addition to the global thermal gradients conventionally imposed.

Local control of flows in experimental setups of RBC have been incorporated using thin wires embedded in the lateral sidewalls in successfully suppressing boundary driven instabilities [15]. High intensity lamps have also been used previously in conjunction with masks to bias states of the fluid flow [11, 8]. Our technique borrows from this later approach aided by advancements in the available technology since these early experiments.

We cause local thermal actuation by focusing a laser beam at the region of flow within the convection cell. Laser emission in the visible wavelengths of light is transmitted without significant loss of power through sapphire, water and glass that form the top ensemble of

the convection cell. Light in the visible spectrum is not absorbed by the CO_2 gas either and the local heating of the gas is by creating hot spots on the bottom plate that conductively transfer heat to the gas. The gold coated Al mirror is replaced by a composite layered structure engineered to maximize optical absorption of the laser radiation while meeting reasonable mechanical, optical and thermal requirements for visualization and convection. Spatially distributing the laser radiation across this bottom plate biases the convective flow to organize in a pattern commensurate with the optical imposition.

The optical imposition of patterns utilizes a spatial variation in the Rayleigh number to influence the convective flow. In regions where the local value of ϵ is high, instabilities in the flow may be induced and often cause time dependent structures. This limits the applicability of our technique to low Rayleigh numbers where the convective rolls formed mimic the optical field imposed. At higher ϵ it is possible that nonlinear aspects of the hydrodynamics dominate, leading to a departure from a linear response of the flow to the temperature profile of the bottom boundary. The optical technique as we used can only increase the local Rayleigh number. It would be useful if a mechanism for local cooling may also be implemented.

Two approaches to imposing the spatial optical pattern were developed. The light source in both these techniques used an Ar-ion laser(Coherent Innova 100 or Spectra Physics model 2020) tuned for emission in all lines mode. The power of the beam could be maintained up to about 17 Watts, but in typical applications this was set to about 2 Watts. The laser emission is primarily in the visible spectrum.

The initial implementation for spatial modulation of light used an existing setup of computer interfaced galvanometric mirrors. The laser beam was reflected off two galvanometric mirrors that could rotate about axis perpendicular to each other. The synchronized motion of these mirrors under computer control would raster the beam over a desired path across the bottom plate of the convection cell. The light beam was focused by a combination of lenses to create an intense spot at the bottom plate. A similar setup has been in use for imposing flows in Benard-Marangoni convection[54]. This raster technique worked well in setting simple patterns for the flow that were intrinsically stable. In some instances a

local instability of such patterns could be suppressed by controlled actuation at the desired location. This technique was especially fruitful in suppressing boundary driven instabilities by imposing thermal boundary conditions by a continual raster of the beam at the lateral boundaries of the flow. The patterns were perturbed by point perturbations corresponding to brief localized pulses by the laser directed within the bulk of the pattern to probe stability.

When destabilizing mechanisms like defect formations at boundaries were frequent, the speed of raster was not sufficient to externally stabilize the pattern as described above. The fastest local variation in the flow occurs at τ_ν, the vertical thermal diffusion time. The imposition of intricate patterns to study complex states requires the ability to raster the entire pattern on a time scale faster than the vertical thermal diffusion time. This is necessary so the entire convective state may be imposed simultaneously, without instabilities occurring during imposition.

One of the approaches tried was to project the desired optical pattern within the convection cell using a MEMS spatial light modulator. This device (Texas Instruments DMD) consists of an array of microscopic mirrors(a rectangular array about 2cm on a side, with 1024×768 individual mirrors) whose orientation can be flipped between two states very fast. Light incident on this array is spatially modulated by the controlled switching of individual mirrors between these two states, 'on' and 'off' - the 'on' state directs the light into the convection cell. The disadvantage of this technique was the significant loss of light intensity - the laser beam is expanded to the size of the DMD and the light used during imposition is gathered only from mirrors toggling to the 'on' state. While this technique allowed for practically instantaneous imposition across the cell with 8-bit intensity resolution, the associated loss of power did not permit pattern imposition within the convective flow effectively. The MEMS device described above is used in commercial light projectors, illuminated by high intensity lamps. While these systems do not yet meet the power requirements of our systems, they have been used in other fluid experiments, most notably in thin film flows by Garnier *et al.* [26].
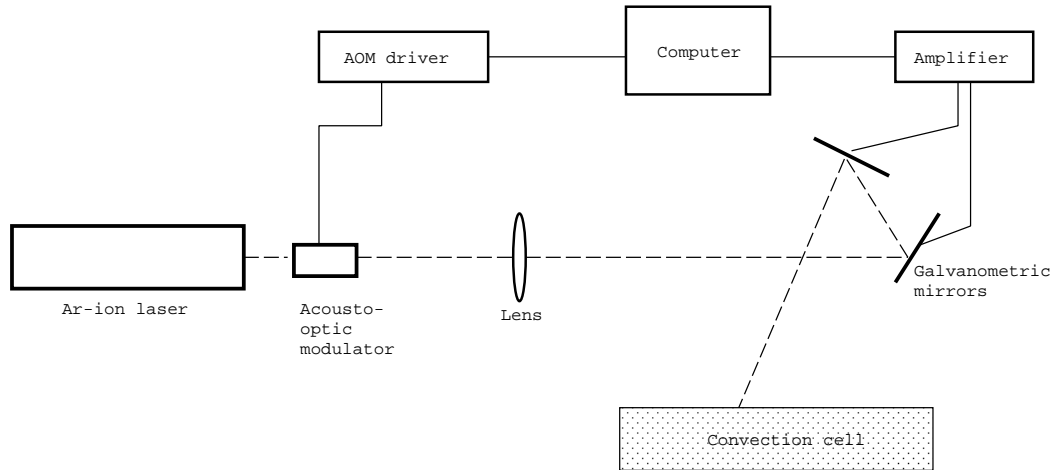
Figure 7: Schematic showing the optics and electronics for thermal imprinting of patterns.

The efficiency of local heating by rastering a laser beam led us to develop a faster scanning system that is now the workhorse for pattern imposition in our experiments (Figure 7). All the components for such a system are commercially available as separate modules. The primary ingredient for the system are two fast scanning galvanometric mirrors(GSI Lumonics model G120D). This assembly consists of mirrors attached to galvanometers that are controlled by a precision amplifier(Lighting Systems and Design, Inc. model : Turbotrak) connected to computer. The amplifier sends a precise current through the galvanometer coils to deflect the mirrors. Software (LaserShow Designer) and an interface board made by Pangolin are used for computer control of the amplifier. In addition, a Acousto-optic modulator(Neos Technologies: Model 35085-3) is used to vary the intensity of the beam. Used in conjunction with the galvanometric mirrors, the AOM modulates the intensity of the beam at a desired spatial location to 8-bits of resolution. The scanning system used has the capability to raster up to 60000 points every second. Additional software was written to interface the scanning system with Matlab.

3.4.2 Bottom plate

The other aspect of optical imposition that we expended considerable time and effort on was optimizing the light absorption at the bottom plate of the cell. Convection experiments usually aim to have a bottom plate at a constant and uniform temperature. This is done

by using materials with a high thermal conductivity, such as Aluminum or Silicon wafers. Such materials are counterproductive in our scheme of local heating as they dissipate heat through the bulk before there is significant heat transfer to the fluid.

We use an optically flat glass substrate as the bottom plate bounding the fluid. Specular reflection from the glass surface is essential for shadowgraph visualization. The glass is a neutral density filter(NDF) with an optical density of 3, absorbing the laser radiation. The laser radiation is incident from the top of the convection cell, with maximum absorption occurring close to the fluid-NDF interface. The incident beam is about 100 microns in diameter at this location. The absorbed heat is conducted by the fluid as well as within the glass. The glass is mounted on a good thermal conductor(an Al plate embedded with a thermistor, or a silicon waver 0.5 cm thick) heated by a thin film heater to maintain a temperature gradient across the fluid in addition to the laser heating. A good thermal contact between the glass substrate and the conductive mount improves the temperature control of the bottom plate, as well as the thermal profile imposed optically. In the absence of good thermal contact, the temperature of the glass substrate uniformly rises from laser light absorption, hampering the imposition of patterns. The glass substrate is bonded to its mount using heat sink compound or a UV cured glue(Figure 8).
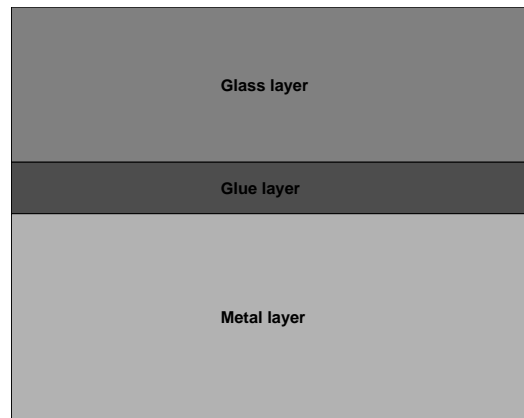
Figure 8: The schematic of the composite layered structure built to improve thermal contrast during laser imposition. The glass thickness of the glass substrate was varied. The glue comprised of either heat sink compound or UV cured dark glue. The metal support was 0.5cm thick.

The size of the hot spot caused by the light absorption is determined by the diffusion

of heat through the substrate and fluid. The horizontal spread of the heat within the glass is reduced when the region of light absorption is close to the heat sink, improving the contrast of the thermal imprint. Simple numerical models of the diffusion of heat through the composite layers were used to gain insights into the contrast of thermo-optic imposition. These simulations are discussed in Figure 9. A thinner glass substrate is suggested to be more desirable for our thermal imposition.

Initial experiments of our system relied of NDF glass substrates 3 mm thick(Schott NG-1), resulting in poor thermal contrast, hampering imposition of the flow field in convection (Figure 9). The thinnest self-supporting glass substrates available are about 50 microns(Schott D-263)to 70 microns(Corning Inc. : corning 0211) thick. These substrates are transparent to the laser radiation, and are mounted on silicon wafers using a black UV cured glue(Bohle black UV glue). The glue forms a layer about 100 microns thick between the glass and silicon. The light absorption occurs within this layer of glue, and is found to achieve good thermal contrast resulting in the best control for pattern imposition in our convection experiments. Strong heating by the laser can cause the glue layer to 'melt', deforming the substrate. The composite layers described are not mechanically stiff. Bowing in these substrates causes a non-uniform depth across the fluid layer. Further, when pressurized, such a composite layer is suspected to show dynamics of its own - the onset temperature of convection is seen to fluctuate by almost a degree when monitored over a few hours, suggesting a dynamic variation in the depth of the fluid layer.

A compromise between thicker, mechanically stronger substrates and the thinner composites is desired. The NDF initially used was ground down to a variety of thickness. While this reduced the optical density, it improved the thermal contrast of imposition, while not compromising the mechanical stability too much. A substrate 1mm thick, bonded to a aluminum plate by heat sink compound was used in our experimental setup.

The experimental techniques of optically driving the flow requires considerable refinement before it may be used as a robust tool to impose patterns in the experimental setup. Such refinements could benefit from guidance through accurate numerical simulations on the hydrodynamic response to local heating and material characteristics.
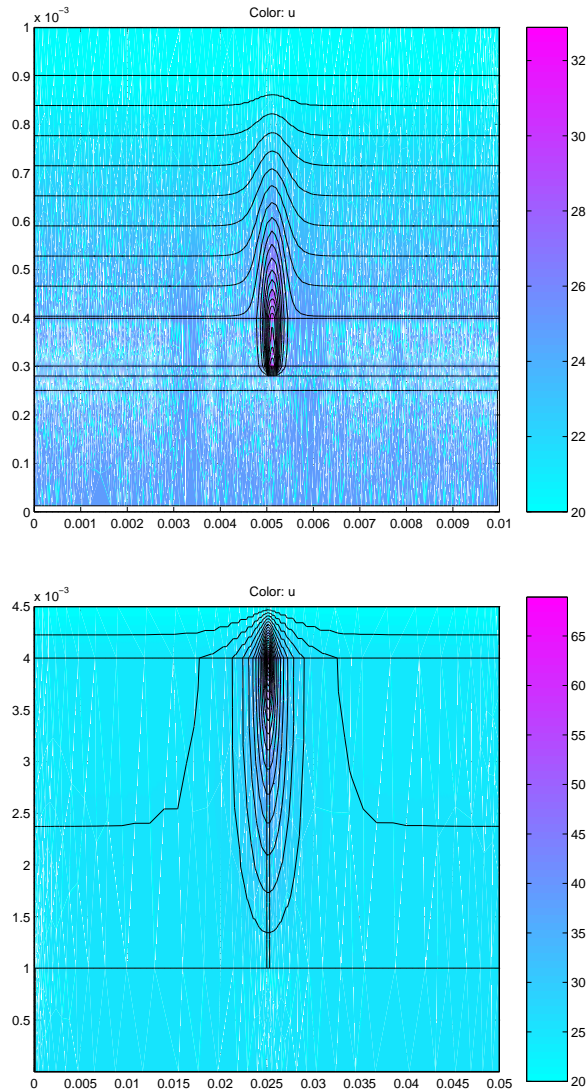
Figure 9: Results from a simple two dimensional simulation of the vertical cross-section of the convection cell in response to the heating caused by laser imposition. The upper figure models a composite layer structure comprising a 100 micron glass substrate bonded with glue over a metal plate (bottom). The light absorption occurs within the dark UV glue. A gas layer within which pattern imposition is to be carried out is the topmost layer in both the figures. The lower figure indicates the poor thermal contrast when a 3mm glass sheet is mounted over metal. The simulations were performed using the partial differential equation toolbox in Matlab. The color code represents the temperature field (u) in °C. The x and y coordinate axis are in meters. The model describes the diffusion of heat through materials comprising the composite structure and the gas. The various materials are differentiated by their thermal conductivity.

In the following section we describe the experimental procedures used in our investigations of patterns found in RBC.

3.5 Data collection and analysis

The primary data collection in our experiments comprises of the shadowgraph images representing the convection in the flow. In addition to this, records of the temperatures of the top and bottom plate as well as the pressure of the gas are maintained. The mean temperature of the fluid, the critical temperature difference at onset and the wavenumber of the emergent convective pattern form important parameters for the dynamics. These parameters may be used to compute the depth of the convection cell. We do this using code developed by the group of Guenter Ahlers at the University of California, Santa Barbara. The code incorporates the empirical equations of state for CO_2 and has been extensively used in the convection community[52].

The shadowgraph images capture the state of flow in the system along with artifacts associated with measurement noise or optical non-uniformities. The data is processed to capture the primary dynamics of interest. Stationary optical non-uniformities are usually caused by inhomogeneous reflectivity of the bottom plate, non-uniform illumination or at times dust in the optic path. Subtracting a reference image, such as a shadowgraph image captured prior to the onset of convection can eliminate these features. High frequency noise is intrinsic to any CCD based imaging system, showing up as intensity fluctuations at each pixel of the CCD array. The dynamics we image is at a length scale larger than the length scale associated with such noise. For our purposes Fourier filtering the data is seen to sufficiently eliminate distortions from this source of noise. The entire convection setup, including the associated optics is mounted on a optic table with pressurized gas dampeners to reduce vibrations. In addition, refractive index variations through the water circulation over the sapphire crystal are also picked up by the shadowgraph imaging. There is scattering of laser light during pattern imposition that may not be completely eliminated by the band-pass filter used in the camera.

There have been two thrusts for the procurement of data in our studies. The first(Chapter 4) looks at the evolution of an ensemble of similar states of the system for short times with the aim of characterizing chaotic evolution. Here we setup the system to enable thermo-optic imposition of patterns. The bottom plate consisting of a composite layer of 1mm

thick NDF in thermal contact with an Aluminum plate using heat sink compound. The second(Chapter 6) characterizes the long time dynamics of the system by describing the topological configurations taken by rolls at different ϵ. The state of the system is observed at a variety of ϵ after waiting sufficiently long (about $10^3\tau_\nu$). Here the bottom plate consists of a gold coated Aluminum mirror.

CHAPTER IV

LINEAR STABILITY FROM EXPERIMENTS

4.1   The challenge in experiments

In many spatially extended systems exhibiting complex patterns, it is desirable to build tools to achieve feedback control to direct the evolution towards a target state[41, 59, 47, 35]. There have been attempts at such control by treating global variables as control parameters for the system, however, not all target states may be attained by such an approach[31, 30, 32]. Being able to manipulate the local dynamics provides for more flexibility in controlling the future evolution[33]. In addition, local control of the dynamics could be more efficient in terms of the energy input needed to guide the system, as well as the computational effort required.

One of the primary difficulties with implementing local control is the lack of understanding of the origin of complex dynamics in spatially extended systems. Identifying the dynamical features relevant to the future evolution of these systems is an aspect that is still under investigation and an extension of the tools and techniques developed in the study of low dimensional chaotic systems is not straightforward due to the infinite dimensional space the trajectory evolves in[2, 4, 48].

The trajectory of such systems typically exhibit complex patterns of similar qualitative features, while the details at different instants of time are distinct[14]. The notion of such evolution representing a strange attractor described by the closure of unstable fixed points and periodic orbits motivates the characterization tools we develop in this chapter. We extract a reduced order model for the linear manifold describing the neighborhood of fixed points and periodic orbits with the intention of using well developed tools of linear control theory. The hyperbolic manifold of such neighborhoods scatter the trajectory of the system between unstable periodic orbits and fixed points. Experimental control over the hyperbolic manifold of linear instabilities can direct the future evolution of the system.

We wish to control a system by a set of perturbations that direct trajectory to a desired target state. In experimental systems, while we can measure the trajectory of the system, there is almost no information on neighboring trajectories that small perturbations may direct the evolution towards. For short times, the neighboring trajectories describe the linear manifold that is needed to develop schemes to control the evolution of the system. One of the salient features of the experiments we perform is the ability to impose patterns and perturb their evolution in a controlled manner, as described in Chapter 3. This is used to generate reproducible initial conditions about which small perturbations yield an ensemble of neighboring trajectories describing the linear manifold imperative to linear control schemes.

In the remainder of this chapter we describe our approach to characterizing such linear manifolds. In the next section we motivate the role defects play in the dynamics of spiral defect chaos and the importance of characterizing the linear manifold about these events.

4.2 The role of defects

Numerical [23] and experimental [36, 21, 20] investigations have suggested defect nucleation as being pivotal events dominating the complexity of the evolution in SDC. The structures of the defects in a complex pattern of SDC are hard to define and are intuitively described as local regions where the local symmetries of parallel rolls is broken. The underlying notion in such a description is that SDC may be looked upon as a state of parallel rolls destabilized by multiple spatially and temporally distributed defects. The statistics of such defects has been investigated [20, 21] to yield quantitative measure of their influence. Other related explorations have measured the roll curvature, local wavenumber and roll to spiral transitions [36].

The description of SDC as defect mediated turbulence has been further corroborated by numerical investigations by Egolf et. al. [23]. The Navier-Stokes equations modeling SDC at each time step were also evolved without the nonlinear terms. These linearized equations showed that they were most sensitive to perturbation at regions that were spatiotemporally localized. This investigation was also used to compute the Lyapunov exponents for the

system and demonstrated that the chaos in the system was extensive. The authors state that "the localization of the Lyapunov vectors with positive exponents is correlated with regions of the pattern that are linearly unstable due to the rolls being too narrow or too wide". Regions of the pattern with extremum values for the local wave number result in the formation of defects [22].
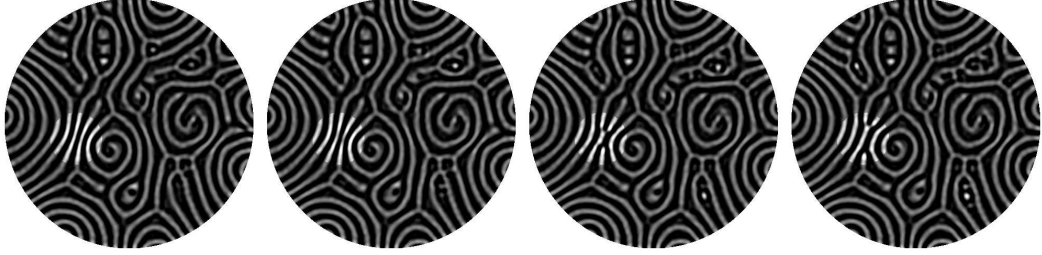
Figure 10: In the image time series shown, a site of defect formation in SDC is highlighted. The images shown are sampled at about twice every vertical thermal diffusion time. Also noteworthy in this figure is that the remainder of the pattern shows no large-scale motion at this time scale. Defect formation in SDC are spatiotemporally localized events resulting in topological rearrangements of the pattern. These events are pivotal to the complex evolution. Numerical simulations have also suggested that Lyapunov vectors corresponding to such states are localized about these events. The almost parallel roll structure in the neighborhood of defect nucleation as illustrated above motivate the congruence to instabilities of ideal straight roll patterns.

The extensive nature of chaos indicated by Egolf et. al. [23] suggests that distant regions of the pattern evolve in an uncorrelated manner. In this light, it might be sufficient to have a description of the local dynamics related to defect nucleation in order to capture the dynamically significant aspect of the pattern evolution(Figure 10). When defect nucleations are sufficiently well separated, the fundamental domain for the pattern may be reduced to isolated defect nucleation events.

Our approach to achieving global control is through controlling the local instabilities (associated with defect nucleation) resulting in the global complex evolution. In order to do so, we develop tools that may characterize these local mechanisms. This characterization builds a reduced order model for the dynamics, relevant to the evolution of the system in the neighborhood of a local linear instability leading to defect nucleation. The modes and growth rates extracted are of prime importance in implementing control. From an

experimental viewpoint, the defect nucleations may be regarded as independent of each other and the description of single defect nucleation translated and rotated appropriately can be used to characterize and control (via appropriate feedback) the chaotic dynamics of the entire pattern.

4.3   Approximate invariant manifold

Spatiotemporal systems, such as RBC, are embedded in infinite dimensional spaces, however, it is possible in some cases to develop models that approximate the dynamics to good accuracy in a finite dimensional space. In experimental systems, the bound on the maximal dimension defining such a space is limited by the resolution of the measurement - the resolution of the CCD camera used to image the flow in our case. A good choice of a basis may significantly improve the convergence for the accurate representation of the state of the system, capturing the significant evolution in a lower dimensional space than the experimental measurement directly yields.

In SDC the recurrence of defect nucleation across the systems suggest that they may be representative of important "coherent" events. The coherence in these structures results from the dissipation in the system, limiting the evolution to a bounded space. In what follows, we describe an experimental technique developed to extract an "approximate invariant manifold" (AIM) to efficiently track the evolution of coherent structures such as defect nucleation.

The local spatial neighborhood prior to the occurrence of a defect in SDC has the symmetries associated with parallel rolls as seen in Figure 10. The local wavenumber of this base state of locally parallel rolls may be considered close to an instability as for the infinite system at the boundary of the Busse balloon. In this sense, the instabilities of parallel straight rolls may be considered canonical to those occurring in SDC. We therefore focus our attention on developing the AIM for the instabilities of an ideal state of parallel rolls. To experimentally extract this manifold, we sample the evolution of the state as it progresses through these instabilities. A complete description requires such sampling to be carefully chosen, accounting for all possible states the system may undertake while

undergoing the instability. We achieve such ergodic sampling by selecting initial conditions across the basin of attraction leading to instabilities for the base state of parallel rolls. This selection is guided by symmetries of the system. The ability to span and choose a variety of states in a controlled manner in experiments is a unique feature of the experimental techniques we have developed.

The experiments begin by using laser heating to impose a well-specified basic state of stable straight rolls. The basic state is typically arranged to be near the onset of secondary instability by imposing a sufficiently large pattern wavenumber such that at fixed $\epsilon (\approx$ 0.4 in our case) the system's parameters are near the skew-varicose stability boundary [6, 7, 16]. In this regime, the modes responsible for the instability are weakly damped and, therefore, can be easily excited through externally induced disturbances. The modes leading to the instability are best described when the evolution of the system in response to such a disturbance is linear. For patterns that are stable to an arbitrary disturbance, the regime of linear evolution may be preceded by nonlinear evolution, however, close the base state when the disturbance has decayed sufficiently, the contribution of the nonlinear influences may be deemed insignificant. In our experiments we will be primarily interested in characterizing this later regime of the evolution.

The linear stability of the basic state is probed by applying brief pulses of spatially localized laser heating. For stable patterns, all small disturbances eventually relax. Each time the system is perturbed it excites modes of the system with different amplitudes. The relative amplitude of the modes excited depends on the details of the perturbation applied: the strength of the perturbation as well as its spatial location. To excite all modes governing the disturbance evolution, we apply a set of localized perturbations consistent with symmetries of the (ideal) straight roll pattern – continuous translation symmetry in the direction along the rolls and discrete translation symmetry in the perpendicular direction plus the reflection symmetry in both directions. Therefore, localized perturbations applied across half a wavelength of the pattern form a "basis" for all such local perturbations – any other localized perturbation at a different spatial location is related by a translation and reflection symmetry. Localized perturbations are produced in the experiment by aiming

the laser beam to create a "hot spot" whose location is stepped from the center of a (cold) downflow region to the center of an adjacent (hot) upflow region in different experimental runs. The perturbations typically last approximately 5 s and have a lateral extent of approximately 0.1 mm, which is less than 10 % of the pattern wavelength.
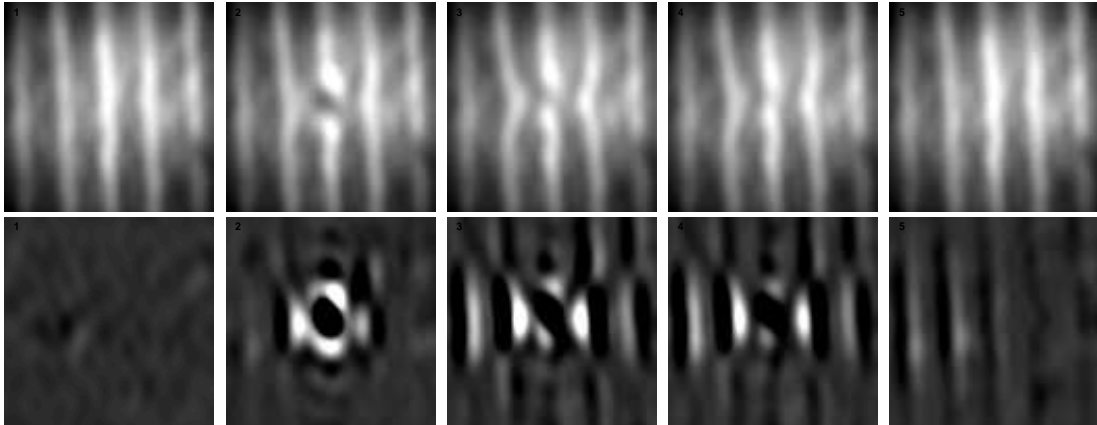
Figure 11: A sequence of shadowgraph images showing the base state of the system and its response to a perturbation. The upper sequence details the progression in response to a "symmetric" perturbation applied between the center of two hot rolls. Dark regions mark hot upflows and brighter regions indicate cooler downflows. The lower sequence of images are difference images - the base state subtracted from the upper image sequence. These difference images enhance the deviation from the base state in response to a disturbance.
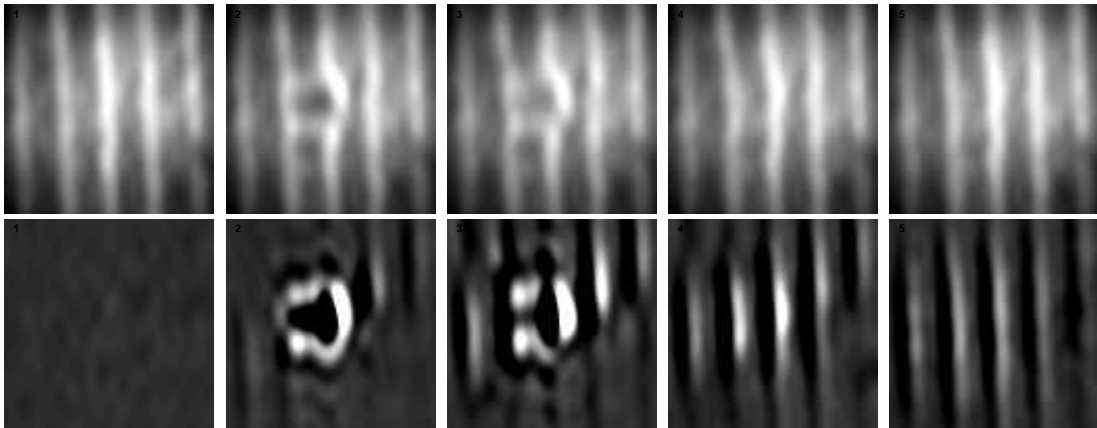
Figure 12: A similar set of images as in the previous figure. The perturbation in this case is imposed off-center. The subsequent evolution is seen to be devoid of the symmetry seen earlier. The aplitude of modes excited varies with the location and strength of the perturbation. The regime of linear evolution corresponding to such disturbances is of interest to us.

The evolution of the perturbed convective flow is monitored by shadowgraph visualization. A digital camera with a low-pass filter (to filter out the reflections from the Ar-ion laser) is used to capture a sequence of 256×256 pixel images recorded with 12 bits of intensity resolution at a rate of 41 images per second. A reference image, the mean of the states during linear evolution, is subtracted from each data image; such sequences of difference images comprise the time series representing the evolution of the perturbation (Figures 11 and 12).
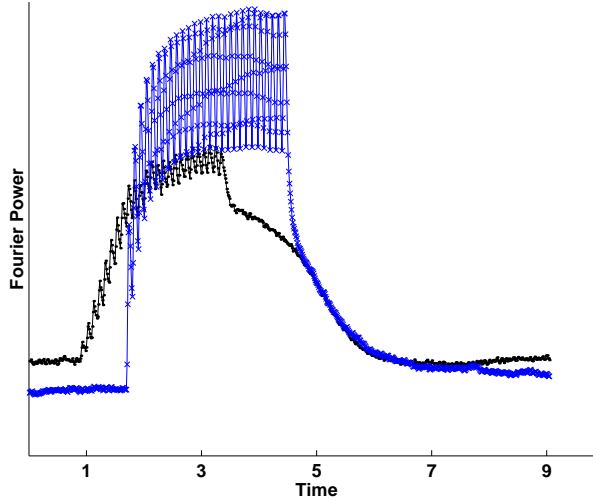
Figure 13: The Fourier power evolution for the two image time series, corresponding to the location of the perturbation on the center of a cold roll(marked by filled circles, Fig 11) and off-center(marked by filled crosses, Fig 12)indicated in the earlier figures. The exponential part of the above curves are used in estimating the regime of linear evolution. The large oscillations seen are due to laser light scatter while the perturbation is being applied.

To estimate the regime of linear evolution, we compute the decay of the spectral power following the perturbation. The total power for each image in a time series is obtained from 2-D spatial Fourier transforms. The resulting time series of total power shows a strong transient excursion (corresponding to the initial nonlinear response of the convective flow to a localized perturbation by laser heating) followed by exponential type decay as the system relaxes back to the stable state of straight convection rolls. We restrict further analysis to the region of exponential decay, which typically represents about 3.5 seconds of data for each applied perturbation. If the system is described by a single mode, the decay would be exactly exponential. When there are multiple modes with similar growth

rates present a deviation from exponential decay is not unexpected. The spectral power described in Figure 13 represents the superposition of the modes excited by the disturbance and while each mode may decay exponentialy, their sum may not show exponential decay.

The dimensionality of the raw data is too high to permit direct analysis, so each difference image is first windowed(to avoid aliasing effects) and Fourier filtered by discarding the Fourier modes outside a 31×31 window centered at the zero frequency. The discarded high-frequency modes are strongly damped and contain less than 1% of the total power. This also serves as a filter for high-frequency noise associated with the CCD imaging. The basis of 31^2 Fourier modes still contains redundant information, so we further reduce the dimensionality of the embedding space by projecting the disturbance trajectories onto the "optimal" basis constructed using a variation of the Karhunen-Loeve(KL) decomposition [34, 56, 57].

The KL decomposition, or proper orthogonal decomposition is a technique to extract an appropriate axis from a sample of points. These axes minimize the least-square projection of all the points used in the construction of the coordinate system. As an example, if the sample of points form the circumfrence of an elipse in two dimensions, the KL decomposition of these points yields the major and minor axis of the system. The procedure requires the construction of a correlation matrix from the sample data set, whose eigenvectors form the coordinate system.

In our analysis, the correlation matrix in constructed from a sample data set representing members of the ensemble of trajectories sampled during their linear evolution. The correlation matrix C is computed using the Fourier filtered time series $\mathbf{x}^s(t)$,

$$C = \sum_{s,t} (\mathbf{x}^s(t) - \langle \mathbf{x}^s(t) \rangle_t)(\mathbf{x}^s(t) - \langle \mathbf{x}^s(t) \rangle_t)^{\dagger}, \tag{4}$$

where the index s labels different initial conditions and the origin of time $t = 0$ corresponds to the time when the perturbation applied by the laser is within the linear neighborhood of the stationary state. The angle brackets with the subscript t indicate a time average. The matrix C is a symmetric, with every element being positive definite. The eigenvectors of C are the KL basis vectors. It is worth noting that the average performed to compute

38

C represents an ensemble average over different initial conditions (obtained by applying different perturbations); this is distinctly different from the standard implementation of KL decomposition where statistical time averages are typically employed[62].
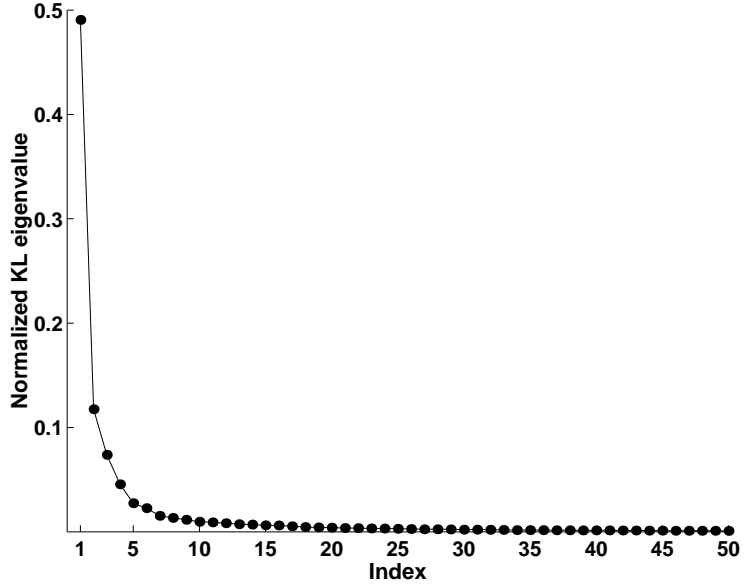
Figure 14: The spectrum of eigenvalues for the correlation matrix indicates the relative amplitude of the KL vectors, in describing the space of which they form a basis. Here the normalization is done with the total power - the sum of all the eigenvalues.

The eigenvalues of the correlation matrix, C, represent the contribution of the corresponding eigenvector in the sample space used to construct the correlation matrix, as in Figure 14. We find that the first 24 basis vectors capture over 90% of the total power, so an embedding space spanned by these vectors represents well the relaxation dynamics about the straight roll pattern.

The spatial structures of the first few KL vectors are shown in Figure 15. In our convection experiments, the KL eigenvectors show two distinct length scales. The first two dominant vectors are spatially localized, while the remaining vectors are spatially extended. This is consistent with earlier work as suggested by Egolf *et al.* [22]where they suggested a separation of scales - one describing defect nucleations, and the other related to global relaxations that may be associated with mean flows.
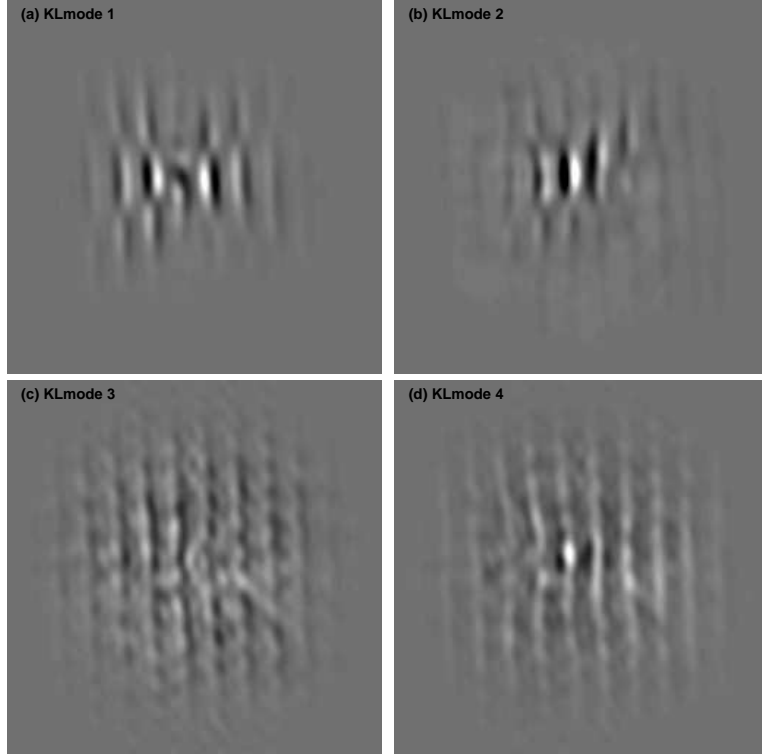
Figure 15: The Karhunen-Loeve eigenvectors corresponding to the four highest eigenvalues. These vectors form an optimal basis to describe difference images as indicated in the previous figure.

4.4   Modes and Growth rates for defects

The Karhunen-Loéve decomposition builds a basis to capture the dominant dynamics resulting from excitations about a stationary state, corresponding to parallel rolls in our experiments. The disturbance about the stationary state of straight rolls may be considered as a superposition of eigenmodes for the system. The linear regime of the excitation may be parameterized in terms of these modes, their amplitudes and growth rates in addition to the fixed points about which the system is excited. In experiments the stationary state typically shows some weak time dependence associated with slow drifts in the parameters. We assume such drifts to be negligible on the time scales at which each individual perturbation decays, however may be significant over the period data for the entire ensemble of perturbations is collected. Quantitative information can be obtained by finding the eigenmodes of the system excited by the perturbation, and their growth rates. The decay of the perturbations in the linear regime may be modeled by:

$$\mathbf{x}_i^s(t) = \mathbf{x}_i^s(\infty) + \sum_{k=1}^{\infty} A_k^s \mathbf{m}_i^k e^{\lambda_k t}$$

where $\mathbf{x}_i^s(t)$ is a projection of the perturbation at time t in the time series s onto the ith KL basis vector. In the fit $\mathbf{m}^k$ and λ_k are the kth eigenmode and its growth rate and A_k^s is the initial amplitude of the kth eigenmode excited in the experimental time series s. The fixed points $\mathbf{x}^s(\infty)$ are chosen to be different for the differing time series in the ensemble to account for a slow drift in the parameters. In theory the modes for disturbances form a continuous spectrum, however we use a simpler picture of a discrete set of modes. The discretization in experimental systems may result from the finite aspect ratios, forming bounds to the dynamics.

These can be extracted from a nonlinear least squares fit with the cost function

$$E_n = \sum_{i,s,t} \left[\mathbf{x}_i^s(t) - \left(\mathbf{x}_i^s(\infty) + \sum_{k=1}^{n} A_k^s \mathbf{m}_i^k e^{\lambda_k t} \right) \right]^2,$$

While ideally there are an infinite number of modes excited in the system, we limit ourselves to extracting only n of them. The optimization procedure should extract the most dominant modes excited by the perturbation. The optimization of the parameters of the fit was implemented using a nonlinear least squares minimization routine in Matlab, `lsqnonlin`.

The experiments typically consisted of sets of an ensemble corresponding to about twenty perturbations. This amount of data is excessive for the optimization problem, restricted by memory usage during the computation. We therefore weighted the initial conditions based on their mutual projections on each other and select only seven of the ensemble for modal extraction. These seven projections were selected as being with the least projection on each other, thus maximally spanning the modal space.

To have a faster convergence for the nonlinear least squares routine, we first extracted a single mode with $n = 1$ above, using random initial guesses. The parameters from this extraction were incorporated into guesses for the case where $n = 2$, with the additional parameters given random initial guesses. This procedure was followed, increasing n sequentially. At each value of n, 25 realizations for the noise were used for the additional parameters. The result corresponding the lowest value of the cost function was chosen as the best fit.

The computation takes about 10 days to run on a single high end workstation to extract parameters corresponding to $n = 6$. The residual from this optimization was 0.01.

4.5 Results
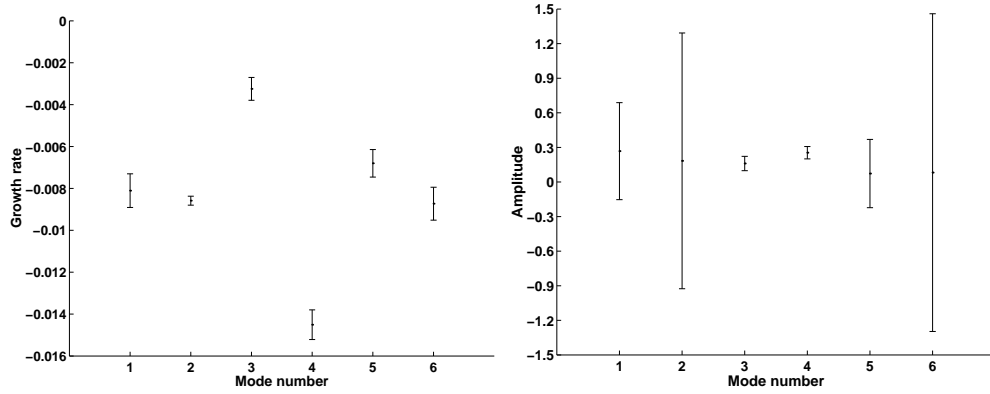
Figure 16: The spectrum of growth rates, λ(left) and the amplitudes, A (right) extracted to parameterize the instabilities of straight rolls. In this particular case, the growth rates are all negative, consistent with the base pattern being stable - all disturbances applied are damped out. The instability of the pattern would be dominated by the modes corresponding to positive growth rates.

The extracted growth rates λ_k are shown in Figures 16. Not surprisingly, since the pattern is stable the growth rates are negative. The leading eigenmode (see Figure 17) is spatially extended and shows a diagonal structure characteristic of the skew-varicose instability in an unbounded system. This is also expected as the pattern is near the skew-varicose instability boundary. The second eigenmode is spatially localized and has no analog in spatially unbounded systems. The subsequent modes are again spatially delocalized and likely correspond to the Goldstone modes of the unbounded system (e.g., overall translation of the pattern) which are made weakly stable due to confinement by the lateral boundaries of the convection cell.

The modes and growth rates are used to describe the phase space(Fig. 18) corresponding to the local instabilities of straight rolls. Such extraction of the linear manifold in experiments on spatially extended systems without the knowledge of the dynamical equations of the system aids in the extension of techniques that are well developed for low dimensional systems. The manifolds of fixed points and periodic orbits are of particular interest in
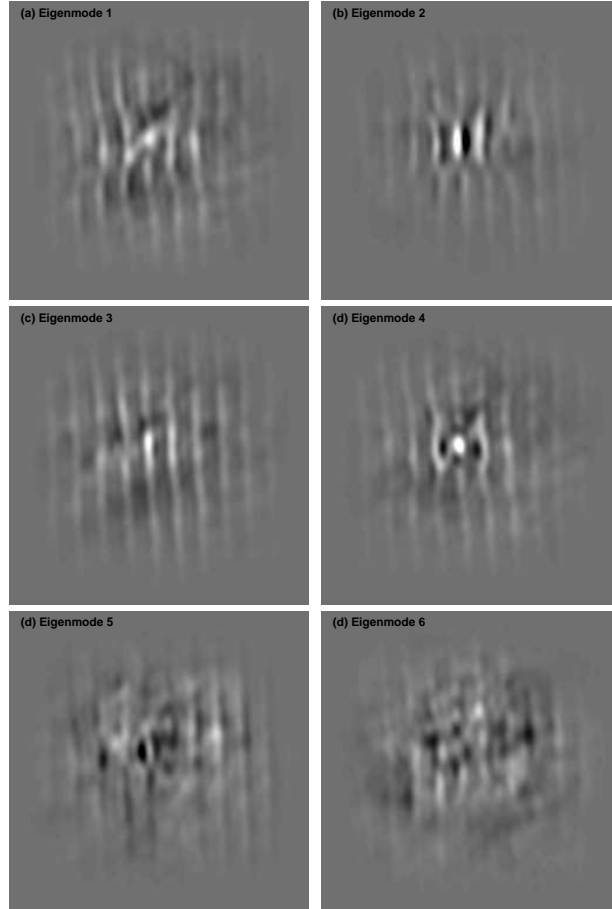
Figure 17: The first six eigenmodes extracted from the data. Some of these modes show a skew structure resembling the skew-varicose instability of infinite straight rolls. These modes correspond to disturbances close to the skew-varicose boundary of the Busse balloon.

chaotic systems and their control.

If the system is brought across the stability boundary, one of the modes is expected to become unstable (without significant change in its spatial structure), thereby determining further (nonlinear) evolution of the system towards a state with a pair of dislocation defects. We would also expect the spatially localized eigenmodes (like the second one in Figure 17) to preserve their structure if the base state is smoothly distorted (as it would be, e.g., in the SDC state shown in Figure 16), indicating the same type of a spatially localized instability.

We also attempted to realize trajectories that evolve from unstable patterns of the straight roll state. This was done using a composite layer for the bottom plate as described in Chapter 3 comprising of a transparent sheet of glass about 70 microns thick bonded to

a silicon wafer with a dark UV cured glue. This composite structure provided for good pattern imposition in response to thermo-optic actuation, but lacked mechanical strength.

The experimental system was unsuccessful in impositions of straight roll patterns with wavenumbers outside the stability balloon, due to the inherent hydrodynamic instability. However, in stable patterns close to the skew-varicose boundary, one could trigger defect formation through continual local heating using the laser. The laser power used for creating the hot spot was maintained to a minimum needed for the system to go unstable. While the global structure of the rolls is stable within the Busse-balloon, the local heating raises ϵ locally, resulting in defect formation. A variation of the location of local heating results in the evolution of different trajectories, indicated by the progression through different roll patterns after defect formation.

The different trajectories referred to above are to be contrasted with the experiments performed with no defect formation, as described earlier in this chapter. In the earlier case, perturbations about the same (reproducible within experimental limitations and measurements) base state excite a spectrum of modes to different amplitudes. In the case of unstable patterns, the initial state of the flow is different due to the different spatial locations of the continual raster of the laser to create a hot spot. Ideally, we would like to briefly perturb the same base state as it undergoes a linear instability. Our inability to impose unstable
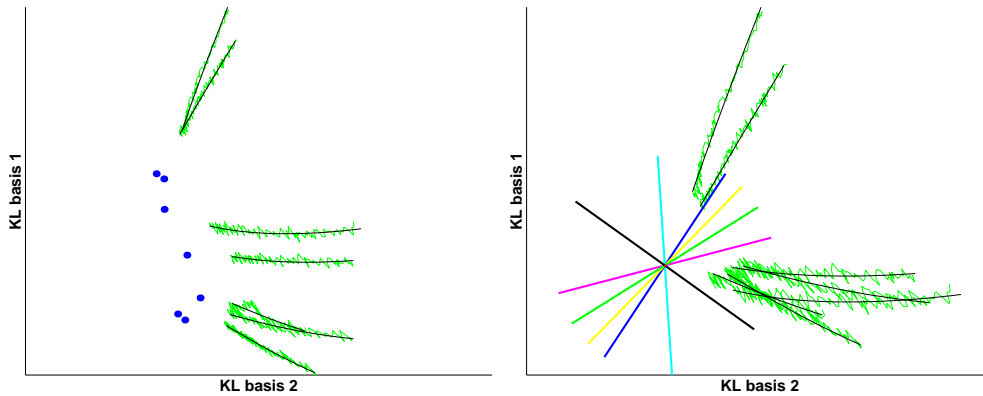
Figure 18: The projection of the experimental time series and the least squares fit on the plane spanned by the first two KL basis vectors. The fixed points have been shifted to coincide in the picture on the right, while the image on the left indicates the drift in the state as measured by the scatter in the extracted fixed points. The different colored lines represent projections of the six modes extracted.

states reproducibly prevents us from doing this.
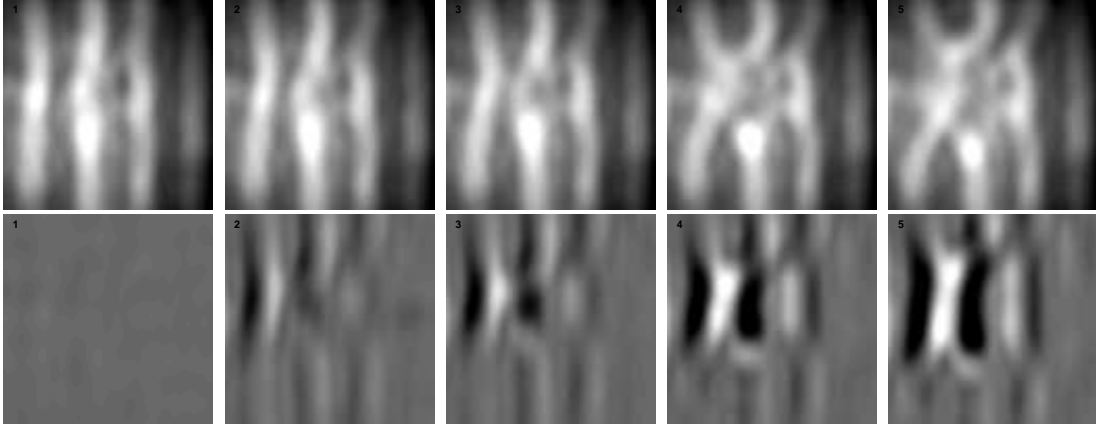
Figure 19: The progression of defect formation is seen in response to continual laser heating. In the lower image the deviation from the initial state of the flow is seen as a difference image - the initial state is subtracted from the images in the upper row. The roll may pinch off to connect to a neighboring roll to the left, right or symmetrically gliding out of the field of view to reduce the local wavenumber.

For a system were governed by linear evolution, the critical slowing down close to the unstable fixed point would suggest that the time to defect nucleation would vary over long times. We find that the time for the defect to nucleate from the continual laser raster is roughly 100 seconds, varying only by about 30 seconds through a variation in the location of the laser hot spot. The reproducibility of this time suggests that the system is strongly biased. The strong bias may result in an imperfect bifurcation for the system, making our search for a linear manifold about the fixed point difficult in this case. One source of strong bias in the system may be through the bottom boundary bounding the fluid. As mentioned, the bottom plate is not mechanically stiff, and bowing in it causes significant depth variations across the convective cell.

The departure from linear response is also supported when one attempts to compute the growth rates and modes for the system. The trajectories are seen to be far away from the fixed points, and the residual for the optimization of the fit is large, as indicated in Fig. 24. Some qualitative similarities in the structure of the KL modes(Fig. 20) and eigenmodes(Fig. 23) are seen when compared to those of stable patterns. In particular, the leading eigenmode, with a positive growth rate maintains a skewed structure, suggesting a

primarily skew-varicose type instability.

The following figures summarize the results of analysis similar to that in Chapter 4.
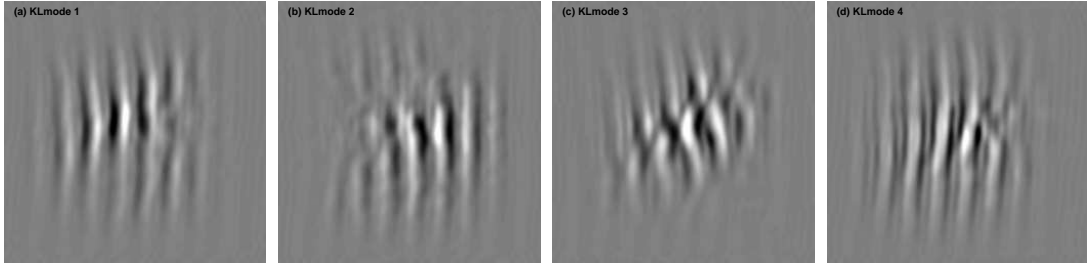
Figure 20: The basis vectors for the instability described in the earlier figure through the Karhunen-Loeve decomposition. Some of the basis elements show qualitative similarities to those in Fig. 15 describing the instabilities of stable straight rolls
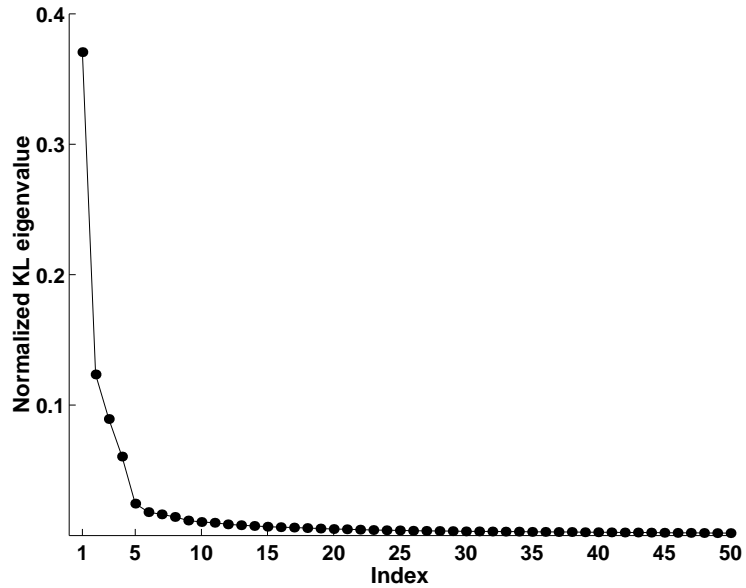
Figure 21: The spectrum of eigenvalues for the correlation matrix indicates the relative amplitude of the KL vectors, in describing the space of which they form a basis. The normalization is done with the total power - the sum of all the eigenvalues. We use up to 20 of the basis vectors to capture 90 % of the space.

Defects represent a type of "coherent structure" in spiral defect chaos. Previous efforts have used coherent structures to characterize spatiotemporally chaotic extended systems in both models [56] and experiments [50]; the use of coherent structures to parameterize the invariant manifold was pioneered by Holmes *et al.* [34] in the context of turbulence. In practice coherent structures are usually extracted using the Karhunen-Loéve (or proper
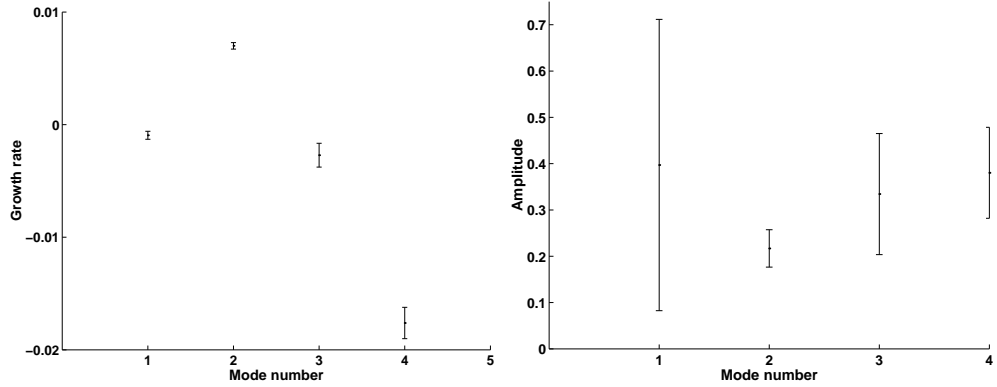
Figure 22: The spectrum of growth rates indicates at least one positive mode in the figure on the left. This mode would be primarily responsible for the defect formation in the base state, growing exponentially. This is to be contrasted with Fig. 16 where there were no hyperbolic manifolds. The amplitudes of the various modes extracted are seen in the plot on the right. Only four modes were extracted through nonlinear optimization.
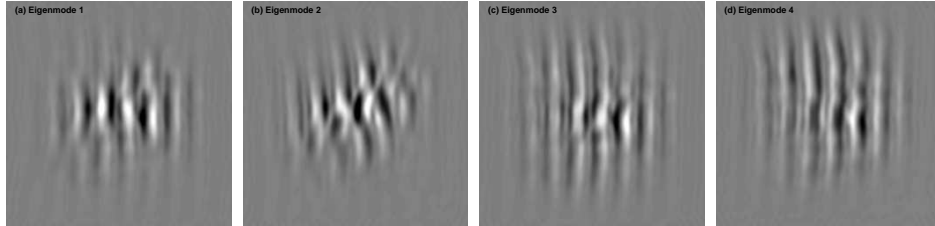
Figure 23: The structure of the second mode has the largest and positive growth rate. This mode is amplified while the others are damped. The skew structure is predominant as is qualitatively seen in Fig. 17, indicative of being close to the skew-varicose boundary of the Busse balloon.

orthogonal) decomposition of time series of system states, which picks out the *statistically* important patterns. This prior work has met with only limited success – indeed, it is unclear whether statistically important patterns are *dynamically* important. A similar methodology has also been used that combines principal component analysis and multitaper harmonic analysis to extract the statistically significant spatial and temporal response from optical imaging data from the cat primary visual cortex[57].

An alternative approach has been proposed by Christiansen *et al.* [14], who suggested instead to use the recurrent patterns corresponding to the low-period unstable periodic orbits (UPO) of the system, which are dynamically more important. Our work sets the stage for attempting the more ambitious task of extraction of UPOs and their stability properties from experimental data.
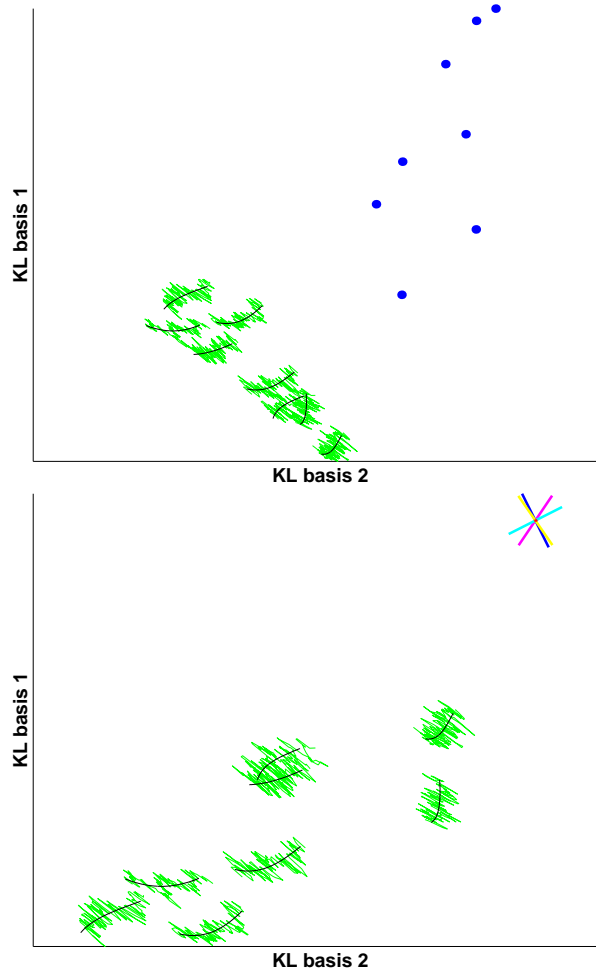
Figure 24: The projection of the experimental time series and the least squares fit on the plane spanned by the first two KL basis vectors. The trajectories are seen not to lie close to the extracted fixed points, indicating a breakdown of the assumption of linear evolution. The upper figure shows the drifts in the fixed points while the lower figure translates the trajectories so that the fixed points are coincident.

CHAPTER V

COMPUTATIONAL HOMOLOGY

5.1 Measures of complex geometry

Patterns exhibited by physical systems are indicative of their underlying dynamics. Often, these patterns exhibit symmetries that allow the description of the pattern across a large spatial domain with a few parameters. The lattice constants characterize crystalline structures through invariance associated with discrete translational symmetries. In systems with complex geometries, it is difficult to discern quantitative features of the dynamical evolution exhibitted by the pattern.

Capturing the details of complex patterns results in high dimensional data sets. Visualization of these data sets when they form two dimensional structures is feasible, however, such techniques are limited in the insights they uncover, particularly when used to understand structures in higher dimensions. Conventional techniques typically rely on the use of a metric, extracting length and time scales to characterize a pattern. In contrast topological characterizations are scale independent. We propose the use of algebraic topology to determine consistent and robust geometric properties of spatiotemporal complexity. In particular this thesis develops the use of computational homology as a rigorous, systematic, and dimension independent method for characterizing geometric structures.

The homology of a pattern is described by a set of positive integers, called Betti numbers. These numbers are indicative of the connectivity within a structure. As an example, consider the three dimensional structure forming the surface of phase separation in a binary alloy in Figure 25 [25]. The homology of this geometry has been used to determine that that there are no cavities formed within the structure, i.e. there are no regions of either material of the composite that is not connected to the boundary. Further, it is determined that the surface indicated forms a single continuous structure, with exactly 1701 holes in it. Such quantitative measures of geometry provided by homology makes it a unique characterization
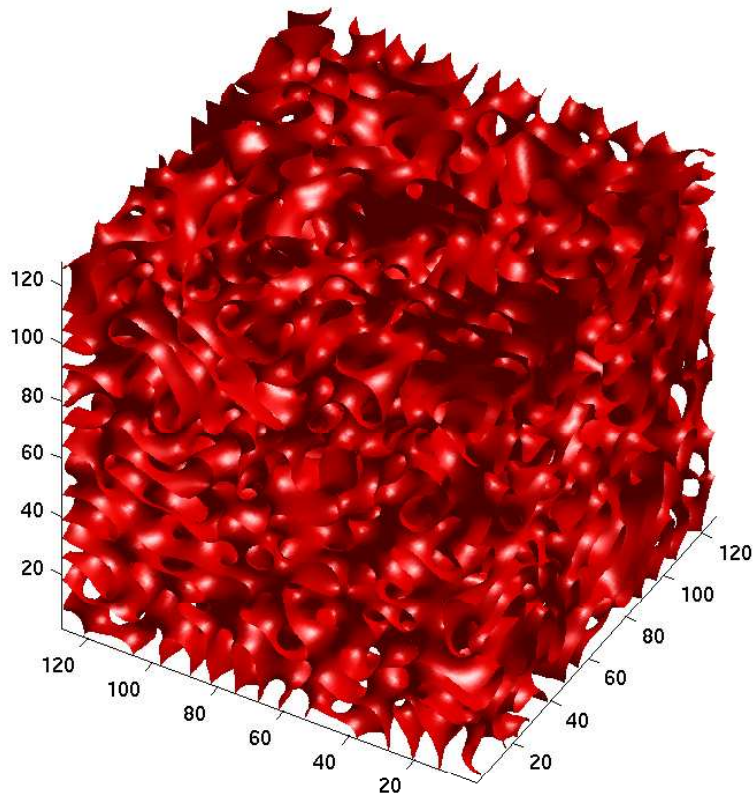
Figure 25: The isosurface indicating phase separation in a binary alloy as modelled by Cahn-Hilliard dynamics. This surface was extracted from numerical simulations of the Cahn-Hilliard dynamics as described in [25]. Computational homology characterizes this structure as being a single continuous structure, with no cavities and 1701 tunnels.

tool for complex structures.

Technological advances in measurement have made possible the measurement of patterns to high spatial and temporal resolution. The large volume of data prompts the use of computers for their storage and analysis. In the following sections we describe the mathematical treatment and computational aspects of extracting the homology of geometric patterns.

5.2 Computing Homology

5.2.1 Cubical complex

The spatial distribution of variables in physical systems is often visually recognized as geometric structures. These variables may have continuous spatial dependence representing topography, concentration, density etc. Some of the geometric structure manifest in the distribution may be preserved by reducing the continuous variation observed to a binary structure. This reduction to a binary image from gray scale is best illustrated through an example as in Figure 26, where the essential features of the geometry for the purposes of computing the homology are preserved, while reducing the information content of the data. Regions above and below a threshold are represented by ones and zeros as indicated in the figure.

The choice of the threshold is critical to the subsequent reduction a continuous distribution to a binary representation. Through the binary representation, the spatial extent of a physical system is segregated into regions representative of distinct attributes of the variables considered. The value of the threshold may be motivated by physical considerations that are insightful in determining relevant regions of interest. For example, the region of zero concentration is used to delineate the surface defining phase separation [25] during alloy formation. In the next chapter, we attempt to segregate regions of upflow and downflow in shadowgraph images of fluid flows. In the absence of any particular choice, a good choice of threshold would correspond to one about which small variations result only in variations of scale in the binary representation. For instance if the threshold value in Figure 26 is close to any of the maxima or minima of the continuous curve, the number of distinct elements in the binary representation would vary, however, away from such regions the number of distinct regions of the binary representation is unaffected.

The reduction to a binary representation is usually achieved by binning data, marking regions above and below the threshold. Such binning is often naturally suggested in experimental data, where spatially extended information is measured at a large number of discrete points forming a cubical lattice. The construction of a binary representation over such integer lattices is known as a cubical complex. Each of the bins used in building the cubical
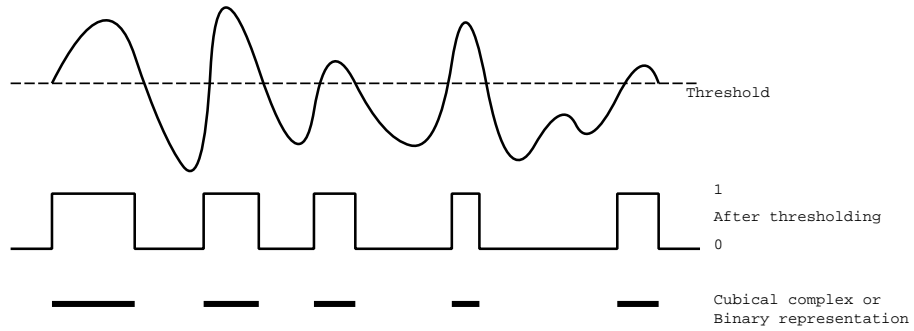
Figure 26: The above figure is a schematic illustrating the reduction of a continuous curve to a cubical complex by thresholding data that varies spatially in one dimension. In one dimension, the number of distinct components counted in the binary representation, five in the above figure, characterizes the homology of the geometry.

lattice is referred to as an elementary cube. We shall be primarily concerned with cubical complexes in two dimensions constructed from digital images acquired by rectangular CCD arrays. In this case, each pixel is a rectangular/square elementary cube. Elementary cubes in n dimensional lattices are also called n-cubes.
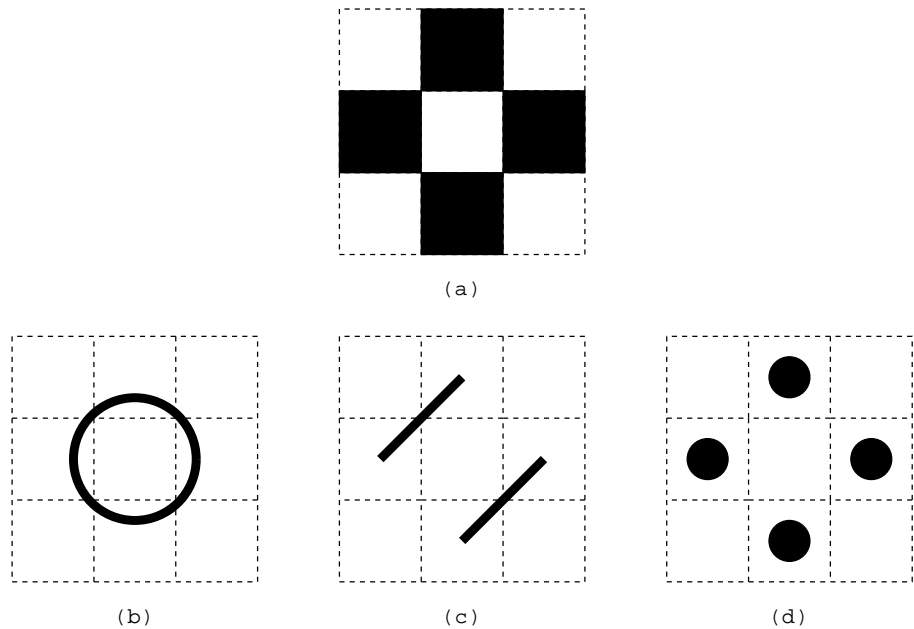
Figure 27: The upper figure (a), represents the cubical complex that may be constructed from any of the lower figures (b), (c) and (d).

The reduction of information by the cubical complex does not uniquely identify the

52

original geometry it was constructed from. This is illustrated in Figure 27. It is possible to construct triangulation that captures the spatial extent of the system studied more accurately than a cubical integer lattice. The techniques described below are adaptable to arbitrary meshes as well, however their implementation for cubical meshes is most straightforward in any dimension. We shall limit our discussion of computing the homology of structures to the special case of cubical complexes in two dimensions. For a more complete treatment of the subject we refer to the text, *Computational Homology* [37].

Each elementary n-cube may be associated with structures in lower dimensions. For example, the boundaries of a 2-cube may be identified as lines that form the edges of the cube. These lines, or 1-cubes, terminate at points that are objects in zero dimensions. Each pixel may thus be constituted of a face(2-dimensional object), edges(1-dimensional object) and vertices (0-dimensional objects). A precise description of a boundary is essential to the mathematical formalism developed for computational homology. We develop this formalism in the the next section.

5.2.2   Homology Computation and the Betti numbers

The paramount step in developing the mathematical machinery of homology lies in associating algebraic quantities with geometric objects. Extracting the homology then reduces to a linear algebra problem, with the dimension of homology groups (described later) counting quantities that are physically interpreted as the number of distinct pieces and enclosed regions.

Consider single element, i.e. a vertex, edge or face, in a cubical complex labeled by a. The quantity $\alpha \hat{a}$, where α is an arbitrary integer may be intuitively associated with this object. We associate an isomorphism between the set of integers, Z, and the algebraic object $\hat{a}$. The quantity $\alpha \hat{a}$ is referred to as a elementary d-chain and is generated by the "basis element" $\hat{a}$, where a is a d-dimensional object.

A geometry consisting of two points, v_1 and v_2, is dual to the elementary 0-chains $\alpha_1 \hat{v}_1$ and $\alpha_2 \hat{v}_2$. The quantity $\alpha_1 \hat{v}_1 + \alpha_2 \hat{v}_2$ is defined in terms of a finite sum of elementary 0-chains, and referred to simply as a 0-chain. The elementary d-chains form the basis for

the d-chains, C_d. The set of elementary chains form a free abelian group when constructed from cubical complexes.
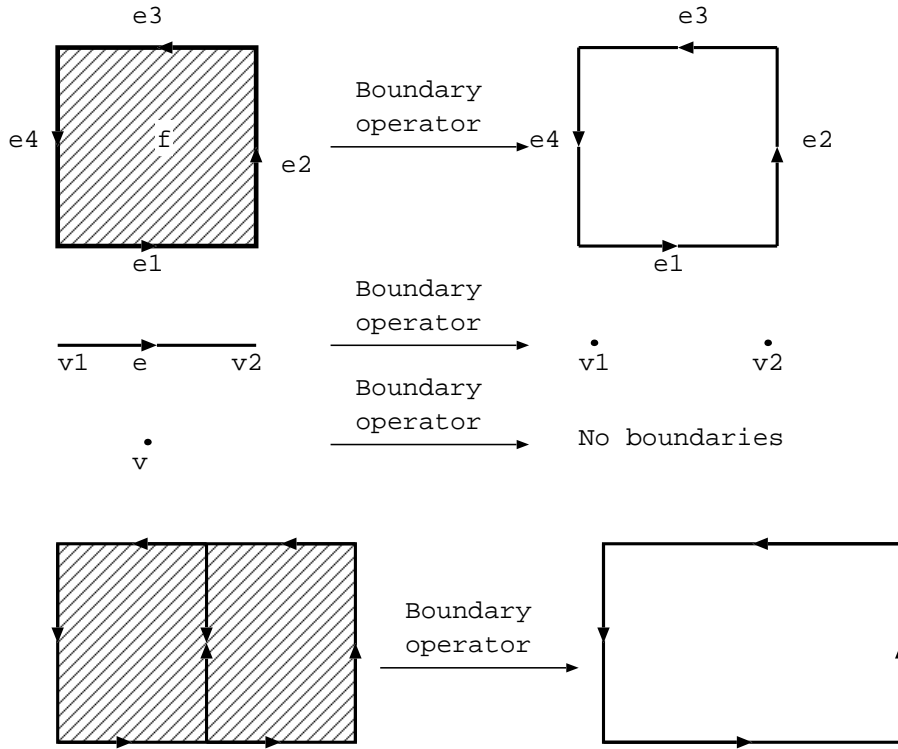
Figure 28: The above diagrams provide the geometric interpretation of the boundary operator.

A boundary operator, ∂ may be associated with algebraic objects and is illustrated in Figure 28. A point in zero dimensions has no boundary, $\partial \hat{v} = 0$. An edge, e is seen to join two vertices v_1 and v_2 through the relationship $\partial \hat{e} = \hat{v}_2 - \hat{v}_1$. The boundary operation defined in this manner associates a directionality for the edge as indicated in the figure. For a face, f, the boundary operator maps out the composition of edges around the face, $\partial \hat{f} = \hat{e}_1 + \hat{e}_2 - \hat{e}_3 - \hat{e}_4$. The need to associate a direction with the boundaries of an object is indicated when an object is composed of two elementary 2-cubes for example(lowest diagram in Figure 28). The side at which these cubes merge have boundary edges in opposing directions, in effect canceling out.

In what follows we shall develop computation of the homology of a simple structure in two dimensions as an illustrative example. Consider the object shown in Figure 29. We shall refer to it as a cubical set, X, that is embedded in a two dimensional space. It consists
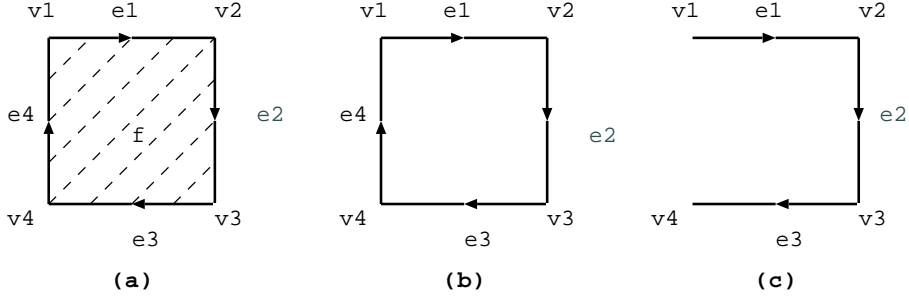
Figure 29: A graph is composed of vertices, edges and faces. In all three graphs shown, there is one connected component. The difference lies in the qualitative features of the connection between the edges, vertices and faces. In (a), the entire graph is connected, with the edges forming a loop around a face that also connects the vertices. On removing the face, f, we get (b), where the edges form a loop, encircling a part of the 2-D space the graph is drawn in. In (c), there are no loops formed by the edges

of four vertices (v_1, v_2, v_3, v_4), four edges (e_1, e_2, e_3, e_4) and one face (f). The chains associated with this object are,

$$
\begin{aligned}
C_0(X) &= \alpha_1 \hat{v}_1 + \alpha_2 \hat{v}_2 + \alpha_3 \hat{v}_3 + \alpha_4 \hat{v}_4 \\
C_1(X) &= \gamma_1 \hat{e}_1 + \gamma_2 \hat{e}_2 + \gamma_3 \hat{e}_3 + \gamma_4 \hat{e}_4 \\
C_2(X) &= \delta_1 \hat{f}
\end{aligned}
$$

where the coefficients α, γ and δ are arbitrary integers. It is worth noting that $C_0(X)$ and $C_1(X)$ are isomorphic to Z^4 while $C_2(X)$ is isomorphic to Z.

In general the boundary operator, ∂ for a cubical set X, maps members of $C_k(X) \to C_{k-1}(X)$. In particular, for a set of edges that form a loop as in Figure 29(b) we have $\partial(e_1 + e_2 + e_3 + e_4) = v_2 - v_1 + v_3 - v_2 + v_4 - v_3 + v_1 - v_4 = 0$. In Figure 29(c) $\partial(e_1 + e_2 + e_3) = v_4 - v_1$. The boundary operator acting on the edges describing the geometric structure yields zero when they form a loop. The existence of a loop indicates a hole in the graph that encloses a region. The loops or cycles in the geometry in any dimension are characterized with their boundaries summing to zero. The total number of loops in the geometry are therefore the number of 1-chains in the cubical complex with boundaries summing to zero.

In two dimensions, a loop may be filled in by the existence of a face, f. In the case of Figure 29, the boundaries of the face, f, are the edges e_1, e_2, e_3 and e_4. It is worth noting

that in this example, the boundaries of the face, f, span all of the edges in the geometry that form closed loops. In more general 2-D structures, the boundaries of all the faces would form a subset of the set of all edges forming closed loops.

In an arbitrary two dimensional graph formed by a cubical complex, the total number of loops would be those formed by edges corresponding to boundaries of a face, and edges that do not form a boundary of a face. The loops that are boundaries of a face do not enclose an "empty" region within them. The actual number of loops in the cubical complex would therefore be the difference of the total loops counted by considering all edges and the number of faces.

The above discussion may be extended to define homology groups in general. The dimension of the group formed by kernel of the boundary operator acting on the kth chain(edges in the example discussed) counts loops formed by the chain. Such a loop may however be filled in by a member of the $k + 1^{th}$ chain (a face in the example discussed). The actual number of loops counted in the kth chain therefore have to be adjusted by the number of members of the $k + 1^{th}$ chains whose boundaries are elements of the kth chains.

The kth-homology groups of a structure are defined as the quotient or factor groups

$$H_k = \frac{kernel(\partial C_k(X))}{image(\partial C_{k+1}(X))}$$

In other words, the homology is the set of cosets of the image of $\partial C_{k+1}(X))$ in the kernel of $\partial C_k(X)$. The cosets thus derived represent equivalence classes contained in the kernel of $\partial C_k(X)$.

The different homology groups H_k are also referred to as the different levels of homology, with $k = 0, 1, 2....$ The dimension of the homology groups are known as the Betti numbers. The Betti numbers may be computed knowing that $kernel(\partial C_k(X) \cong Z^a$ and $image(\partial C_{k+1}(X)) \cong Z^b$ implies $H_k \cong Z^{\beta_k}$, where the kth Betti number $\beta_k = a - b$ is due to the nature of the problem we consider.

5.2.3   Matrix representation

The representation of the boundary operators and algebraic elements discussed above as matrix elements is used during the computation of the Betti numbers. Consider the case

of two vertices v_1 and v_2 connected by an edge e. We may use the following notation to describe the vertices and edges:

$$\hat{v}_1 = \begin{bmatrix} 1 \\ 0 \end{bmatrix}$$

$$\hat{v}_2 = \begin{bmatrix} 0 \\ 1 \end{bmatrix}$$

$$\hat{e} = [1]$$

With this representation, the boundary operator is a $m \times n$ matrix mapping n edges, represented as $1 \times n$ vectors, to m vertices, represented as $1 \times m$ vectors. In our case, this would correspond to ∂ being a 2×1 matrix.

$$\partial \equiv \begin{bmatrix} 1 \\ -1 \end{bmatrix}$$

$$\partial \hat{e} = \begin{bmatrix} 1 \\ -1 \end{bmatrix} [1] = \hat{v}_2 - \hat{v}_1$$

The size of the vector space needed to compute the homology scales with the number of cubes constituting the cubical complex. It is not unusual to have images from experiments (as used in the following chapter) with a resolution of 512×512 pixels. A cubical complex is constructed from half these pixels requires a vector space of dimension $512 \times 256 = 131072$. A substantial reduction in the embedding space may be achieved if the number of elements in the cubical complex are reduced. This makes the computation of the Betti numbers more efficient in terms of the computational time as well as storage requirements.

The reductions in the number of cubes forming the cubical complex is done by eliminating cubes whose removal does not change the homology of the geometry [46]. These reductions in the cubical complex are done by considering the connectivity of each cube through its neighbors. An elementary cube in a cubical complex with d spatial dimensions would have $3^d - 1$ neighboring elementary cubes. We shall demonstrate the procedure for
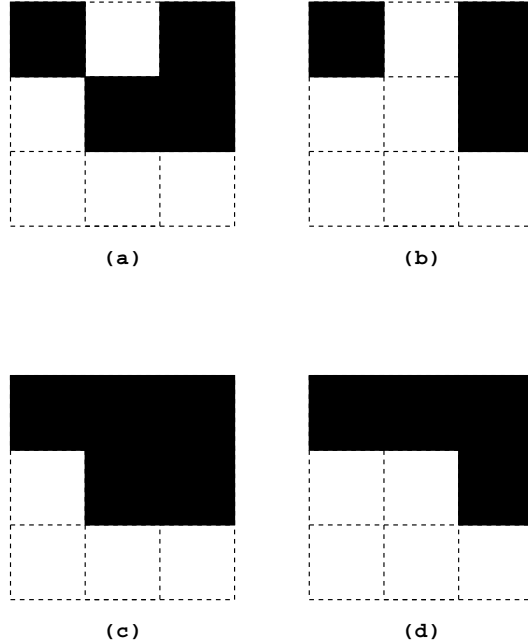
Figure 30: The above figures represent the neighborhood of a single cube in a cubical complex. The pictures demonstrate the procedure to determine if removing the pixel in the center would affect the homology of the entire complex as in [46]. The central cube is connected only to its neighbors. If removing the central cube results in the formation of a set of cubes that may have a trivial homology, i.e. have the same set of Betti numbers as a single point, then removing the central cube would not affect the homology of the structure. In the two upper images, the central cube may not be removed as it results in two distinct regions, while in the lower two images, removing the central cube results in a structure that may be reduced to a point. Removing the central cube in the lower images therefore would not change the global homology of the structure.

reduction in a two dimensional binary image in Figure 30. In the figure, two local neighborhoods where the central pixel is occupied are considered in (a) and (c). The images in (b)(corresponding to (a)) and (d) (corresponding to (c)) have the central pixel eliminated. If the homology of the remaining structure with the central pixel removed is the same as that of a single point, then the central pixel may be discarded, reducing the size of the cubical complex. Such a reduction may be carried out over the entire structure repeatedly until no further reductions are possible.

5.2.4 Physical interpretation of Betti numbers

The Betti numbers have a special significance in terms of their physical interpretation. For a structure embedded in n spatial dimensions, $\beta_k = 0$ if $k > n$. This is easy to see, as

the chains, $C_k = 0$ for all $k > n$ as well. The zeroth Betti number, β_0 represents the total number of distinct components seen in a geometry while the first Betti number, β_1 counts the number of loops in a structure. The second Betti number, β_2 which occurs in three dimensional objects, counts the number of cavities formed within the structure. Subsequent Betti numbers count the number of "voids" in higher dimensional spaces.

As examples the Betti numbers associated with some generic geometric structures are shown in Figure 31.
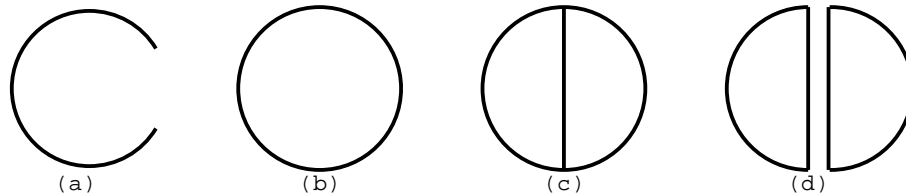
Figure 31: The number of connected components corresponds to the zeroth Betti number, β_0 and the number of enclosed regions the first Betti number, β_1. In the above images, we have for (a)$\beta_0 = 1$, $\beta_1 = 0$, (b)$\beta_0 = 1$, $\beta_1 = 1$, (c)$\beta_0 = 1$, $\beta_1 = 2$ and (d)$\beta_0 = 2$, $\beta_1 = 2$. In all the images shown, the higher Betti numbers, $\beta_{2,3,\ldots} = 0$

The Betti numbers represent scale independent measures describing the topology of a geometric structure. By definition, they are non-negative integers.

5.3 Noise

Computing the homology of a structure from a cubical complex is straightforward as described in the previous section. The accuracy of the technique depends on the cubical complex being a reliable representation of the geometry being considered.

In experimental systems, noise is ubiquitous to any measurement. Figure 32 indicates a schematic of typical distortions brought about by the presence of noise. Image processing techniques to reduce noise in experimental data are well developed. Eliminating noise completely is not feasible in general, and some signatures of the noise are seen in the cubical complex. The spurious structures associated with noise in the cubical complex would be reflected in its homology. Estimating the variation in the Betti numbers of a structure due to noise is an open and interesting problem that we are currently pursuing.

While constructing a cubical complex, a continuous spatial variation is thresholded to
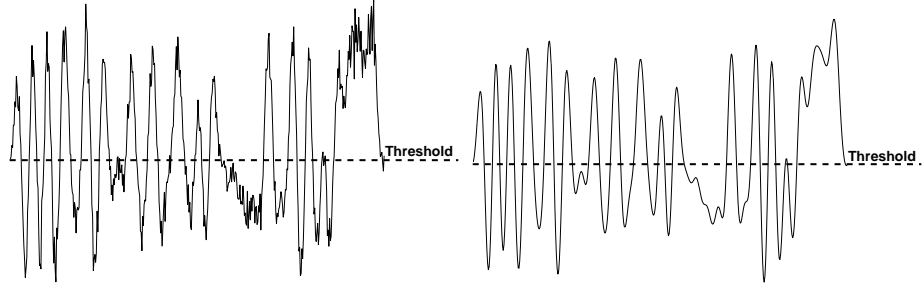
Figure 32: The above plots are schematics indicating the presence of noise in experimental data. The curve on the left is distorted due to noise, while the curve on the right has the noise filtered out. While constructing the cubical complex, the influence of noise is dominant where it biases the data in the vicinity of the threshold.

reduce it to a binary representation. The influence of noise occurs in regions where its amplitude is large enough to change the value of the measurement across this threshold. In many experiments, probability distributions of the amplitude, spatial and temporal variation of noise are well characterized. For example, while intensity measurements within pixels of a CCD array is well characterized by a Poissonian distribution. The change in the Betti numbers may be inferred from the probability distribution of noise in the individual pixels.

CHAPTER VI

HOMOLOGICAL CHARACTERIZATION OF SDC

6.1 Introduction and outline

In the previous chapter we discuss computational homology as a characterization and quantitative measure of geometric structures. In many spatially extended systems, the topology of these structures may relate directly to physical properties of the system. For instance, in a granular material, the structure of the force chain networks is seen to vary with a change in the load supported by it [27]. Building the relation of a physical characteristic to the geometry of the structure at a global scale depends on the particular system under consideration. The patterns exhibited across different systems are diverse and may relate to the particular mechanisms resulting the formation of the geometry.

In many systems, in addition to the complex geometry, there is a temporal evolution of the patterns exhibited as well. This is especially true for spatially extended non-equilibrium systems. The dynamical evolution in these system is often marked by the formation of structures that show complex evolving topologies. The spatial distribution of electrical activity during fibrillation in the heart tissue [61], or the organization of bacterial colonies in response to a environmental disturbances form examples of such systems [63]. Quantitative measures of the topology of the geometric structures displayed by these systems may be used in understanding the underlying dynamics.

In this chapter we emphasize the role of computational homology in connecting the topological evolution of patterns to the physical properties the system, and describe its use as a tool in the study of dynamical systems. The procedure to reduce measurements of geometries to the Betti numbers is robust, however, their interpretation to extract physical insights may benefit through comparison with other measures.

The homological characterization in this chapter is developed to describe fluid flows in experiments on RBC. The convective rolls in RBC arrange themselves in varying degrees of

61

complexity in response to the heat flux through the cell as well as the geometric constraints imposed through boundary conditions. At low ϵ, the rolls form stationary structures and at higher driving they show complex spatial and temporal dependence as described in Chapter 2. There have been many characterizations of the roll structures based on local measures of the wavelength, curvature and defect statistics. The local dynamics of these rolls are well described by the techniques discussed in these studies. These characterizations rely on the existence of a simpler structure in a smaller region of interest. For instance, identifying a defect intrinsically assumes a break in symmetry from a base state of locally parallel rolls [43]. The local wavenumber characterization relies on a sinusoidal intensity profile locally [22], and the curvature measurement approximates segments of the roll structures to circles [36].

At a global scale the patterns of the rolls in SDC have few symmetries that may be exploited to develop a similar characterization. In addition, the local characterizations do not reduce the dimension of the embedding space of the dynamics - they only map the local variations of the structure to different metrics. In contrast, the homological characterization of the rolls reduces the patterns to a set of scalars (the Betti numbers) that are independent of system size. The total number of Betti numbers is the dimensionality of physical space in which the pattern is embedded.

Some of the primary results gained through the homological characterization of SDC include (a) revealing a break in the symmetry of geometric configurations taken between hot and cold flows of the pattern, which may be attributed to non-Boussinesq properties of the fluid, (b) indications of bifurcations occurring through the onset of SDC, (c) characterizing the boundary influence through the pinning of the rolls to it, rather than the distance from the boundary, and (d) the evolution of the patterns exhibited to fluctuate stochastically rather than chaotically at the global scale.

6.2 Binary representation of the cubical complex

In our experiments shadowgraph images provide reliable data on the configuration of the convective rolls. The shadowgraph images distinguish between regions of heavier downflows

and lighter upflows flows through a density dependent variation in the refractive index across the fluid layer. Two dimensional intensity images form the experimental measurement of the state of fluid flow. High-frequency camera noise and optical non-uniformities are the primary sources of distortion in the data. The influence of these distortions are sufficiently minimized through Fourier filtering and subtracting a image of the cell prior to the onset of convection as described in Section 3.5. The images of the system are taken at about 10Hz yielding a measurement of the flow a few times every vertical thermal diffusion time at onset($\tau_\nu \approx 2$ seconds). A time series of 18000 images is captured over a range of ϵ stepped from 0.125 to 4.125 in increments of 0.125.

Figure 33: The intensity profile representing the state of the fluid flow as captured in the experiment at $\epsilon \approx 1$. The image is Fourier filtered to remove high frequency spatial noise. The cubical complex is constructed separately for hot flows (dark) and cold flows(bright) representing two components of the geometry. We refer to the cubical complex representing these flows as X^{hot} and X^{cold}. The geometric structure of hot and cold flows are measured to be distinct in their homological properties. The choice of thresholding at the mean value of the intensity profile distinguishes hot and cold flows to distinct equal areas of the convection cell.

Prior to developing the homological characterization of the patterns exhibited by SDC, the filtered images are reduced to a binary representation/cubical complex. The intensity profile of the flow is thresholded at the median value, with regions above and below the threshold representing hot and cold flows. This choice of the binary representation segregates regions of hot flows and cold flows to constitute equal areas of the convection cell.

As seen in Figure 33, the regions of hot flows and cold flows represent different patterns

that may be characterized through computational homology. The time series of images is converted to cubical complexes as described above and the computational homology algorithms are used to extract the Betti numbers from each image [37, 38] at different values of ϵ. This results in a pair of Betti numbers for hot flows $(\beta_0^{hot}(n,\epsilon),\ \beta_1^{hot}(n,\epsilon))$ and cold flows $(\beta_0^{cold}(n,\epsilon),\ \beta_1^{cold}(n,\epsilon))$, for the nth image of the time series. The complete state of the flow as described by the homological characterization of the two dimensional shadowgraph images is provided by the vector $(\beta_0^{hot}(n,\epsilon),\ \beta_1^{hot}(n,\epsilon),\beta_0^{cold}(n,\epsilon),\beta_1^{cold}(n,\epsilon))$. The values $\beta_0^{hot/cold}$ represent the number of distinct hot/cold convective rolls(or distinct components) visualized in the flow. Similarly, $\beta_1^{hot/cold}$ counts the total number of loops formed by the hot/cold convective rolls as illustrated in Figure 34
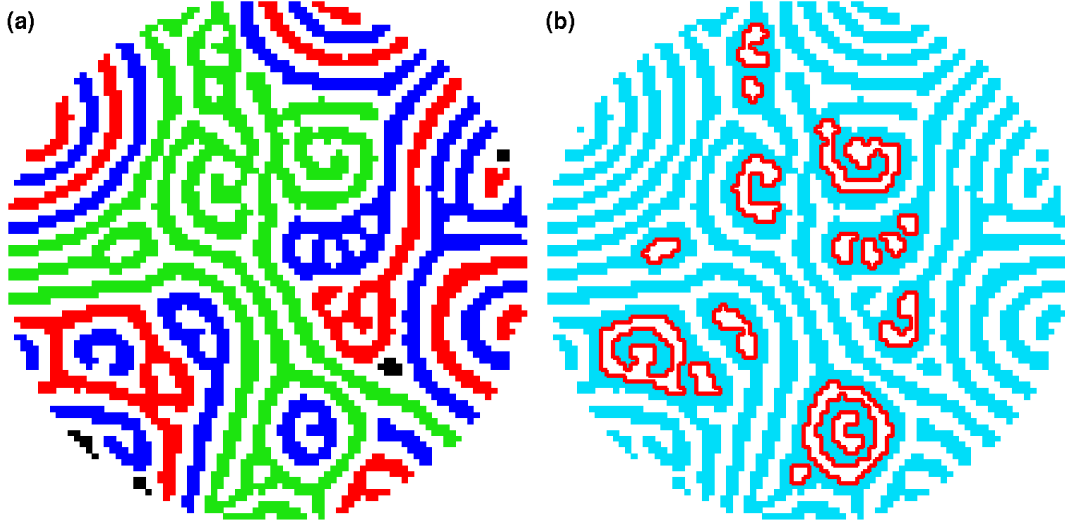
Figure 34: The geometries above are representative of those found in SDC and illustrate the physical interpretation of the Betti numbers extracted through computational homology. In (a) neighboring components comprising the geometry are indicated in different colors. There are 34 such distinct components in all - this number is the zeroth Betti number, β_0. These components sometimes self-intersect to form loops sectioning off parts of the space the geometry is embedded in. These holes, or voids, in the structure are indicated with a red boundary in (b). The number of these holes (13 in the figure above) is the first Betti number, β_1.

The measurement of the convective flow through shadowgraphy and its subsequent reduction to a binary image is done by fixing some parameters determined by physical considerations. These parameters correspond to the frame rate for image capture, the length of time the images are captured, the spatial resolution at which the images are captured

and the threshold used in building the cubical complexes.

The fastest time scale in the dynamics is expected to be the vertical thermal diffusion time, $\tau_\nu \approx 2$ seconds. This time scale is also visually seen to correspond to the time taken for local defect nucleation. We capture images at about 10Hz, which would be sufficient to resolve variation in topology caused through these events. Sampling the Betti number time series at lower rates(such as using every other data point, corresponding to halving the frame rate) is seen not to change the results of our analysis described below. In addition, sampling only the first half of our time series does not change the qualitative results seen either. This indicates that the frame rate and the length of the image capture we use is sufficient to describe the dynamics through a homological characterization.

The homological characterization through the Betti numbers represents a measurement that is scale independent, however it does require measurements of the structure at a resolution that is representative of the geometry of the system. The roll wavelengths form the smallest length scale that may be used to define the pattern. The CCD array captures shadowgraph images that resolves the flow to about 20 pixels across each convective roll. Spatially binning the images thus captured to reduce the resolution by up to a third is seen to make insignificant variations in the measurements of the Betti number time series for our purposes.

The reduction of the shadowgraph images to the binary complex distinguishes regions corresponding to hot upflows and cooler downflows. The threshold at which these two distict regions are segregated is an important parameter determining the subsequent geometric structures formed in the binary representation. The geometry of the flow can vary significantly as the smooth intensity variation is reduced to a binary representation as seen in Figure 35. The upper two images in Figure 35, the threshold has been varied to have have $\beta_0^{hot} = \beta_0^{cold} = 33$ and $\beta_1^{hot} = 3$, $\beta_1^{cold} = 5$. As seen in the figure, a large variation in the threshold can lead to the cubical complex being an unrealistic representing the structure of the flow seen in the shadowgraph images. Convective rolls that are seen to be connected may be broken into distinct pieces at regions where the intensity is just beyond the threshold value. While one may vary the threshold to require a symmetry in a pair of Betti numbers,
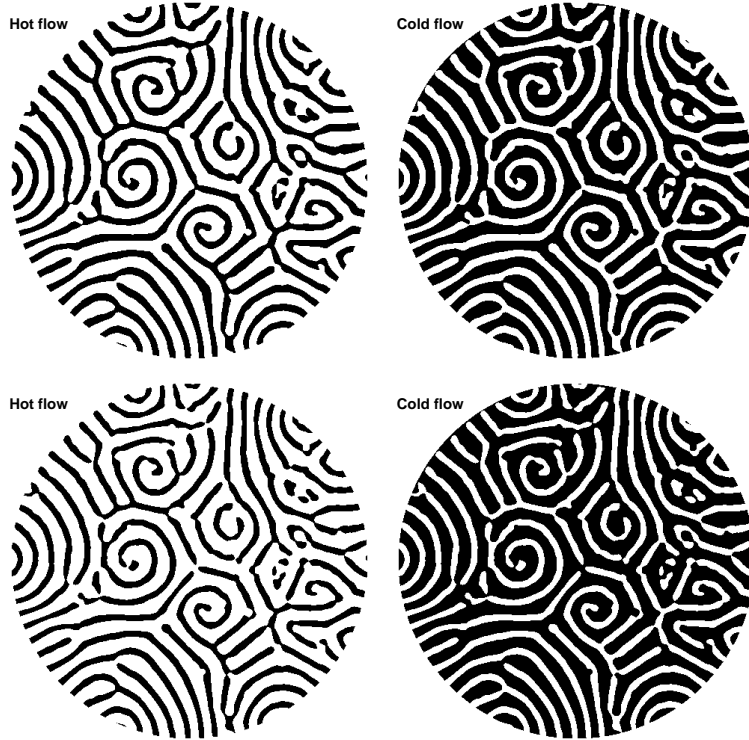
Figure 35: The upper two images are binary complexes built with varying the threshold from the median value by 14.6% of the peak to peak intensity seen in Figure 33, which corresponds to an equal number of distinct components for hot and cold flows. The lower two images illustrate the geometry extracted when the threshold is varied by 20%. The images are for a state exhibited at $\epsilon = 1$. The geometry of the roll structure is degraded when compared with the intensity image seen in Figure 33, as the threshold value is increased away from the median value.

this symmetry may not be satisfied for the other Betti numbers. Further variation of the threshold increasingly changes the asymmetry in the geometry of the rolls. The reasoning behind separating the flows into regions covering equal areas is presumes that the fluid is Boussinesq, incompressible, with a conserved volume. The areas representing upflows therefore may intuitively equal the areas of downflows over the entire convection cell. It is worth noting that in our experiments, the regions in the images that are close to the threshold are sparsely distributed. The events leading to their crossing their threshold are typically associated with large variations in intensity. A small variation in the threshold, while changing the Betti numbers for a particular image, therefore does not significantly change the statistical properties of the Betti number time series.
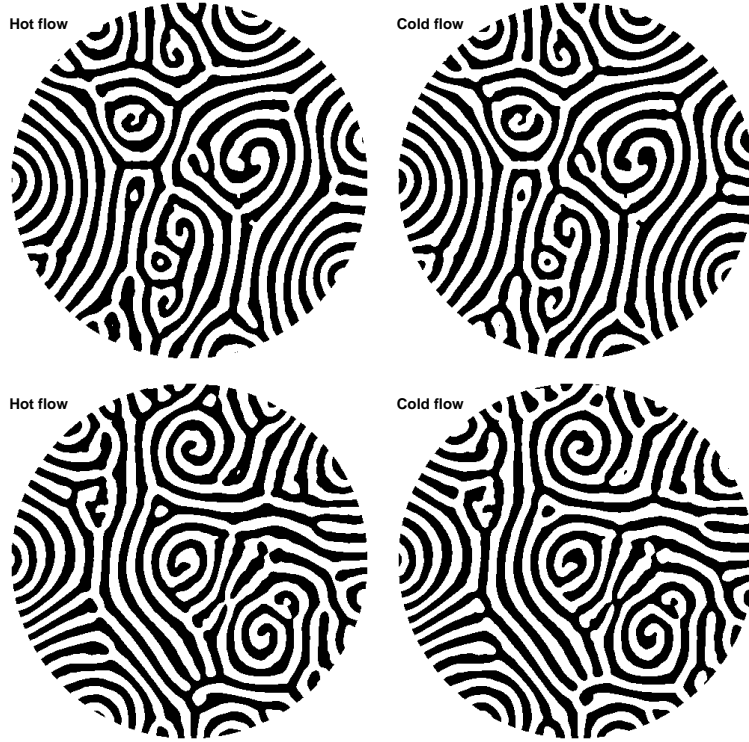
Figure 36: The above set of images indicate states of the flow at two instants of time, characterized by the same Betti numbers. In the two upper images, the hot flows and cold flows correspond to the binary images used, with $\beta_0^{hot} = 42$, $\beta_0^{cold} = 32$, $\beta_1^{hot} = 2$, and $\beta_1^{cold} = 10$. The same Betti numbers characterize the state of the flow in the lower pair of images, taken at the same value of $\epsilon = 1$. The geometry of the flow is clearly seen to be different, although the Betti numbers do not distinguish between them.

In the following sections we discuss the primary results and questions raised by analyzing the time series of Betti numbers. While the Betti numbers do not uniquely describe the pattern of convective flow(Figure 36), we shall nevertheless use them to identify the homological state of the system. The geometry of the flow may be substantially different in two images that are reduced to the same set of Betti numbers. In two dimensions, these images may be transformed into each other by a spatial rearrangement of the rolls along with continuous deformations in their scale. Tracking the system through the Betti numbers does not allow for uniquely reconstructing the flow, although it constrains the set of geometric configurations taken by the convective rolls.

The basic roll like structure of the flow may add further constraints on the Betti numbers of hot and cold flows. In simple symmetric geometries such as parallel roll patterns, this

relation is $\beta_0^{hot} = \beta_0^{cold}$ with $\beta_1^{hot} = \beta_1^{cold} = 0$. Similarly, in a target pattern with n hot and n cold rolls, we would have $\beta_0^{hot} = \beta_0^{cold} = n$ and $\beta_1^{hot} = n$ and $\beta_1^{cold} = n - 1$, where we have presumed the central spot of the target pattern to be cold. For more complex geometries and time dependent patterns, these relationships are not easy to determine.

In the remainder of the chapter, the "state" of the system shall refer to the description of the homological characterization of the pattern through the Betti numbers. Two patterns with the same set of Betti numbers will be considered as representing the same state.

6.3 Results

The Betti number time series track the geometric configuration taken by the hot and cold regions of the fluid. While the total area of the hot and cold regions in the binary representation are conserved (equaling half the area of the convective cell), the Betti numbers detail finer structures of the flow. The time series of the Betti numbers over different values of ϵ describe the response of the flow pattern to different levels of driving. In this section we describe some measures extracted from the time series of Betti numbers and propose interpretations consistent with the patterns seen in RBC and SDC in particular.

Time series:

In Figure 37 a sample of the time series of the Betti numbers is displayed. Each of the Betti number time series fluctuates within well defined bounds. The fluctuations in the Betti numbers represent the variation in the topology of the convective rolls. The different Betti numbers at a given value of ϵ are seen to fluctuate about different mean values.

At low ϵ the convective rolls are seen to be primarily stationary and parallel, with a few defects in the structure occurring close to the boundaries. In such symmetric structures the number of hot and cold rolls are equal. As ϵ is increased the flow pattern becomes increasingly complex with defects permeating across the bulk of the system. The defect nucleations are local coherent structures that result from the interaction of neighboring convective rolls as described in chapter 4.

The bounds of the Betti number time series indicate that these configurations are confined to particular geometries at each value of ϵ. The time series provide an indicator of
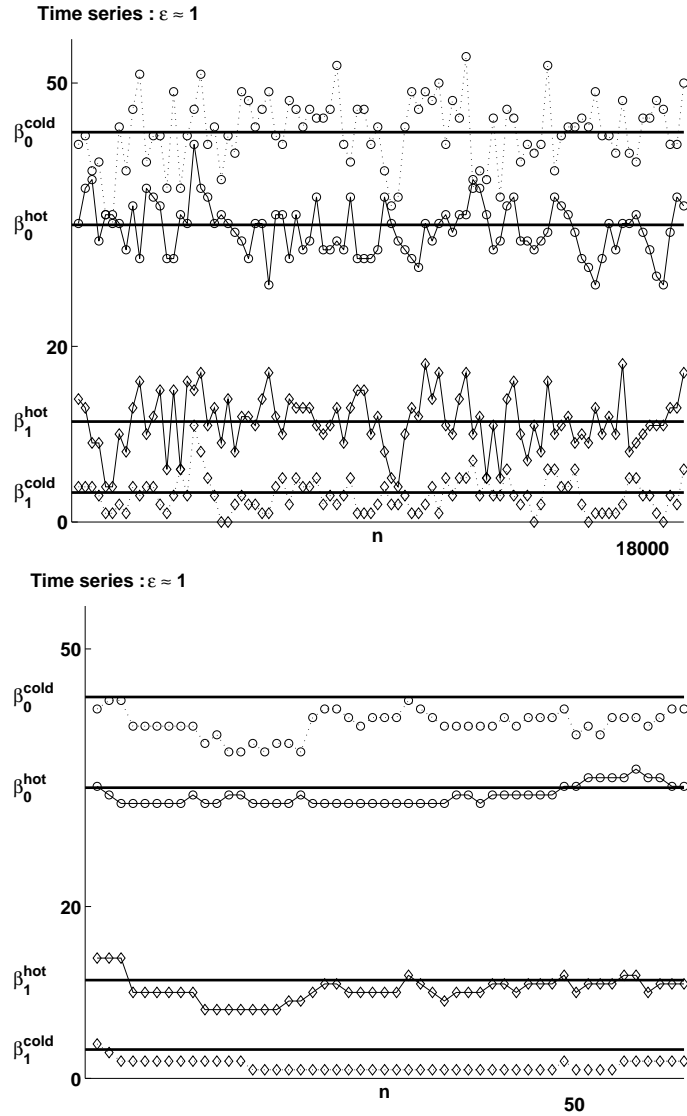
Figure 37: The Betti numbers for a time series of images representing the flow in SDC fluctuate to reflect the variation in the topological configuration taken by the system in. The time series in the upper image indicates every 200th data point in the time series of 18000 for better visualization. The bounds on the Betti numbers represent the limited geometric configurations spanned by the dynamics. The dotted lines connect Betti numbers for cold flows and solid lines hot flows. Circles and diamonds mark the zeroth and first Betti numbers. The lower time series plot illustrates the fluctuations when every data point is considered. The solid horizontal lines indicate the mean values of the Betti numbers computed over the entire time series.

convergence to an attractor - the transient dynamics is known to have died out as the mean values and fluctuations about it converge. The fluctuation in the Betti number time series reflect the variation in topology arising from the formation of defects. As an example, in a

69

complex pattern with a single defect formation two neighboring rolls may merge reducing the number of distinct components, β_0, by one. Defects in SDC are extensive through the entire convective domain, and multiple and simultaneous occurrence of defects result in the Betti number to fluctuating rapidly, much faster than the vertical thermal diffusion time, τ_ν.

The Betti numbers measure only the global changes in the roll configurations, while defect nucleations are local events. The Betti number time series would have to be combined with measures of defect statistics [43] to quantify the relationship between them.

The Betti numbers offer a mechanism to track the dynamical evolution of the pattern with a few indicative scalars. The statistical description of these time series as a function of ϵ indicate the different attractors converged to as the driving in the system is increased.

Mean values

The mean values of the Betti number time series are as a function of ϵ are displayed in Figure 38. The mean value is computed by averaging the Betti number over the time series, $\bar{\beta}(\epsilon) = \sum_{n=1}^{N} \beta(n, \epsilon)/N$, where N is the length of the time series. The mean values of the time series are seen to have converged, showing little variation when computed over half the length of the time series.

One distinctive feature of the plot is that the mean number of distinct components and distinct holes in the geometries of hot and cold regions are similar at low ϵ (i.e. $\beta_{0,1}^{hot} \approx \beta_{0,1}^{cold}$). This symmetry between hot and cold regions is broken as ϵ is increased. As a gross measure, the mean number of distinct cold regions increases while those of hot regions decreases with an increase in ϵ. The mean number of holes in the geometry exhibited by cold flows is seen to increase, but not as rapidly than that of hot regions with an increase in ϵ. In addition, there are seen to be no holes in the structures found in the geometry of convective rolls at low ϵ.

The exact values of the Betti numbers depend on the threshold used in constructing the binary representation. The qualitative features of the mean values as seen in Figure 38 remain unchanged with a variation in the threshold value by 10% of the peak to peak

Statistics
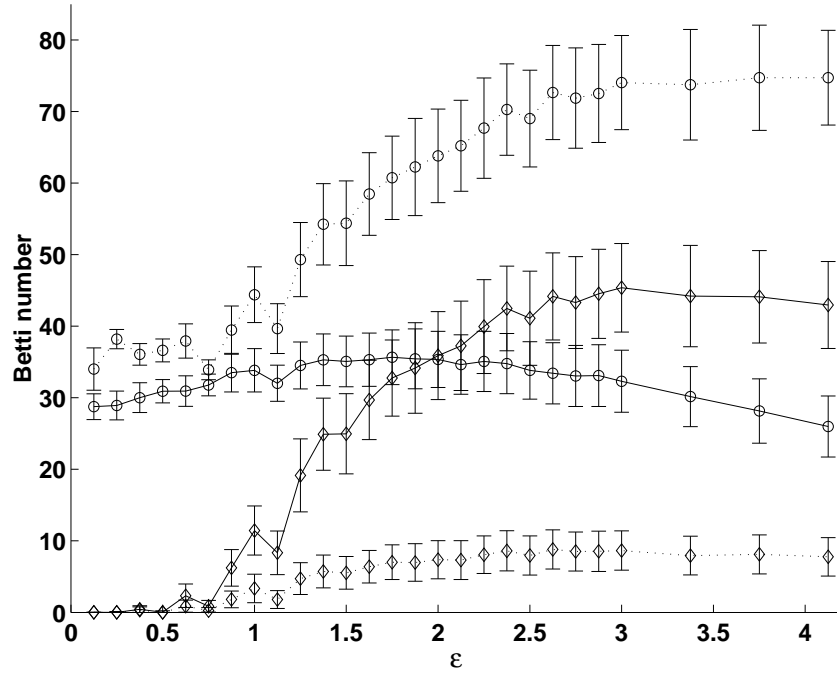
Figure 38: The variation of mean values of the Betti number time series (as indicated in the figure on the left) with ϵ is displayed. The error bars indicate the standard deviation of the time series. The asymmetry between the configurations spanned by hot upflows and cooler downflows is noteworthy; this asymmetry increases with higher driving. The dotted lines connect Betti numbers for cold flows and solid lines hot flows. Circles and diamonds mark the zeroth and first Betti numbers.

intensity in the shadowgraph images. The threshold value was set at the median intensity of the shadowgraph images to distinguish bright and dark regions into equal areas.

The change in the Betti numbers by a variation in the threshold value would occur in regions where the intensity of the shadowgraph image is close to the threshold value. Such regions often occur when the convective rolls are close together. The reduction in the threshold about regions of high wavenumber would tend towards merging neighboring rolls, while increasing the threshold would tend to distinguish rolls that are close together. Regions that correspond to such events are seen to be distant from each other in the flow, and occur for short periods of time. The sparse nature of these events in the dynamics therefore may not contribute significantly to changing the mean values of the Betti number time series. The reduction in the threshold value would thus foreshadow the merging of neighboring rolls through an increase in regions of high local wavenumber, and increasing

the threshold does the reverse.

The absence of tunnels at low ϵ is consistent with the occurrence of straight roll structures seen in the convective flow. The transition SDC is coincident with the formation of loops in the convective roll patterns. The holes in the pattern occur when a single roll self-intersects. An increase in the density of defects in the convective flow may therefore lead to an increase in β_1. The variation in the mean values of the Betti numbers between hot and cold regions of the flow might be related to differing mechanisms of defect occurrences in these distinct regions.

The defects in SDC occur in regions of local compression or dilatation of the roll structure. The compression leads to the merging of neighboring rolls while the dilatation results in the formation of a new roll in the pattern. Such local events change the topology of the pattern. For instance, the merging of two rolls reduces the number of distinct rolls reducing β_0 by one. A pattern increasingly dominated by such instabilities would hence show an overall reduction in β_0 as different components link together locally at distinct locations. As the number of distinct rolls reduces, such linkages are often self-intersections of a roll. This manifests as an increase in the number of loops (β_1) in the pattern. The mechanisms characterizing the secondary instabilities for ideal straight rolls [6, 7] have a similar structure and are known as the skew-varicose (compression) and the cross-roll (dilatation) instabilities. In spiral defect chaos such events are seen to be operational in regions localized by the curvature of the rolls. The lower mean values for the number of components seen in hot flows as opposed to cold flows, $\bar{\beta}_0^{hot} < \bar{\beta}_0^{cold}$, indicates that hot flows are more dominated by analogues of skew-varicose type instabilities than cold flows. The mean values of the Betti numbers (Figure 38) thus reflect the instability mechanisms operating during the evolution of the complex spatiotemporal pattern in SDC.

The asymmetry in the patterns seen through the Betti numbers may be related to biases between hot and cold regions of the flow in the shadowgraph technique, boundary conditions of the fluid and/or physical characteristics of the fluid itself. The shadowgraph technique provides a qualitative distinction between hot and cold regions of the flow, and relating it quantitatively to the velocity of the fluid flow is not easily done. For our purposes,

the choice of the threshold assures us of a symmetric construction of the cubical complex, with hot and cold regions represented by equal areas of the convective flow. The boundary conditions of the fluid are known to be asymmetric - the thermal conductivities of the top sapphire window and metallic mirror vertically bounding the fluid layer are different. The thermal conductivities of these bounding plates are much higher than that of the CO_2 gas, and the influence of this variation is presumed to be minimal on the flow. We believe the primary mechanism for the asymmetries noticed may result from a variation in the physical properties of the fluid itself.

The flow in ideal Rayleigh-Bénard convection, as described by the Boussinesq equations [29], has a reflection symmetry about the horizontal midplane between the two confining horizontal plates. This symmetry of the flow (the Boussinesq symmetry) in an ideal Rayleigh-Bénard problem suggests that the statistical properties of the patterns would be the same for cubical complexes built from hot or cold flows; in particular we should obtain $\bar{\beta}_i^{hot}(\epsilon) = \bar{\beta}_i^{cold}(\epsilon)$ for $i = 0, 1$ at all values of ϵ. As Figure 38 indicates, in our experiments we find that the mean values of the Betti numbers clearly distinguish between fluid regions comprised of hot and cold flows. Furthermore, this asymmetry is enhanced with an increase in the Rayleigh number. We suspect that the pattern homology serves as a detector of non-Boussinesq effects that are present due to the variation in physical properties of the fluid between the hot bottom layer and the cool top layer. The strength of non-Boussinesq effects in experiments can be estimated by a dimensionless parameter Q [7, 16] computed perturbatively at the primary instability for convection as described in Chapter 2. In our experiments with CO_2, we find this parameter to equal 0.54 near the onset of convection — thus indicating strong, O(1), non-Boussinesq effects. Higher temperature differences between the plates bounding the fluid flow would further strengthen the non-Boussinesq influences.

While the non-Boussinesq effects break the symmetries between hot flows and cold flows, it is not clear as to how this leads to the variation in the patterns exhibited by hot and cold flows. In large aspect ratio cells, transitions between hexagonal structures and roll structures have been attributed to non-Boussinesq properties of the fluid [5]. While this

provides for some qualitative indication of the patterns selected by breaking the Boussinesq approximation, we do not have specific answers as to why the number of hot rolls is lower than the number of cold rolls in SDC. The larger number of holes in hot flows indicates that cold regions are often enveloped by cooler regions, but not the other way around. At low ϵ, the symmetry of the pattern resulting in parallel roll structures results in a symmetry in the Betti numbers between hot and cold flows in spite of the fluid being non-Boussinesq. In the flow exhibitted by numerical simulations of convective flow by Janet Scheel and Michael Cross at Caltech, the Boussinesq approximation is built into the equations of motion. Computing the Betti numbers of the patterns exhibitted by the mid-plane temperature profile of the cell shows a symmetry between hot and cold flows.

At large values of ϵ, the mean values of the Betti numbers are seen to approach asymptotic values. These values, and the progression towards them may be influenced by the system size. At a finite system size, the number of possible configurations the rolls can take may be bounded - further configurations may be possible only at levels of driving that break the basic roll structure seen from the onset of the primary convective instability. The existence of an asymptotic value for the Betti numbers also indicates a qualitative change in the dynamical evolution of the system at large ϵ, with the driving through heat flux not causing substantial variation in the homology of hot and cold flows. It could be that higher driving only increases the rate of the fluctuation between the different geometric configuration the flow exhibits.

Number of states

The convection rolls take on different configurations at different values of ϵ. As ϵ is increased, the number of configurations spanned by the rolls increases, as measured by the vector $(\beta_0^{hot}(n,\epsilon),\ \beta_1^{hot}(n,\epsilon),\beta_0^{cold}(n,\epsilon),\beta_1^{cold}(n,\epsilon))$. The number of states attained by the system shows distinct steps as a function of ϵ. The size of the plateaus is seen to increase with the number of states spanned as well as ϵ. The state of the system was captured by an 18000 image long sequence, sampled at equal time intervals. This bounds the maximum number of configurations we would be able to measure for the system. At higher driving, the

number of states attained approaches this bound, indicating that the system is increasingly able to span more distinct states. Sampling the time series with half the images reproduces similar qualitative features as seen in Figure 40. These qualitative features are preserved when the samples are chosen either from a smaller section of the time series corresponding to half the data, or considering every other data point from the Betti number time series.

One reason for the increased span of states with increasing ϵ may be the faster dynamics at higher ϵ which effectively samples a larger number of states in the time taken to captures images. However, the qualitatively similar appearance of the increase in the number of states in spite of the reduced sampling the time series discounts this possibility. The number of states spanned at lower ϵ does not change as dramatically as those at higher values of ϵ.

We speculate that a higher heat flux through the fluid provides energy for the system to span a more diverse set of geometric configurations. This would increase the number of states attained at larger values of ϵ. The transition between the plateaus seen in the number of states as ϵ is increased may be indicative of bifurcations occurring within the system. This is akin to the number of states spanned by the system as it undergoes period doubling bifurcations. At the points of bifurcation system parameter doubles the number of stable states, with the previously stable states turning unstable. The number of stable states therefore shows increases in steps, each step indicating the doubling in the number of states. The size of these steps in the standard period doubling route is however seen to decrease towards the onset of chaos, unlike the increase we note in the onset of SDC. In the bifurcations we suggest in RBC, as the parameter of the system ϵ is incrementally changed, the system accesses a different number of states in a discontinuous manner. While the number of states in the plateaus is similar, the states themselves are qualitatively different as is indicated by the mean values of the Betti numbers in Figure 38. The fluctuation about these mean values however are similar. A study involving a finer resolution in the variation of ϵ would shed more light on the nature of the bifurcations indicated.

The structure of the rolls are seen to take on more intricate patterns at higher ϵ. The fluctuation amongst the different states accessed would be indicative of the stability of the structures formed in SDC. The system at parameter values with fewer fluctuations may be
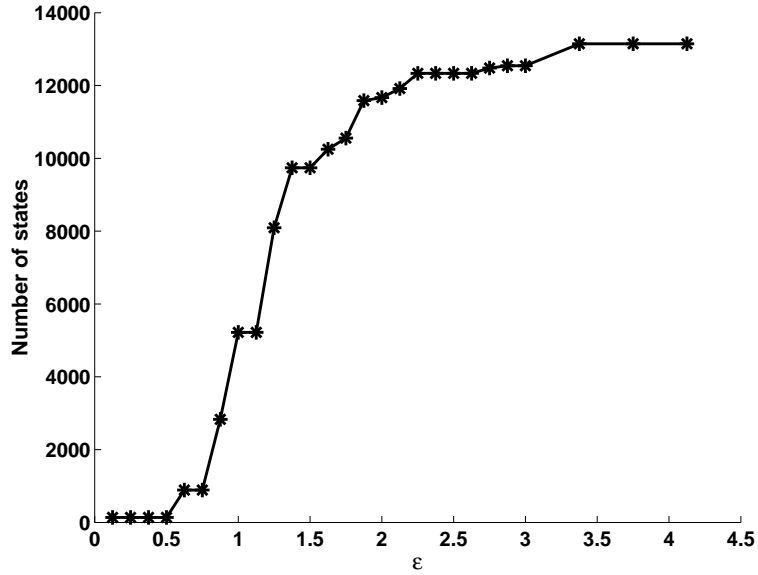
Figure 39: The number of configurations spanned for the period of measurement as a function of ϵ is indicated above. The plateaus in the plot are indicative of bifurcations occurring in the system as the driving is increased.
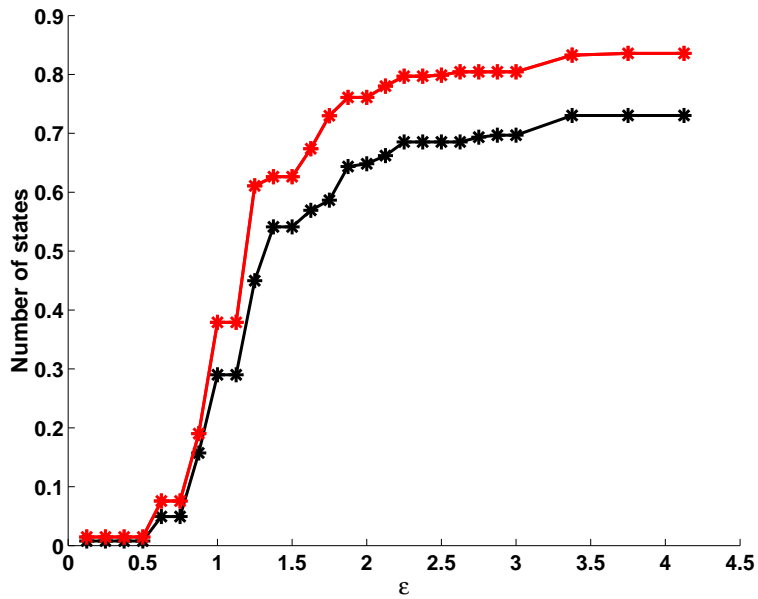
Figure 40: The number of configurations spanned, normalized with the total number of measurements taken is indicated in the above figure. The black curve is a the states spanned over the entire(18000) image time series, while the red one is from the first half(9000) of the time series.

infered to have fewer instability mechanisms operating.

While a number of states are spanned at a given value of ϵ, not all the states are accessed with equal frequency. The time series of Betti numbers allows one to empirically compute the probability of occurrence of a state defined by $(\beta_0^{hot}(\epsilon),\ \beta_1^{hot}(\epsilon), \beta_0^{cold}(\epsilon), \beta_1^{cold}(\epsilon))$. The probability is obtained by trivially counting the number of distinct configurations attained over a large (ergodic) period of time and normalizing by the total number of possible configurations. The probability distribution, p, enables the computation of an entropy to distinguish between different SDC attractors. The entropy is defined as

$$S(\epsilon) = -\sum_i p_i log(p_i),$$

where the index i span the different states attained by the system as characterized by the Betti numbers.

The entropy of the system increases with increasing ϵ. The increase is however non-monotonic. In Figure 41, dips in the value of entropy are observed even with an increase in ϵ. The values at which the dips in entropy occur are seen to correspond to regions of transitions in the plateaus described in Figure 39. The dips are however not easily identified at larger values of ϵ. The entropy characterizes the fluctuations in the number of states observed. If these fluctuations spanned the total number of accessed states, N with equal frequency, the entropy would vary as $log(N)$. Normalizing the value of entropy by $log(N)$ indicates that at higher ϵ, the states asymptotically span states with equal probabilities of occurrence as ϵ is increased. This normalization is also seen to increase the size of the dips in the non-monotonic regions.

The broad increase in entropy with ϵ is consistent with the larger number of states being spanned by the system. The larger number of states spanned indicates a larger size of the attractor, and the entropy change would be extensive with the size of the attractor in phase space.

The non-monotonic behavior, with increasing the driving reducing the entropy may indicate that the rolls get more ordered within the convection cell when ϵ is increased. As

the number of rolls (or other Betti numbers) in the system changes, the geometry of the rolls may be more commensurate with the boundary geometry. Variations in roll curvature, wavenumber or other factors may influence the rolls to 'fit' better within the bounds of the convection cell as well. A signature this proposed mechanism is seen in the sample of images shown in Figure 43. The images indicated in the figure are chosen across the different values of ϵ. The structure of the pattern is seen to have a qualitative change from being more convoluted to mostly parallel rolls at values of ϵ corresponding to the dips in the variation of entropy (see images corresponding to $\epsilon = 1$ and $\epsilon = 1.125$ for example). While the geometric signatures of bifurcations are dramatic at lower values of ϵ, it is harder to visually notice them in the more complex evolution at higher ϵ.
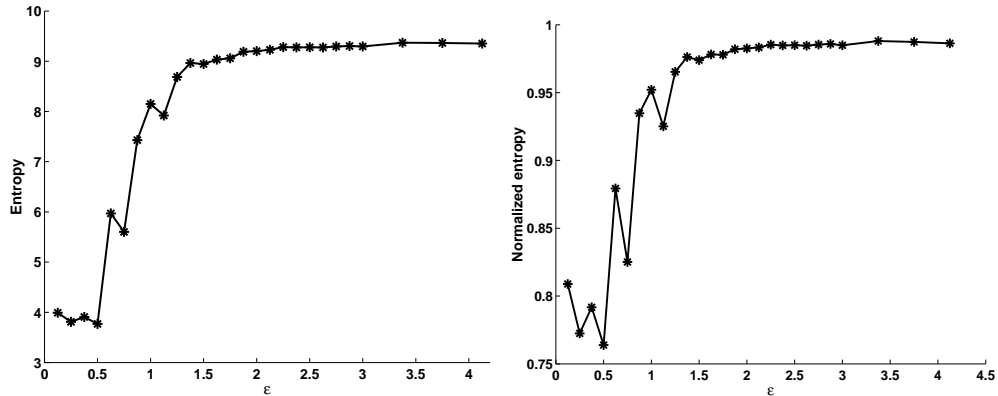
Figure 41: The entropy of the attractor indicates behavior akin to a phase transition as a function of ϵ. The entropy computed from the time series is shown in the upper plot. When normalized against the entropy of white noise (right), the plot asymptotes close to one at higher values of epsilon.

The reduction in entropy with an increase in ϵ is consistent with bifurcations occurring within the system, although it may not be as sensitive an indicator as the number of states spanned at higher ϵ. The entropy however may provide more details on the nature of states selected as bifurcations occur.

With the proposed mechanism, further insights into the bifurcations may be gained by varying the aspect ratio of the system. The values of ϵ at which the peaks and dips occur would be expected to shift (and perhaps even oscillate) as the aspect ratio varies in units of the roll width for example. The separation between the parameter values at bifurcations

would be expected to reduce with an increasing aspect ratio, smoothening out at very large aspect ratios (as compared with the roll width, or average hole size for instance). When the system size is large compared to the intrinsic length scales, variations in the system size may be accommodated by small changes in the intrinsic length scales.
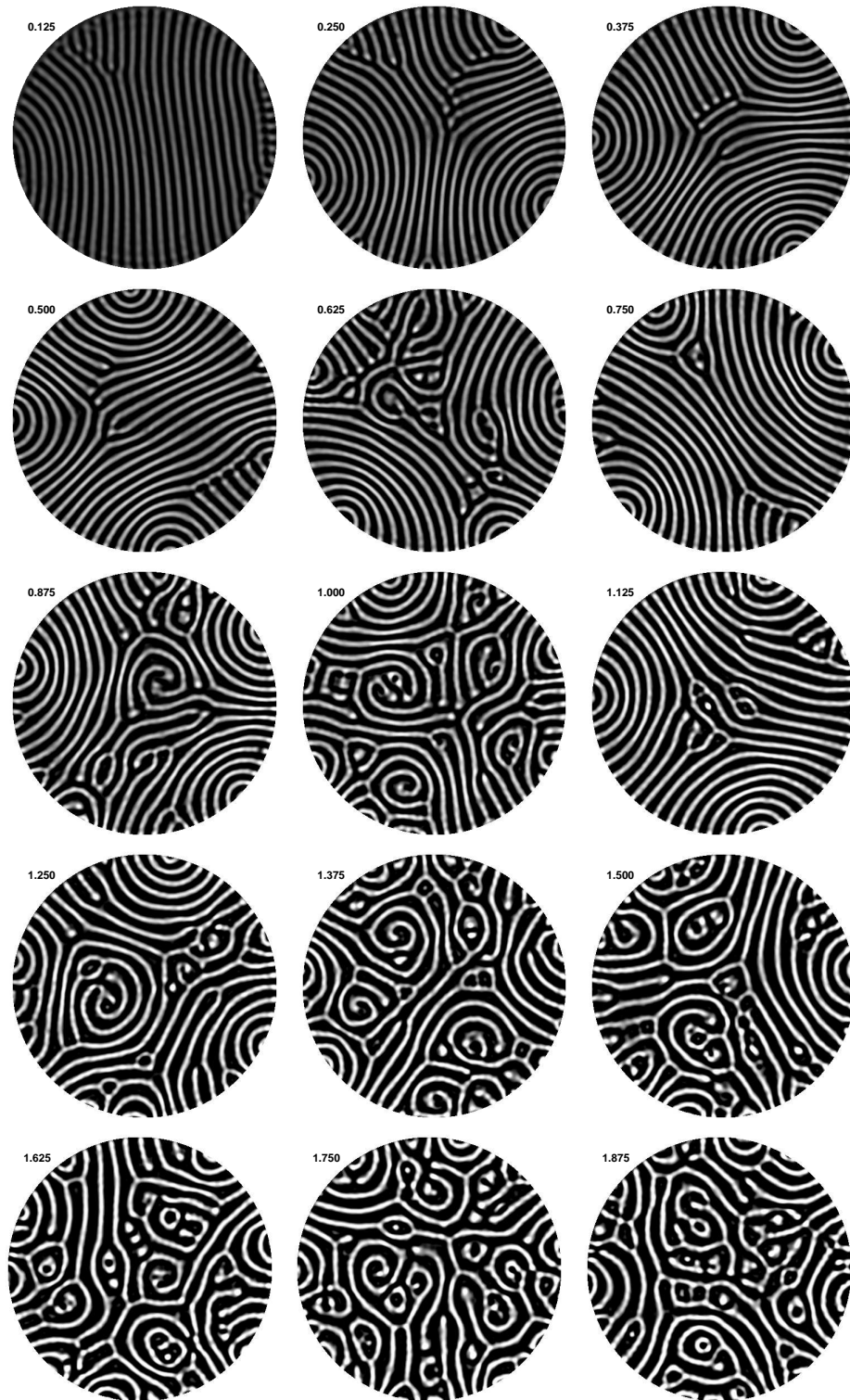
Figure 42: – continued on next figure...
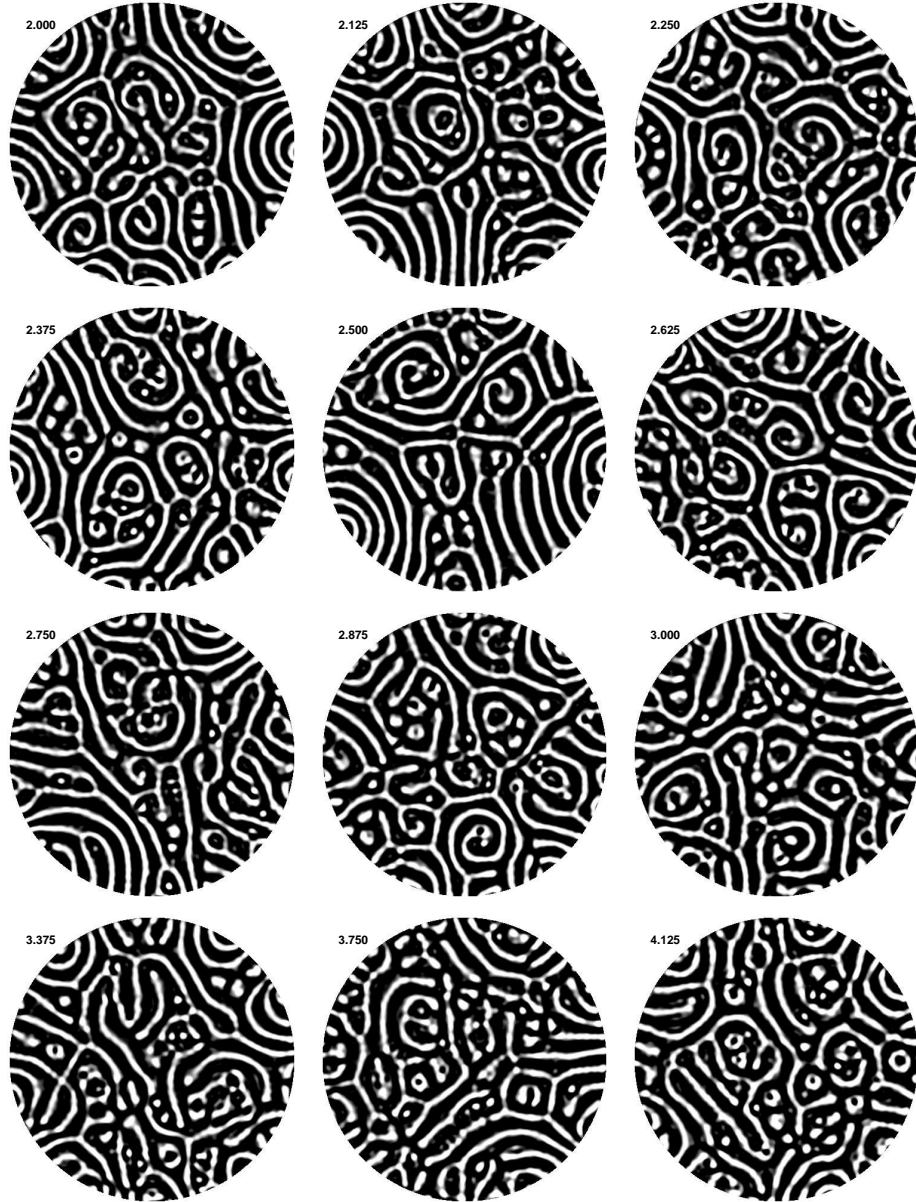
Figure 43: A sampling of the experimental measurements of the flow in our experiments on RBC measured at different ϵ (indicated on the top left side of each image). We quantitatively measure the qualitative differences in the geometry seen in the different images.

A similar entropic variation was described in studying the onset of SDC from straight rolls [9]. A spectral entropy was defined relating to the distribution of the Fourier spectrum of the state. In this study, no oscillatory behavior was noticed in the variation of the spectral entropy with ϵ. This might be due to the much larger aspect ratio used in this investigation.

The description of the flow through the Betti numbers allows for the separation of
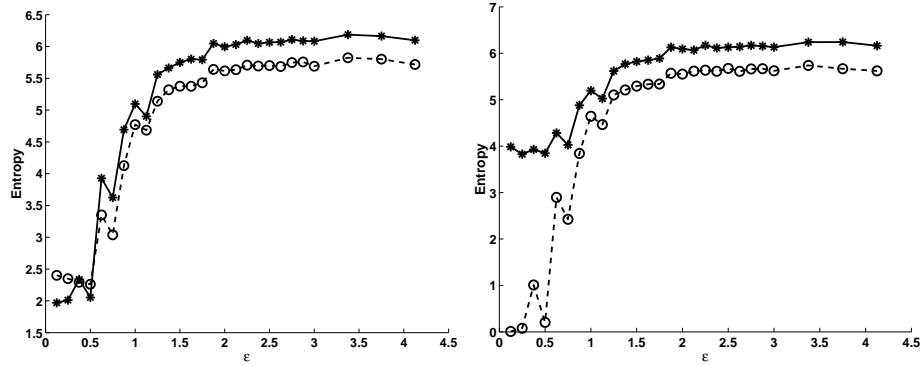
Figure 44: The image on the left plots the variation of entropy as distinguished between hot(stars) and cold(circles) regions. In the image on the right, the entropy contribution due to fluctuations in the number of components(stars) and holes(circles) is indicated.

the dynamics in a manner not possible through the spectral entropy. One may use the Betti numbers of only the hot flows or cold flows to compare the relative entropic variations occurring between them. Similarly, the fluctuations in the geometric configurations too may be separated, with the number of holes compared to the number of distinct components in the flow. Figure 44 indicates such comparison.
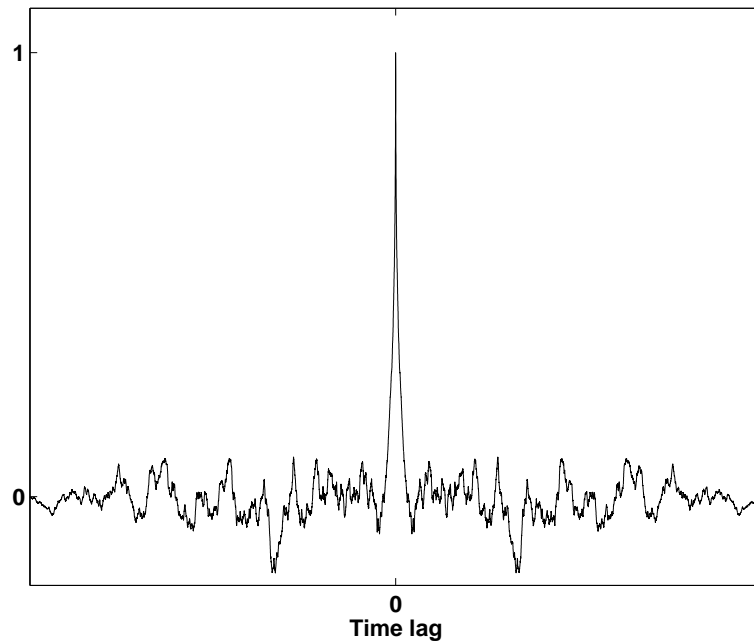
Figure 45: The autocorrelation of Betti number time series decorrelate rapidly. There are no significant coherent patterns discernable. This is the strongest indicator we have of the homological configurations evolving stochastically.

82

While the number of states and entropy measure the spatial structure of the states spanned by the system, they are not indicative of the temporal evolution of the pattern. The autocorrelation of the time series in the regime of SDC is seen to be sharply peaked at zero time. The correlation of the Betti numbers at later times are close to zero.

The evolution of complex geometries may be distinguished as being chaotic or stochastic from the time series of Betti numbers. The sequence of Betti numbers has been used previously to uncover global chaotic evolution through the computation of the largest Lyapunov exponent in numerical simulations of reaction-diffusion systems previously [24]. In our experiments on SDC we have been unsuccessful in extracting Lyapunov exponents using similar techniques. In the case of SDC a mechanism describing locally chaotic islands driving the complex dynamics has been proposed [22, 23]. It is likely that the spatiotemporally localized nature of such instabilities in SDC decorrelates at a scale that is not effectively captured by the time series of Betti numbers; a succession of these local events interspersed across the system may cause effectively stochastic evolution for the global geometric structure attained at the attractor. To first order we find it likely that the dynamics of fluctuations in the Betti numbers may be primarily stochastic in nature, as it is also suggested by the auto-correlation of the time series (Figure 45).

Boundary influence

The pattern homology can also provide a well-defined way to separate boundary-driven effects from bulk phenomena in pattern forming systems as indicated in Figure 46. Using homology, we distinguish regions of a pattern as being part of the bulk if they are isolated from the boundary i.e. distinct rolls that do not touch the boundaries. These bulk regions of a given component (say, for example, isolated hot regions) are easily counted by recognizing they comprise the interior of holes of the other component (in this example, cold holes, as characterized by β_1^{cold}). Thus, the number of components of X^{hot}(defined in Fig 33) connected to the boundary is $\beta_{bdy,0}^{hot} := \beta_0^{hot} - \beta_1^{cold}$. Similarly for X^{cold}, $\beta_{bdy,0}^{cold} := \beta_0^{cold} - \beta_1^{hot}$.

One notices an asymmetry between the two components in this measure (Figure 47) with a smaller number of components connected to the boundary as ϵ increases for hot
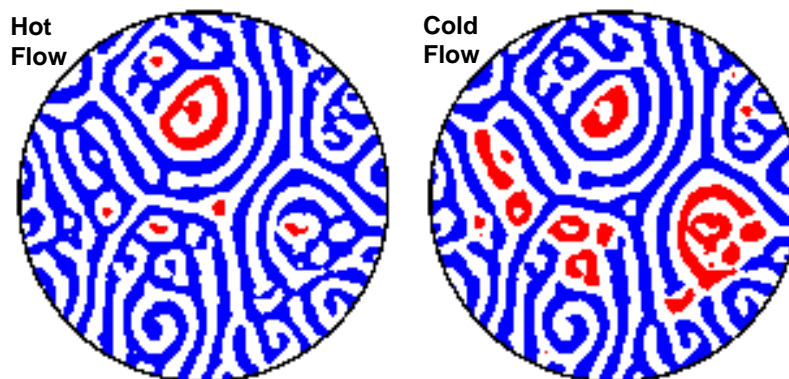
Figure 46: The above image illustrates the pinning at the boundaries for regions of hot flows(left) and cold flows(right). The rolls marked in blue touch the boundary, and those in red do not.

rolls as opposed to being almost the same for cold rolls. This also reflects in the number of components in the bulk, $\beta_0 - \beta_{bdy,0}$, where the ϵ dependence is primarily seen in the cold rolls.

Typically, separating boundary behaviors from bulk effects is done by setting a cutoff based on pattern correlation lengths. This technique may not suffice where pinning to the boundary may be the dominant boundary driven influence. This is especially true when the length scales of individual components may be of the order of the system size. In our system, we observe that rolls tend to align themselves perpendicular to the boundary. Influence of this orientation preference at the boundary may propagate into the bulk as well, much beyond the correlation length of the system, which is a few roll widths. Roll mergers spread across the bulk of the system can ensure that the even rolls far from the boundary remain connected to it. This occurs easily in stationary patterns of straight rolls where every roll is connected to the boundary.

6.4   Outlook

The various characterizations developed from the time series of the Betti numbers are seen to show distinctive changes with variation in the parameter of the system, ϵ in our case.
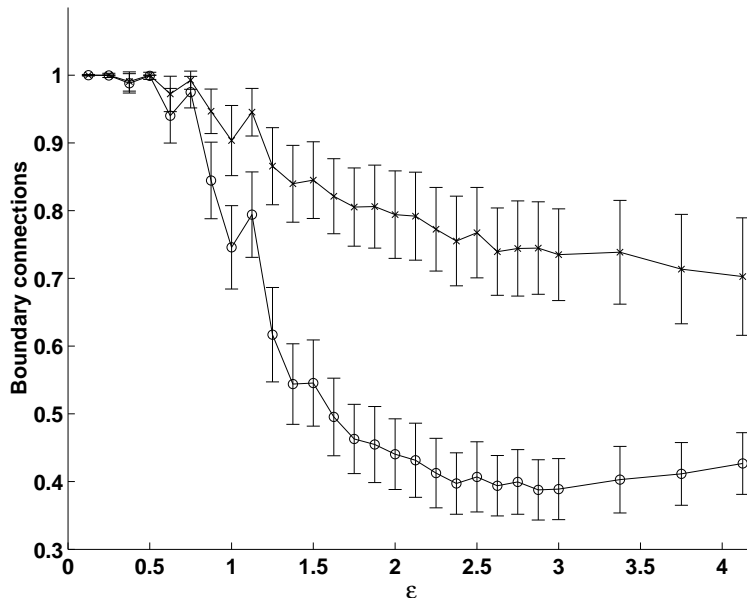
Figure 47: The number of components for hotflows (crosses) and cold flows (circles) connected to the boundary, normalized by the total number of such components. The errorbars indicate the fluctuation in this number as seen over a long time series. At low values of ϵ, the pattern consists of primarily straight rolls, thus every component is connected to the boundary - such a pattern is also symmetric to upflows and downflows. At higher ϵ, the complexity of the pattern segregates sections away from the boundary.

The transition to time dependence and the onset of SDC occurs at about $\epsilon = 0.5$, and this is reflected in the various measures described. A continuous phase transition has been previously suggested by Cakmur et. al. [9], at roughly the same value of ϵ although at a different aspect ratio.

This variation of the Betti numbers with system parameters may also be utilized to estimate the parameters the system operates at. New parameters too may be developed, such as the degree of asymmetry between hot and cold rolls, from the Betti number time series. Often, there is a delay between the response of a system to a variation in an externally controlled parameter. A continuous linear change in ϵ for instance may not correspond to a linear variation in the Betti numbers. The variation of the Betti numbers may also depend on the rate of the variation in ϵ. The dynamics at a transient region may be compared to steady state vaues for comparison. The Betti numbers form a easily computable and small data set from which effective system parameters may be characterized, even from the transient dynamics.

The Betti numbers offer a efficient reduction of the geometric structure of a spatially extended system that help infer the system parameters. The Betti numbers might be utilized in devising control schemes for the system, to track and maneuver the system to a desired target configuration. This would be particularly useful in cases where the system parameters are not easily infered otherwise.

The occurrences of bifurcations as suggested by the number of states and entropy in the system would benefit through comparison with numerical simulations of the Navier-Stokes equations for RBC. The bifurcation points, even for time independent Navier-Stokes equations, with a variation in ϵ corresponding to our cell geometry would be one of the most direct ways of correlating the non-monotonic behavior of entropy to bifurcations.

In the current set of experiments only the driving through the system has been varied. The scaling of the Betti numbers with a variation in aspect ratio would be insightful in studying the dynamics of the system. At low aspect ratios ($\Gamma < 15$), the state of rolls are strongly confined by the geometry of the boundary. Experiments have also shown that periodic behavior through recurrent defect formation may occur. This would be reflected as a periodic variation in the β_0 as rolls merge and new rolls form [15]. For a symmetric pattern such as straight parallel rolls an increase in aspect ratio along the wave vector would increase β_0, however transverse to the wave vector, the increased scale of the pattern would not be reflected in the Betti numbers. In disordered patterns such as SDC, at larger aspect ratios, it would be natural to expect that all the Betti numbers would increase with system size. The details of this increase however are unclear. At sufficient driving, the increase in β_0 due to an increase in aspect ratio may be mitigated through a dense distribution of defects that connect components. The extensivity of the Betti numbers with system size would be expected to occur beyond some particular aspect ratio which is a function of ϵ. The density of Betti numbers(β/Γ) may be conserved at very large aspect ratios.

A variation in the geometry of the boundary at moderate and low aspect ratios would be interesting as well. The measurement of the Betti numbers in a elliptical cell may not be easily extrapolated from those of circular cell geometries at two aspect ratios corresponding to the major and minor radii of the elliptical boundary. The spatial distribution and

spectrum of the modes leading to the dominant dynamics at low aspect ratios would be strongly influenced by the boundary conditions.

The onset of convection for a larger separation between the plates occurs at lower temperature gradients. The variation in fluid properties as a result of temperature dependence would be reduced in deeper cells. The impact of non-Boussinesq fluid properties may be studied through a variation in the depth of the cell layer.

The Betti numbers as a characterizations reduce large geometric structures to a set of scalars. This reduction contains specific information about the original structure. A measurement at a resolution that captures the essential geometric features of interest are sufficient to extract exact Betti numbers. In time dependent geometries such as SDC, one time scale that may be relevant would the time taken by the system to span states across the entire attractor. This would also determine the convergence rates of measured observable defined over the attractor. Observations over longer periods of time may therefore improve the precision of measures such as mean values, entropy etc. as described in this section.

In most measures discussed thus far, the spatial information about the complex state has been emphasized. The temporal transitions between these states have not been quantified. One novel method of incorporating this into the geometric structure would be to build three dimensional cubical complexes, with two spatial dimensions and one temporal dimension(similar to the construction of the cubical complex in [24]). This binary representation would result from 'stacking' the consecutive 2-D spatial images discussed so far to form a 3-D cube. Such a structure would be described by a three Betti numbers, translating into independent components, tunnels in the structure and cavities or bubbles. The cavities in the structure would correspond to rolls that form and disappear within the bulk of the system without ever coming in contact with the boundary of the system.

CHAPTER VII

CONCLUSIONS

In this thesis we have investigated the dynamics of SDC at two different length and time scales. The characteristic wavelength the rolls is governed by the depth of the fluid layer and the time scale determined as the thermal diffusion time across the layer, τ_ν. At this scale we characterize dynamics of rolls through instability mechanisms leading to defect nucleation driving the chaotic evolution. The long time $(10^3 \tau_\nu)$ evolution at scales corresponding to the system size, homological characterizations indicates the pattern dynamics to be stochastic in nature.

Relating the dynamics at a global scale to that at the scale of a few rolls is important to understanding the complex behavior. One clue to this may lie in the non-monotonic growth of entropy with ϵ (Fig. 41 and 39). This might be an indication of wavenumber frustrations operating in the pattern. The attractors converged to at different values of epsilon may be commensurate to the confining geometry to different degrees. Attractors that are more commensurate would have a lower entropy even if the system is driven harder (larger ϵ) and exhibits a more intricate pattern indicated by the Betti numbers. The different degrees of commensuracy may relate to the different driving accommodating the pattern better as a result of changes in the curvature or number of rolls.

The above discussion is important not only because might it connect the local measures to global ones, but also because the entropy might be an indicator of bifurcations occurring within the system within a turbulent regime. We are unaware of any other techniques to measure these bifurcations in a similar system.

We expect similar behaviour to occur as the aspect ratio of the convection cell is varied. The commensuracy of the pattern may be changed through relative size of the cell as compared to the local roll width. This would be marked by a shift in the peaks of the entropy plots as a function of ϵ as well as in the plateaus in the number of states. The

shape of the cell may be insightful as well, with a deviation from a circular(to elipsoidal, or square to rectangular for instance) geometry resulting in further bifurcations due to the break in symmetry. Our current investigations focus on further understanding these mechanisms through variations in ϵ and cell geometry.

While the local roll instabilities may be well described by deterministic models, a succession of such instabilities across the entire domain of the system leads to stochastic evolution globally. Stochastic dynamics are intrinsically ergodic. The two characterizations developed give credence to suggestions relating microscopic chaotic dynamics being the seat of ergodic behaviour in the dynamics of SDC. The ergodic evolution of a system through phase space is of fundamental importance to the foundations of statistical mechanics.

Our initial motivation was to develop symbolic dynamics from the time series of Betti numbers tracking the evolution of the state. Our investigations indicate that while the Betti numbers are good indicators of variation in the pattern, their stochastic variation shows little sign of chaotic dynamics in SDC.

While the homological characterization provides a useful measure of dynamics at the global scale, a holistic description of the system requires the description at all length scales to be reconciled. In SDC, the roll wavelengths form a natural length scale determining the evolution of the pattern. The interaction between neighboring rolls are seen to lead to the globally complex behavior. In Chapter 4 we explored the dynamics at this scale.

Independent of the particulars of implementation, the experimental and analysis concepts developed in Chapter 4 are readily applicable to a variety of pattern forming systems. While we have focused on developing the tools about stationary states, the method may be extended to periodic orbits or segments of complex trajectories with only a few modifications. The experimental procedures and numerical analysis to extract the linear manifold about trajectories of experimental realizations of spatially extended systems is well developed.

This aspect of the thesis has attempted to bridge some of the gaps between experimental and numerical investigations of pattern forming systems. This is done by extending the information conventionally provided in experiments from measurements of the trajectory,

to its neighborhood as well. This relates directly to the information provided by the jacobian of a system of equations used in theoretical approaches.

In regard to implementing active control of SDC, there need to be many advances in experimental capabilities. Feedback control requires data acquisition, analysis and actuation of the flow at rates not feasible with the current setup. It is also not clear as to how large the linear neighborhood is in the vicinity of local instabilities associated with defect nucleation. The size on this neighborhood may depend on the local curvature, mean flows and experimental biases within the system. A more thorough investigation into the realm of applicability of the linear manifold would be needed - it would not be unusual to anticipate many of the local instabilities to be modeled by imperfect bifurcations.

We have imposed ensembles of complex geometries as initial conditions at low Rayleigh numbers and monitored their subsequent evolution. This has helped us in guiding improvements in our experiments regarding control schemes. Technological advances should resolve many of the issues currently stopping the implementation of control.

REFERENCES

[1] AUERBACH, D., CVITANOVIĆ, P., ECKMANN, J.-P., GUNARATNE, G., and PROCACCIA, I., "Exploring Chaotic Motion Through Periodic Orbits," *Phys. Rev. Let.*, vol. 58, pp. 2387–2389, 1987.

[2] AUERBACH, D., GREBOGI, C., OTT, E., and YORKE, J. A., "Controlling Chaos in High Dimensional Systems," *Phys. Rev. Lett.*, vol. 69, p. 3479, 1992.

[3] BATCHELOR, G. K., *An Introduction to Fluid Dynamics.* Cambridge University Press, 2000.

[4] BOCCALETTI, S., GREBOGI, C., LAI, Y. C., MANCINI, H., and MAZA, D., "The Control of Chaos: Theory and Applications," *Phys. Reports*, vol. 329, p. 103, 2000.

[5] BODENSCHATZ, E., DEBRUYN, J. R., AHLERS, G., and CANNELL, D. S., "Transitions Between Patterns in Thermal Convection," *Phys. Rev. Lett.*, vol. 67, p. 3078, 1991.

[6] BUSSE, F. H., "The Stability of Finite Amplitude Cellular Convection and its Relation to an Extremum Principle," *J. Fluid Mech.*, vol. 30, no. 4, pp. 625–649, 1967.

[7] BUSSE, F. H., "Non-linear Properties of Thermal Convection," *Rep. Progr. Phys.*, vol. 41, no. 12, pp. 1929–1967, 1978.

[8] BUSSE, F. H. and WHITEHEAD, J. A., "Instabilities of Convection Rolls in a High Prandtl Number Fluid," *J. Fluid Mech.*, vol. 47, p. 301, 1971.

[9] CAKMUR, R. V., EGOLF, D. A., PLAPP, B. B., and BODENSCHATZ, E., "Bistability and Competition of Spatiotemporal Chaotic and Fixed Point Attractors in Rayleigh-bénard convection," *Phys. Rev. Lett.*, vol. 79, no. 10, pp. 1853–1856, 1997.

[10] CHANDRASEKHAR, S., *Hydrodynamic and Hydromagnetic Stability.* The International Series of Monographs on Physics, Clarendon Press, Oxford, 1961.

[11] CHEN, M. M. and WHITEHEAD, J. A., "Evolution of Two-dimensional Periodic Rayleigh Convection Cells of Arbitrary Wave-numbers," *J. Fluid Mech.*, vol. 31, p. 1, 1968.

[12] CHIAM, K. H., *Spatiotemporal Chaos in Rayleigh-Bénard Convection.* PhD. Thesis, California Institute of Technology, 2005.

[13] CHIAM, K.-H., CROSS, M. C., and GREENSIDE, H. S., "Mean Flow and Spiral Defect Chaos in Rayleigh-Bénard Convection," *Phys. Rev. E*, vol. 67, 056206, 2003.

[14] CHRISTIANSEN, F., CVITANOVIC, P., and PUTKARADZE, V., "Hopf's Last Hope: Spatiotemporal Chaos in Terms of Unstable Recurrent Patterns," *Nonlinearity*, vol. 10, pp. 55–70, 1997.

[15] CROQUETTE, V., "Convective Pattern Dynamics at Low Prandtl Number: Part i.," *Contemporary Physics*, vol. 30, no. 2, pp. 113–133, 1989.

[16] CROSS, M. C. and HOHENBERG, P. C., "Pattern Formation Outside of Equilibrium," *Rev. Modern Phys.*, vol. 65, no. 3, pp. 851–1112, 1993.

[17] CROSS, M. C. and TU, Y., "Defect Dynamics for Spiral Chaos in Rayleigh-Bénard Convection," *Phys. Rev. Let.*, vol. 75, no. 5, pp. 834–837, 1995.

[18] CVITANOVIĆ, P., ARTUSO, R., MAINIERI, R., TANNER, G., and VATTAY, G., *Chaos: Classical and Quantum.* Niels Bohr Institute, Copenhagen, 2005.

[19] DE BRUYN, J., BODENSCHATZ, E., MORRIS, S., TRAINOFF, S., HU, Y., CANNELL, D., and AHLERS, G., "Apparatus for the Study of Rayleigh-Bénard Convection in Gases," *Rev. of Sci. Instrum.*, vol. 67, pp. 2043–2067, 1996.

[20] ECKE, R. E. and HU, Y., "Spiral Defect Chaos in Rayleigh-Bénard Convection: Defect Population Statistics," *Phys. A*, vol. 239, no. 1-3, pp. 174–188, 1997.

[21] ECKE, R. E., HU, Y., MAINIERI, R., and AHLERS, G., "Excitation of Spirals and Chiral Symmetry Breaking in Rayleigh-Bénard Convection," *Science*, vol. 269, no. 5231, pp. 1704–1707, 1995.

[22] EGOLF, D. A., MELNIKOV, I. V., and BODENSCHATZ, E., "Importance of Local Pattern Properties in Spiral Defect Chaos," *Phys. Rev. Lett.*, vol. 80, no. 15, pp. 3228–3231, 1998.

[23] EGOLF, D. A., MELNIKOV, I. V., PESCH, W., and ECKE, R. E., "Mechanisms of Extensive Spatiotemporal Chaos in Rayleigh-Bénard Convection," *Nature*, vol. 404, no. 6779, pp. 733–736, 2000.

[24] GAMEIRO, M., MISCHAIKOW, K., and KALIES, W., "Topological Characterization of Spatial-temporal Chaos," *Phys. Rev. E*, vol. 70, no. 3, p. 035203, 035203, 2004.

[25] GAMEIRO, M., MISCHAIKOW, K., and WANNER, T., "Evolution of Pattern Complexity in the Cahn-Hilliard Theory of Phase Separation,," *Acta Materialia*, 2004.

[26] GARNIER, N., GRIGORIEV, R. O., and SCHATZ, M. F., "Optical Manipulation of Microscale Fluid Flow," *Phys. Rev. Let.*, vol. 91, 054501, 2003.

[27] GOLDENBERG, C. and GOLDHIRSCH, I., "Force Chains, Microelasticity, and Macroelasticity," *Phys. Rev. Lett.*, vol. 89, no. 8, 084302, 2002.

[28] GOLUBITSKY, M., SWIFT, J., and KNOBLOCH, E., "Symmetries and Pattern Selection in Rayleigh-Bénard Convection," *Physica D*, vol. 10, 1984.

[29] GOLUBITSKY, M., SWIFT, J. W., and KNOBLOCH, E., "Symmetries and Pattern Selection in Rayleigh-Bénard Convection," *Physica D*, vol. 10D, pp. 249–276, 1984.

[30] GRIGORIEV, R. O., "Control of Spatially Extended Chaotic Systems," in *Handbook of Chaos Control* (SCHUSTER, H. G., ed.), New Jersey: Wiley-VCH, 1998.

[31] GRIGORIEV, R. O. and CROSS, M. C., "Controlling Physical Systems with Symmetries," *Phys. Rev. E*, vol. 57, p. 1550, 1998.

[32] GRIGORIEV, R. O., CROSS, M. C., and SCHUSTER, H. G., "Pinning Control of Spatiotemporal Chaos," *Phys. Rev. Lett.*, vol. 79, p. 2795, 1997.

[33] GRIGORIEV, R. O., LALL, S. G., and DULLERUD, G. E., "Localized Optimal Control of Spatiotemporal Chaos," *in Proc. NOLTA*, 1997.

[34] HOLMES, P. J., LUMLEY, J. L., and BERKOOZ, G., *Turbulence, Coherent Structures, Dynamical Systems and Symmetry.* Cambridge University Press, 1996.

[35] HOWLE, L. E., "Active Ccontrol of Rayleigh-Bénard Convection," *Phys. Fluids*, vol. 9, p. 1861, 1997.

[36] HU, Y., ECKE, R., and AHLERS, G., "Convection for Prandtl Numbers Near 1: Dynamics of Textured Patterns," *Phys. Rev. E*, vol. 51, no. 4, pp. 3263–3279, 1995.

[37] KACZYNSKI, T., MISCHAIKOW, K., and MROZEK, M., *Computational Homology*, vol. 157 of *Applied Mathematical Sciences.* New York: Springer-Verlag, 2004.

[38] KALIES, W. and PILARCZYK, P., "Computational Homology Program." http://www.math.gatech.edu/~chom/, 2003.

[39] LANDAU, L. D. and LIFSHITZ, E., *Fluid Mechanics.* A course on theoretical Physics, Pergamon Press, London, England, 1959.

[40] MANNEVILLE, P., *Dissipative Structures and Weak Turbulence.* Perspectives in Physics, Boston, MA: Academic Press Inc., 1990.

[41] MORRIS, K., *Introduction to Feedback Control.* San Diego: Harcourt Academic Press, 2001.

[42] MORRIS, S. W., BODENSCHATZ, E., CANNELL, D. S., and AHLERS, G., "Spiral Defect Chaos in Large Aspect Ratio Rayleigh-Bénard Convection," *Phys. Rev. Lett.*, vol. 71, no. 13, pp. 2026–2029, 1993.

[43] MORRIS, S. W., BODENSCHATZ, E., CANNELL, D. S., and AHLERS, G., "The Spatiotemporal Structure of Spiral-Defect Chaos," *Phys. D*, vol. 97, no. 1-3, pp. 164–179, 1996.

[44] NEWELL, A. C., PASSOT, T., and SOULI, M., "Convection at Finite Rayleigh Numbers in Large-Aspect-Ratio Containers.," *Phys. Rev. Let.*, vol. 64, no. 20, pp. 2378–2381, 1990.

[45] NEWELL, A. C., PASSOT, T., and SOULI, M., "The Phase Diffusion and Mean Drift Equations for Convection at Finite Rayleigh Numbers in Large Containers.," *J. Fluid Mech.*, vol. 220, pp. 187–252, 1990.

[46] NIETHAMMER, M., KALIES, W. D., MISCHAIKOW, K., and TANNENBAUM, A., "On the Detection of Simple Points in Higher Dimensions Using Cubical Homology," *Elsevier Science*, Submitted March 2005.

[47] OR, A. C., CORTELEZZI, L., and SPEYER, J. L., "Robust Feedback Control of Rayleigh-Bénard Convection," *J. Fluid Mech.*, vol. 437, p. 175, 2001.

[48] OTT, E., GREBOGI, C., and YORKE, J. A., "Controlling Chaos," *Phys. Rev. Lett.*, vol. 64, p. 1196, 1990.

[49] PLAPP, B. B., *Spiral Pattern Formation in Rayleigh-Bénard Convection.* PhD. Thesis, Cornell University, 1997.

[50] QIN, F., WOLF, E. E., and CHANG, H. C., "Controlling Spatiotemporal Patterns on a Catalytic Wafer," *Phys. Rev. Lett.*, vol. 72, no. 10, p. 1459, 1994.

[51] RAYLEIGH, "On Convective Currents in a Horizontal Layer of Fluid When the Higher Temperature is on the Under Side," *Phil.Mag*, vol. 32, pp. 529–546, 1916.

[52] ROGERS, J. L., *Modulated Pattern Formation: Stabilization, Complex-Order, and Symmetry.* PhD. Thesis, Georgia Institute of Technology, 2001.

[53] RUELLE, D. and TAKENS, F., "On the Nature of Turbulence," *Commun. Math. Phys.*, vol. 20, pp. 167–192, 1971.

[54] SEMWOGERERE, D. and SCHATZ, M. F., "Evolution of Hexagonal Patterns from Controlled Initial Conditions in a Bénard-Marangoni Convection Experiment," *Phys. Rev. Let.*, vol. 88, p. 054501, 2002.

[55] SETTLES, G., *Schlieren and Shadowgraph Techniques.* Springer, 2001.

[56] SIROVICH, L., "Chaotic Dynamics of Coherent Structures," *Physica D*, vol. 37, pp. 126–145, 1989.

[57] SORNBORGER, A., SAILSTAD, C., KAPLAN, E., and SIROVICH, L., "Spatiotemporal Analysis of Optical Imaging Data," *NeuroImage*, vol. 18, no. 3, pp. 610–621, 2003.

[58] STROGATZ, S. H., *Nonlinear Dynamics and Chaos.* Addisson-Wesley, Reading, MA, 1994.

[59] TANG, J. and BAU, H. H., "Stabilization of the No-Motion State in Rayleigh-Bénard Convection Through Use of Feedback Control," *Phys. Rev. Lett.*, vol. 70, p. 1795, 1993.

[60] VANDOREN, V., "PID – The Basic Technique for Feedback Control," *Control Engineering*, vol. 44, 1997.

[61] WITKOWSKI, F. X., KAVANAGH, K. M., PENKOSKE, P. A., PLONSEY, R., SPANO, M. L., DITTO, W. L., and KAPLAN, D. T., "Evidence for Determinism in Ventricular Fibrillation," *Phys. Rev. Lett.*, vol. 75, pp. 1230–1233, 2004.

[62] ZOLDI, S. M., LIU, J., BAJAJ, K. M. S., GREENSIDE, H. S., and AHLERS, G., "Extensive Scaling and Nonuniformity of the Karhunen-Loeve Decomposition for the Spiral-Defect Chaos State," *Phys. Rev. E*, vol. 58, pp. **R**6903–**R**6906, 1998.

[63] ZORZANO, M.-P., HOCHBERG, D., CUEVAS, M.-T., and CÓMEZ-GÓMEZ, J.-M., "Reaction-Diffusion Model for Pattern Formation in E. Coli Swarming Colonies with Slime," *Phys. Rev. E*, vol. 71, 2005.